Magnetic Resonance Imaging of Hydrate Phase Transitions in Sediments

Master Thesis in Reservoir Physics

by

Veronica Flæsland Veland

Department of Physics and Technology

UNIVERSITY OF BERGEN

November 2017

SUMMARY

Natural gas hydrates, simplified described as gas compressed in ice, are a substance existing in large quantities around the world. Their existence requires elevated pressures and low temperature. They are therefore found in the subsurface in and below permafrost and in oceanic environments below a water column of 400-500 meters. The significant amount of gas stored in natural gas hydrates constitutes a potential as a significant contributor in ensuring future energy sustainability. However, extended research on fundamentals and characteristics of hydrates in nature, as well as production schemes, are required to be able to efficient and safely exploit this energy resource. Core-scale experiments give fast and valuable information, which is essential before larger field tests can be planned.

This thesis is part of a research collaboration between Statoil and the University of Bergen in the application of magnetic resonance imaging (MRI) in laboratory petro-physics and core analysis. The new experimental design in this work includes the high field strength magnet of the 4.7 Tesla Biospec MR-scanner, by contrast to the domination of low field strengths in this kind of research. The main objective of this thesis is to show that the high field strength MRI can be applied to visualize gas hydrate phase transitions in a porous media of a sandstone core, before more advanced studies can take place.

First, basic introductory experiments were conducted to illustrate the correlation of water saturation of a core and the signal intensity of the MRI measurement. Two Bentheim sandstones were measured, one with increasing water saturation for each measurement, and the other with decreasing water saturation for each measurement. Two types of MR measurements were conducted on the cores at each water saturation stage: (1) RARE, used to image and for further pixel analysis, (2) MSME, to investigate T2 relaxation. Results from the introductory experiments illustrated the strong relationship between MR signal intensity and water saturation. This fact was fundamental in analyzing the results of the high-pressure study.

Second, MRI measurements of gas hydrate formation and dissociation within sediments were acquired. The Bentheimer sandstone was initially saturated with 65% with 0.1wt% sodium chloride (NaCl). The gas consisted of 22% propane in 78% methane. This gas mixture was chosen to provide hydrate stable conditions at room temperature (21°C). Stimulation of gas hydrate formation and dissociation were therefore possible by regulating the gas pressure when the core was mounted in a high-pressure cell. Two types of MR measurements were conducted through the hydrate study: (1) RARE, used to image and analyze the spatial development in the core, and (2) CPMG to investigate how T2 relaxation changed with hydrate formation/dissociation.

Phase transitions of gas hydrate in the Bentheimer sandstone were successfully imaged and visualized by both RARE and CPMG measurements. Three different methods are suggested for estimation of hydrate saturation. The methods are based on results from (1) pixel analysis by RARE, (2) T2 distribution maps by CPMG, and (3) the initial signal intensity of the decay curve by CPMG. Estimations from the three different methods were in good agreement, and found hydrate saturation to be in the region of 42±3 %. Because of the good agreement, saturation estimations based on measurements attained from a high field strength magnet were found to be promising.

ACKNOWLEDGMENTS

First of all, I would like to express my gratitude to my supervisors Associate Professor Geir Ersland at the Department of Physics and Technology at the University of Bergen, and Professor Per Fotland at Statoil, for the opportunity to work on such an interesting topic. Thank you for the support, guidance and valuable discussions.

I would like to thank my lab-partner PhD candidate Stian Almanningen, for sharing his experience and knowledge, and for being great company during long hours in the laboratory. I would also like to thank Gry L. Aastveit at Statoil and Dr. Marianne Steinsbø at the University of Bergen for giving good experimental advice, and Associate Professor John Georg Seland for contributing with his MRI knowledge. It has been a great experience to enter the complex world of MRI/NMR with this cross-institute research group. In addition, I would like to thank Professor Arne Graue and Professor Martin Fernø for their contributions to the Reservoir Physics group.

Thanks to my fellow students. You have made the years memorable with laughter and discussions both on and off topic. I am especially grateful to get to know my close friends Eirik L. Alver and Kristian V. Greenway. You are a piece of art.

Finally, a special thanks to my family and friends for support and motivation.

Bergen, November 2017

Veronica Flæsland Veland

TABLE OF CONTENTS

PART I. INTRODUCTION AND THEORY

INTRODUCTION

Natural gas hydrates are crystalline solids composed of water and gas molecules. They are formed in high-pressure and low-temperature environments. Gas hydrates are classified as clathrate compounds. *Clathratus* is Latin and is translated to "*to encage*". The hydrogen-bonded water molecules create cages that encapsulate gas molecules, also referred to as guest molecules or hydrate formers. Typical guests include methane, ethane, propane and carbon dioxide [6]. Methane hydrate is sometimes referred to as *the burning ice* or *fire ice* because the warming hydrates release enough methane to sustain a flame. The primary focus on gas hydrates has been on assuring flow in wells and production pipelines in the petroleum industry [12, 13]. Gas hydrate formation can plug the pipeline, which can cause damage on equipment, and become a safety risk. Figure 1 displays an example.

Figure 1: Illustration of a hydrate plug (blue) in a pipeline. In a scenario where the pressure is reduced in one end, the plug can melt and turn into a projectile (darker blue). This can cause damage on equipment, and in worst case scenarios result in fatal accidents.

The last decades, gas hydrates have shown to have another interesting aspect. Natural gas hydrate accumulations are found within sediments in the earth both offshore and onshore, and distributed all over the world [14]. A map showing known and inferred occurrences of sedimentary gas hydrates are displayed in Figure 2. Gas hydrates are considered a potential unconventional gas resource, because of their significant gas content. Several studies have shown that the amount of gas stored in methane hydrates in the world may exceed the volume of known fossil organic carbon sources [e.g. [15, 16]]. Each volume of hydrate can contain as much as 164 volumes of gas at standard pressure and

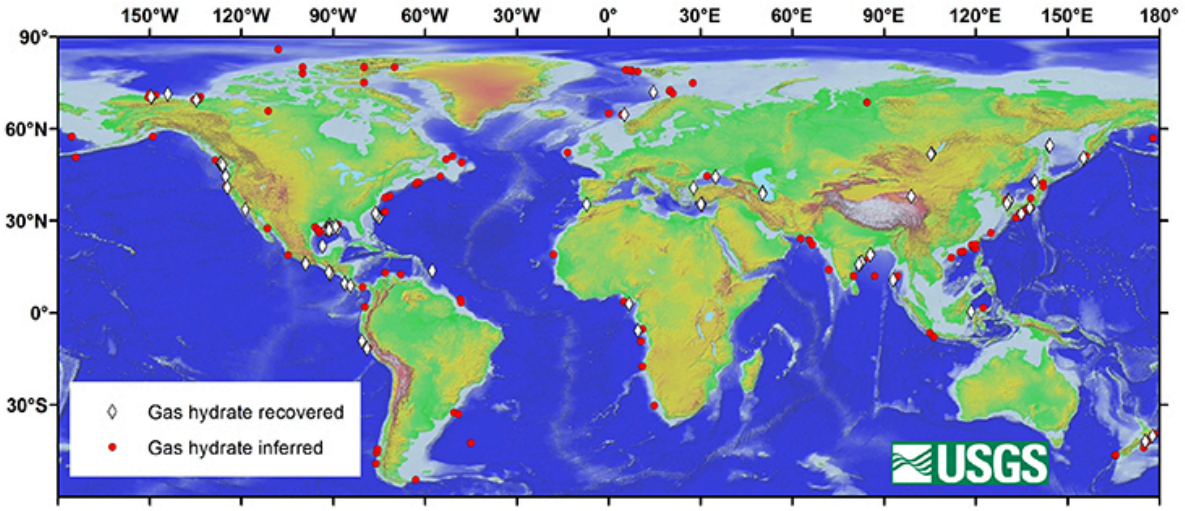

Figure 2: Map of hydrate distribution, recovered in white and inferred in red. The figure is based on information per December 2013. Inferences are most often based on discovery of a seismic interface known as the BSR (bottom simulating reflector) in marine sediments, but can also reflect the analysis of borehole logging data. US Geological Survey [7].

temperature [6]. This is the main reason for the growing interest of natural gas hydrates, and especially in countries like Japan, South-Korea, China and India, seeking to be self-sustained in energy.

It has to be emphasized that not all hydrate reserves are targets for production, as they need to be of a certain concentration to be interesting in this regard. Another problem is accessing the gas hydrates. Technology development adapted to the specific properties and conditions associated with gas hydrates are required to be able to efficient and safely exploit this energy resource [3]. For example, most of the production schemes suggested offshore include breaking the gas hydrates into gas and water. Dissociating the gas hydrates can result in destabilizing the seabed, which can lead to submarine landslides.

Subsequently, there is a need for extended research on fundamentals and characteristics of gas hydrates, as well as the production schemes. This thesis contributes with experiments on core level. Magnetic resonance imaging (MRI) is widely employed in the petroleum industry, both for down-hole logging and in laboratory core analysis. The purpose of this study is to investigate if a high field strength magnet (4.7 Tesla) can be applied to visualize gas hydrate phase transitions in a porous media of a sandstone core. The theory presented are therefore divided in two main sections, (1) fundamentals of natural gas hydrates, and (2) fundamentals of magnetic resonance imaging. In addition, a literature survey of some relevant MRI research is presented.

1 FUNDAMENTALS NATURAL GAS HYDRATES

1.1 GAS HYDRATE STRUCTURES AND GUESTS MOLECULES

Gas hydrates are formed of water and gas molecules. The water molecules create crystal units, where the guest can be encaged. Relative to the molecular structure of ice, hydrate cavities are expanded. This is possible because of the repulsive presence of guest molecules, which prevents the cages to collapse [6, 11, 17], See example of in Figure 1-1.

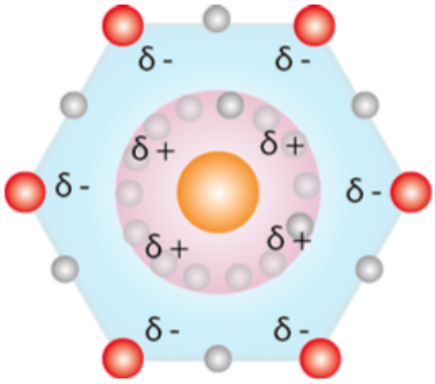

Figure 1-1: 2D illustration of H_2S in a hydrate cavity. Red indicates oxygens, and gray hydrogens that make up the cage. H_2O dipole moments leads to an average δ- field inwards in the cavity. The opposing electrostatic fields between the rotating molecule (δ+) and the cage walls (δ-), makes H_2S a good hydrate former [2].

The size (and geometry) of these crystal units are depending on the size and shape of the gas molecules entering them. There are three common types of structures. Depending on their geometry, they are divided in [6, 18]:

- cubic structure I (sI)
- cubic structure II (sII)
- hexagonal structure H (sH)

Illustration of the structures are found in Figure 1-2. Structure properties, information about natural environment and guest molecules, are listed in Table 1-1.

There is also a distinction between what is called *simple hydrates* and *mixed hydrates*. Simple hydrates have only one guest specie, in contrast to mixed hydrates where cages of the same kind are occupied by two types of molecules, with the restriction of at most one molecule per cage [18].

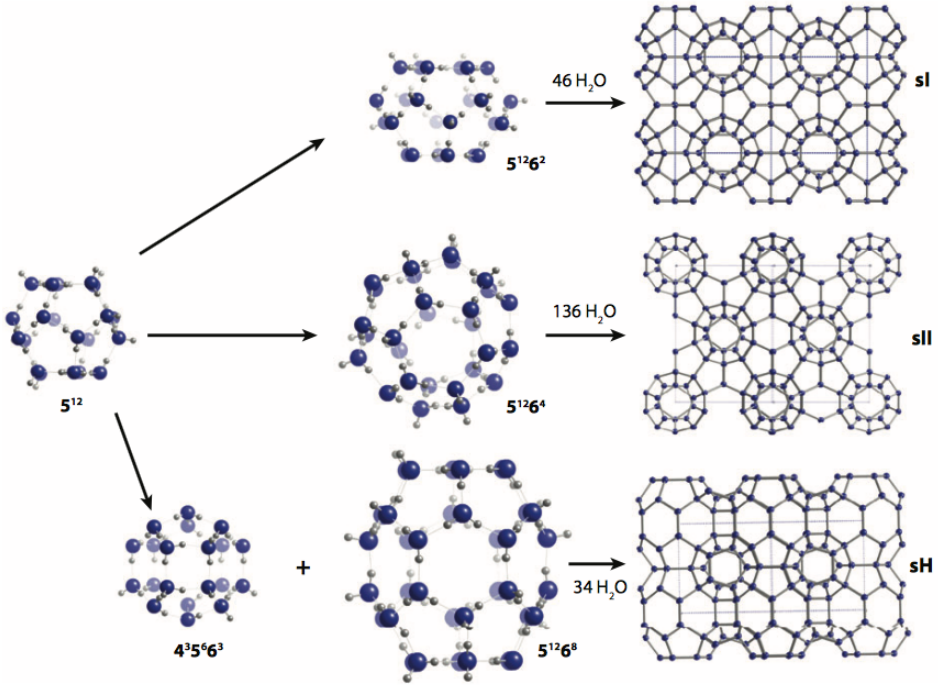

Figure 1-2: Three different hydrate structures, built of 5 different cages. The different polyhedral cages are described by the different type of faces it consists of. For example, the smallest cage, which is a building block in all of the crystal structures, consists of 12 faces of pentagonally bonded water molecules, and are written 5^{12}, (called pentagonal dodecahedra) [1, 2].

Table 1.1: Hydrate structure properties [5]

Hydrate	sI		sII		H		
Environment	Predominates in the Earth´s natural environment		In mostly man-made environments		In both environments, but only with mixtures of both small and large molecules.		
Cavity	Small	Large	Small	Large	Small	Medium	Large
Nomenclature	5^{12}	$5^{12}6^2$	5^{12}	$5^{12}6^4$	5^{12}	$4^35^66^3$	$5^{12}6^8$
Number of cavities per unit cell	2	6	16	8	3	2	1
H_2O per unit cell	46		136		34		
Example of guests	Methane, ethane, propane, carbon dioxide (CO_2), hydrogen sulfide (H_2S)		(Small) Nitrogen, argon, oxygen, together with (larger) propane, iso-butane		(Small) methane, hydrogen sulfide, nitrogen, together with (larger) iso-pentane, neohexane		

1.2 STABILITY CONDITIONS

The formation of hydrate depends on [5, 19]:

- Favorable thermodynamic conditions (incl. heat transfer)
- Sufficient amounts of water and gas (incl. mass transport)

Figure 1-3 illustrate the equilibrium phase curve for methane hydrate. As the figure indicates, high pressure and low temperatures are required for hydrate stability, illustrated as the blue region in the left figure. The stronger guest-water attraction, the better the stabilization, and the higher temperature allowance for hydrate stability [5].

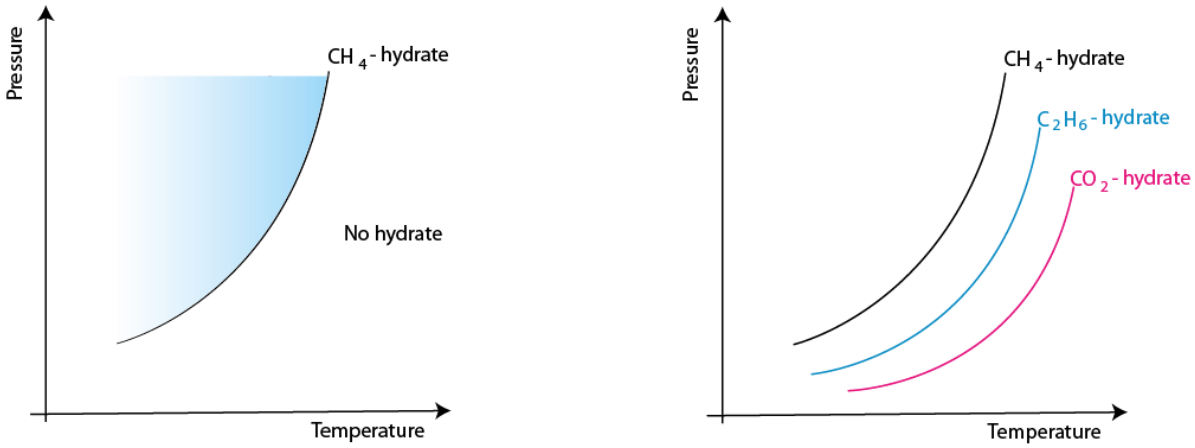

Figure 1-3: Left, illustration of an equilibrium phase curve for methane (CH_4) hydrate. Hydrates are formed at condition over the curve. Right, illustration of relative equilibrium curves for methane, ethane (C_2H_6) and carbon dioxide (CO_2). Notice that carbon dioxide is more stable than methane hydrate (at temperatures below 10°C).

Phase diagrams like the above are important in the industry as a guidance to keep well pressures out of hydrate formation zones. The equilibrium phase curve, for the gas mixture used in this thesis are found in Figure 1-4. The room temperature is held approximately 21°C (requirements of the magnet), a condition that will exclude the possibility of formation of ice. Hydrate formation and dissociation are stimulated by increasing and decreasing the pressure.

Values for the curve is estimated by PVTSIM nova, which is a simulation program developed for reservoir engineers, flow assurance specialists, PVT lab engineers and process engineers. It gives reliable fluid characterization, using robust and efficient regression algorithms, matching fluid properties and experimental data. Here, the Peng Robinson equation of state used [20].

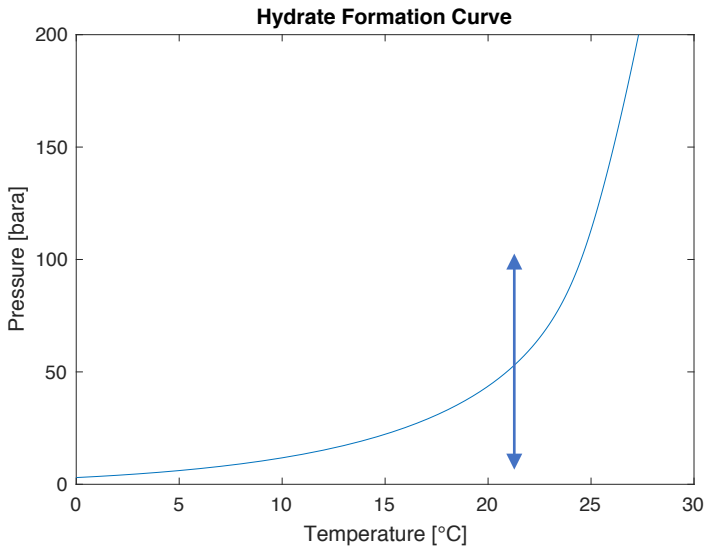

Figure 1-4: The phase diagram, or equilibrium phase curve, for a gas mixture of 22% propane and 78% methane, and water with 0.1wt% sodium chloride (NaCl). Gas hydrate is stable inside the curve. The arrow illustrates the pressure region used for formation (up) and dissociation (down) in the experiment. The figure is plotted in MATLAB, using values from PVTSIM.

1.3 HYDRATE PHASE TRANSITIONS AND PRODUCTION SCENARIOS

This section will look at some basic concepts within hydrate phase transitions, which will be divided in hydrate formation and hydrate dissociation. The end section will in addition look at possible production scenarios. A good place to start for understanding the phase transition concepts, is through Figure 1-5.

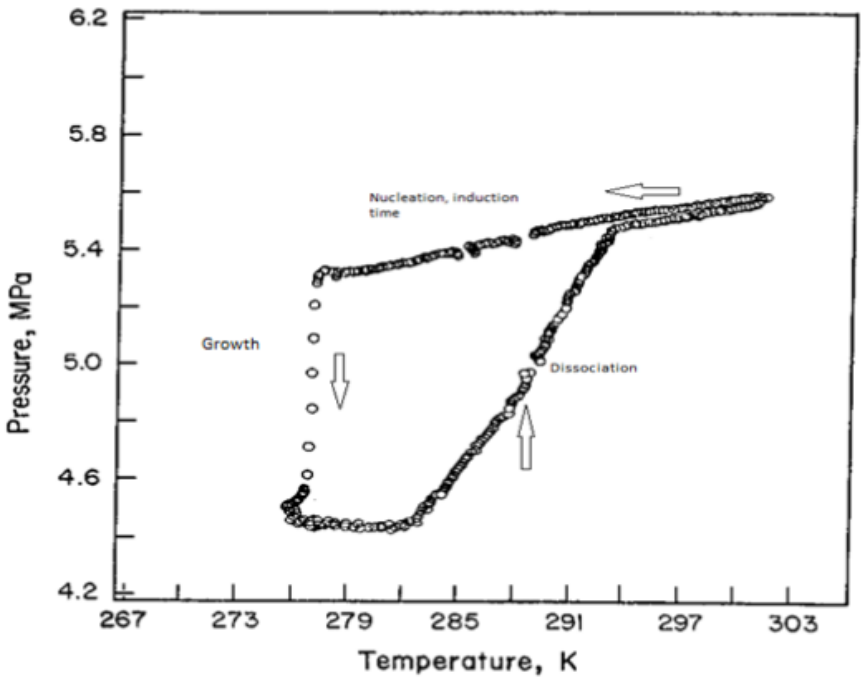

Figure 1-5: Temperature and pressure trace for formation of simple hydrates. From top right, nucleation and induction as pressure and temperature is decreased. The growth process consumes gas and pressure is reduced. Dissociation happens when pressure and/or temperature is changed outside the hydrate stability zone [6] [10].

1.3.1 Hydrate formation

Hydrate formation can commence once enough water and guest molecules are within the hydrate stability zone. The formation process is a crystallization process, characterized by induction time and a nucleation phase followed by hydrate crystal growth. Nucleation refers to the process that results in the onset of hydrates, whereas the time required for the onset of hydrate formation is known as the induction time [21]. There are therefore three important concepts when talking about hydrate formation in laboratory systems: nucleation, induction time and growth, and are described as follows:

Nucleation

Hydrate nucleation is a stochastic process, during which small hydrate crystals grow and disperse, before achieving a critical size for continued growth. Nucleation preferentially occurs at the interface between guest fluid and liquid water [22]. The process is governed by the minimization of Gibbs free energy, and the competition between *surface* excess free energy and *volume* excess free energy. The favorable negative free energy change from phase transition must overcome the penalty from creating new surface area [6].

$$\Delta G = \Delta G^{surface} + \Delta G^{phase\ transiton} \leq 0 \quad (1.1)$$

For a spherical hydrate crystal, Kvamme expressed it as [5]:

$$\Delta G = A \cdot \gamma + \Delta G^{phase\ transition} \leq 0 \quad (1.2)$$

$$\Delta G = 4\pi r^2 \gamma + \frac{4}{3}\pi r^3 \rho_N^H \Delta g^{phase\ transition} \leq 0 \quad (1.3)$$

where A is the contact area for hydrate towards the surroundings, ΔG is the total excess free energy, γ is the interfacial tension [J/m^2], r is the crystal radius [m], $\rho_N{}^H$ is the molecular density [mole/m^3] and $\Delta g^{phase\ transition}$ is the intensive change in Gibbs free energy related to the phase transition [J/mole].

$\Delta G^{surface}$ can be seen as the push-work, or work needed to "push" old phases away, which is very important inside the nucleation period. In the nucleation period, Gibbs free energy increases until a critical radius is reached, where the growth process starts, and $\Delta G \approx \Delta G^{phase\ transition}$. The free energy change is negative, and the hydrate crystal grows without dispersing [5].

Induction time

There are developed various definitions of induction time, and following Volmer [23, 24] it can be defined as the period necessary for the appearance of the very first hydrate cluster of supernucleus size. A supernucleus size is reached when the cluster is capable of spontaneous growth to a macroscopic size. It is regarded as a measure of the ability of a supersaturated system to remain in the state of metastability, the ability of a non-equilibrium state to persist for a long period of time[24]. In other words, as it is defined by Sloan [6], the time elapsed until the appearance of a detectable volume of hydrate phase.

In contrast to the nucleation, which happens in a scale too small to be detected (a microscopic phenomenon), induction time is the time taken for hydrates to be detected macroscopically.

Growth

Gas hydrate growth will start after a critical size is reached. From this point, the growth rate will depend on water and gas accessibility, as well as heat transfer. Hydrate formation is an exothermic process, which can induce a local temperature increase. The increased temperature can counter act the formation.

The High-Pressure Hydrate Study is conducted at constant temperature, with the assumption of good heat transfer throughout the core. The limiting factor will be mass transport, the accessibility of water and gas, as initial hydrate films at the interface will act as barriers for further growth.

1.3.2 Hydrate Dissociation

In contrast to formation, dissociation is an endothermic process. Basically, as formation happens within the hydrate stability conditions, dissociation happens outside. These conditions can be met in several ways, mainly through (as shown in Figure 1-6):

(i) Pressure reduction
(ii) Temperature increase
(iii) Equilibrium-curve shift

Temperature and pressure change may be more intuitive, than the equilibrium curve shift. However, different methods are applied depending on the target. For example, a process engineer can use inhibitors to *prevent* hydrate formation in the well, this will shift the equilibrium curve making the hydrate-stabile conditions harder to reach. Examples of inhibitors are, amongst others, salt and alcohols [25, 26]. An interesting aspect is how salt content will affect the hydrate formation curve, since hydrates are found in saline marine environments. This will be described in the next chapter.

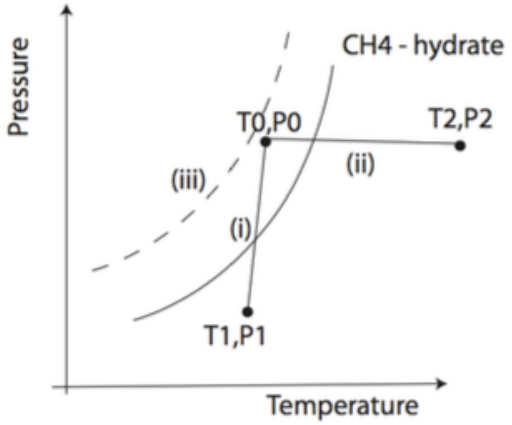

Figure 1-6: Hydrate formation curve with different dissociation methods. (i) Pressure reduction, (ii) Temperature increase, (iii) Equilibrium curve shift. The point (T0,P0) is inside hydrate stable conditions for scenario (i) and (ii), but outside when the curve is shifted in scenario (iii).

1.3.3 Production Scenarios

For a production perspective, the most economically sensible and energy efficient choice would (in most cases) be pressure reduction [5]. This brings the gas hydrate outside of its stable condition, where melting converts the solid over to fluid, releasing water and gas. The methods proposed can be in combination with thermal injection and/or inhibitors. This will be illustrated in the summary of field tests in *chapter 1.5.3*. A possible negative consequence of this production scenario, is the reduction of geo-mechanical stability in the ground. Assuming the solid gas hydrate contributes in holding the sediments together, and stabilize the ground, removing them could lead to landslides [27].

A proposed solution to this problem is introduced by another production method. A method proposed for methane production from gas hydrates, is the injection of the more stable guest, carbon dioxide [26]. Several studies have been conducted on this area. Graue et al. (2008) have shown that injection of liquid CO_2 in methane hydrates in sandstone cores leads to methane production, in addition to other benefits [28]:

(1) The conversion of methane hydrate into carbon dioxide hydrate takes place without adding heat to the system
(2) The conversion happens with no dissociation to liquid water. See Figure 1-7.
(3) CO_2 hydrates offers a stable long-term storage of a greenhouse gas

However, studies have shown that the conversion will be most efficient in the near well area, because of low mass transport. It has been suggested to add other chemicals in the gas mix, to create temporary dissociation, better permeability, and reach further into the formation. An example is adding nitrogen, which will reduce the thermodynamic driving force for the formation of new hydrate from injected gas and free water in the pores [2].

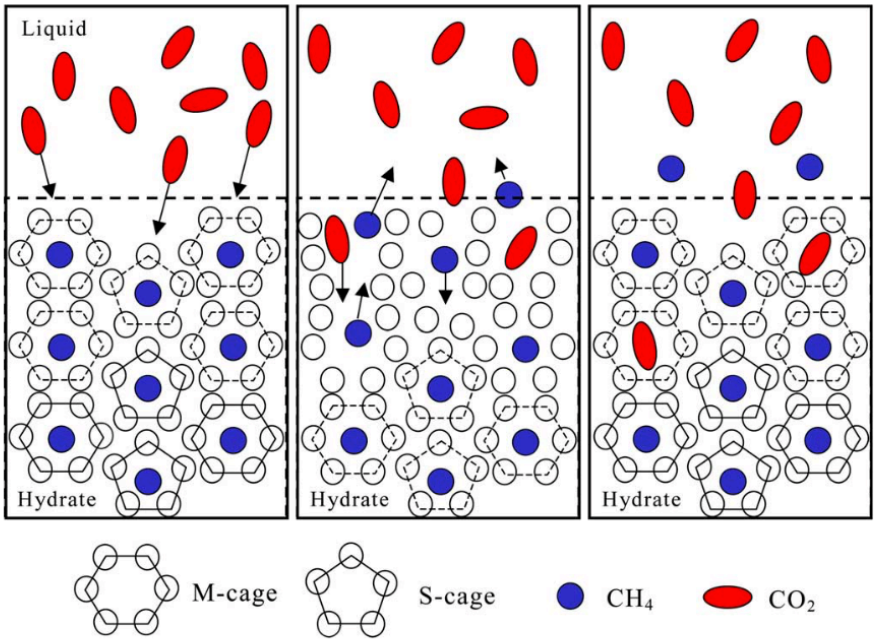

Figure 1-7: A schematic diagram of the guest molecule replacement, methane (CH_4) is exchanged with carbon dioxide (CO_2) in the large (M) cages [29].

1.4 HYDRATES IN NATURE

Natural gas hydrates can be found in regions that fulfill the requirements described previously. This can occur in permafrost regions of the arctic and in deep-water parts of most continental margins worldwide [16, 30]. The gas hydrate stability zone (GHSZ) can be defined by the phase diagram. For marine hydrates, limits are determined by bottom water temperature, sea level, geothermal gradient, gas composition and pore water salinity [31]. Figure 1-8 shows the different GHSZ for (a) marine and (b) permafrost regions [1].

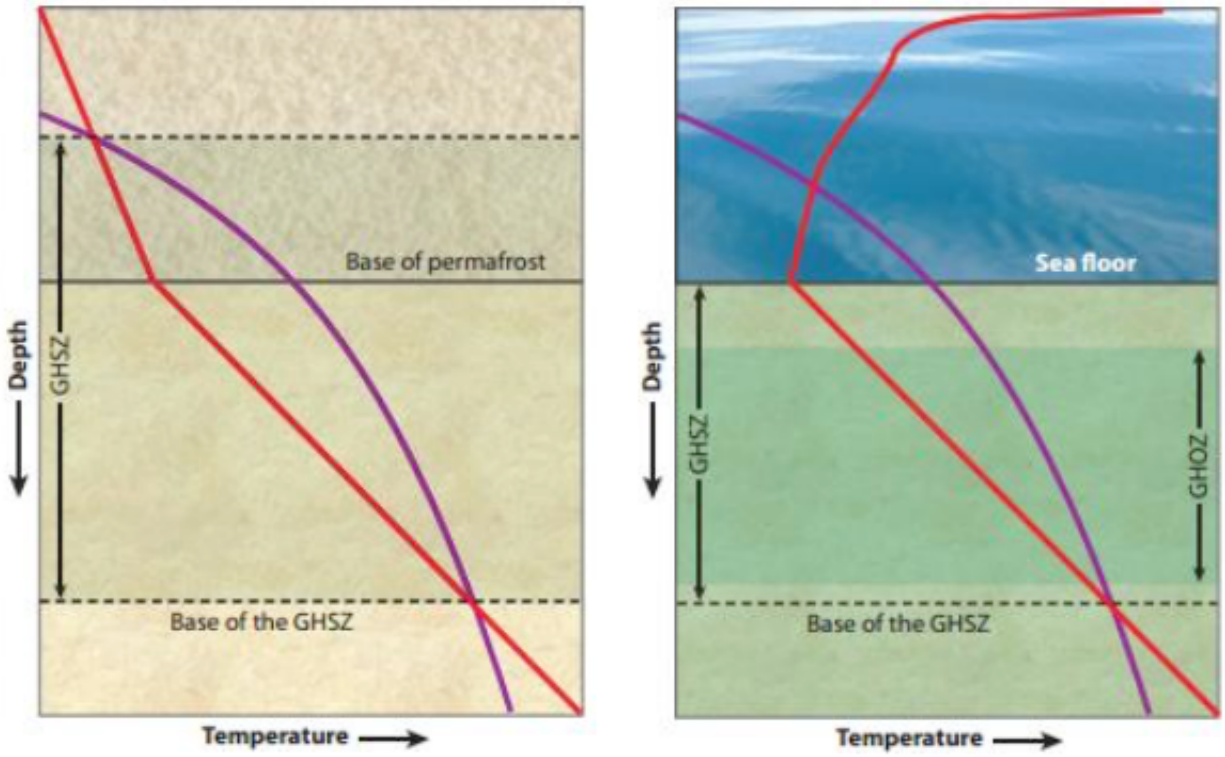

Figure 1-8: Gas hydrate stability zones for (a) permafrost and (b) marine regions. Red curve is the temperature profile, and the purple is the hydrate stability curve (or phase boundary curve). GHOZ is the gas hydrate occurrence zone, depending on gas availability. For permafrost systems, the GHSZ typically occurs around 100-300m depth, and can extend hundreds of meters. The temperature range is from – 10 to 20°C. For marine systems, the GHSZ typically starts below 300-600m of water depth, and can extend hundreds of meters below the sea floor. The temperature range is from 2 to 20°C. Figure from [1].

1.4.1 Gas Sources

The gas may originate from two sources from the ground, biogenic or thermogenic. The first, biogenic, comes from microbial activity in the upper several hundred meters of deep sea sediment. Biological degradation mainly creates methane. High content of methane will therefore be a good indicator of biological source. Methane hydrate is the most abundant of natural gas hydrates, estimated as high as 99% of all natural deposits. Because of the low carbon number, biogenic sources primarily lead to structure I hydrates [5, 32].

In contrast, thermogenic sources come from greater depths, and are thermal breakdown of organic material. Compounds with carbon number above C7 will end up as conventional hydrocarbons, however, compounds under C7 can form hydrates if migrated within hydrate stable zones. Depending on carbon number, thermogenic sources can form structure I (C1, C2, CO_2), structure II (C3, C4) and structure H (C4-C7) [5, 32].

Figure 1-9 illustrates gas hydrate regions, both in permafrost and oceanic, in addition to their possible sources.

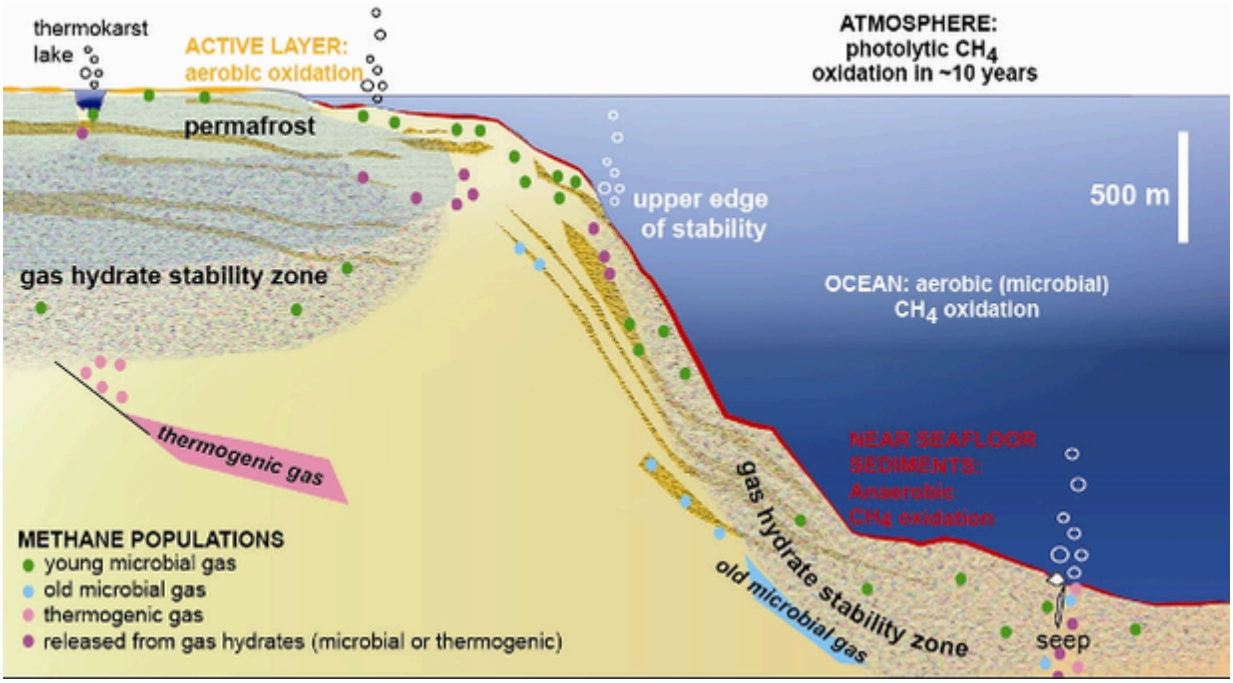

Figure 1-9: Illustration of hydrates in nature and their possible gas sources [30].

1.4.2 Hydrate Reservoirs and the Gas-Hydrate Resource Pyramid

Gas hydrates are often distributed in very low concentrations, over very large areas. Lithology may exercise a primary control of deposition, resulting from permeability, faults and traps. The distribution is heterogeneous, and are observed occupying (1) pores of coarse-grained rocks; (2) nodules disseminated within fine-grained rocks; (3) solid, filling fractures; or (4) a massive unit, mainly of solid gas hydrate with minor amounts of sediment [16]. See examples in Figure 1-11. Formation happens preferentially in coarse-grained sands, because lower capillary pressures in these sediments permit the migration of gas and the nucleation of hydrate [33]. Clay and shale are the most common trapping in marine hydrates, however also ice can act as a trap in permafrost.

Most natural hydrates are found in marine environments. Yet, gas hydrate found in permafrost is the most promising for production. It is distinguished between three commonly cited classes of hydrate reservoirs in permafrost [6, 25, 34]. The classes are illustrated in Figure 1-10. Following Moridis and Collett are [35]:

Class 1: Two accumulation layers: Hydrate layer underlain by two-phase zone of mobile gas and water (illustration A & B in Figure 1-10)

Class 2: Two zones: Hydrate layer underlain by one-phase zone of mobile water (C)

Class 3: A single zone: Hydrate layer with absence of underlying zones of mobile fluids (D)

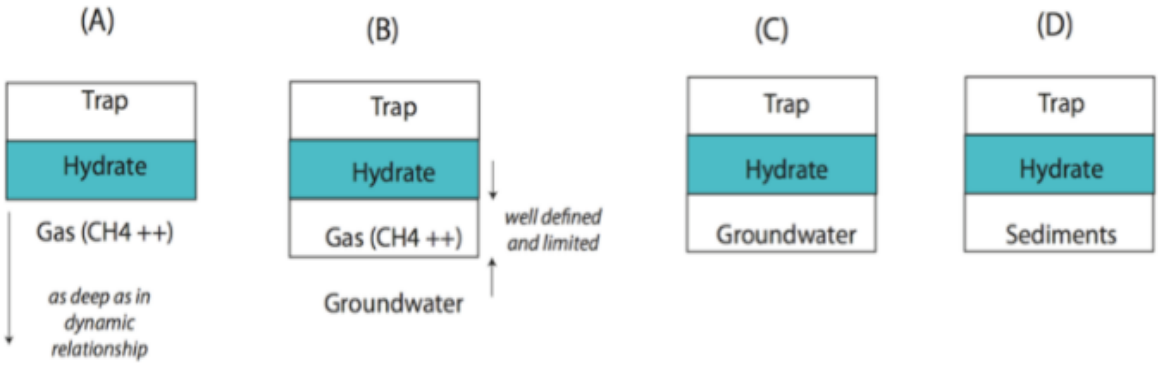

Figure 1-10: Illustration of hydrate reservoir classes. (A) and (B) are examples of class 1, (C) is class 2, and (D) is class 3. Illustration made from notes in [5].

The first class is the most promising in production, because the thermodynamic proximity to the hydration equilibrium requires only small changes in pressure and temperature to induce dissociation. In contrast to class 2 and 3, where the entire hydrate interval may be well within the stability zone [35].

Boswell and Collett (2006) proposed four different gas hydrate play types and compared them within a gas hydrate resource pyramid, seen in Figure 1-11. The resource pyramid displays the relative size and potential production value of the different types of resources. The most promising resources are found at the top, and the most technically challenging at the base [36].

The four gas hydrate play types are [16]:
(1) sand-dominated reservoirs,
(2) clay-dominated fractured reservoirs,
(3) massive gas hydrate formations exposed on the sea floor,
(4) low concentration, disseminated deposits encased in mostly impermeable clays.

Figure 1-11, displays also examples of different gas hydrate occurrences. According to Boswell and Collett, occurrences closest to potential commercialization exists:

- at high saturation
- within quality reservoir rocks
- under existing arctic infrastructure

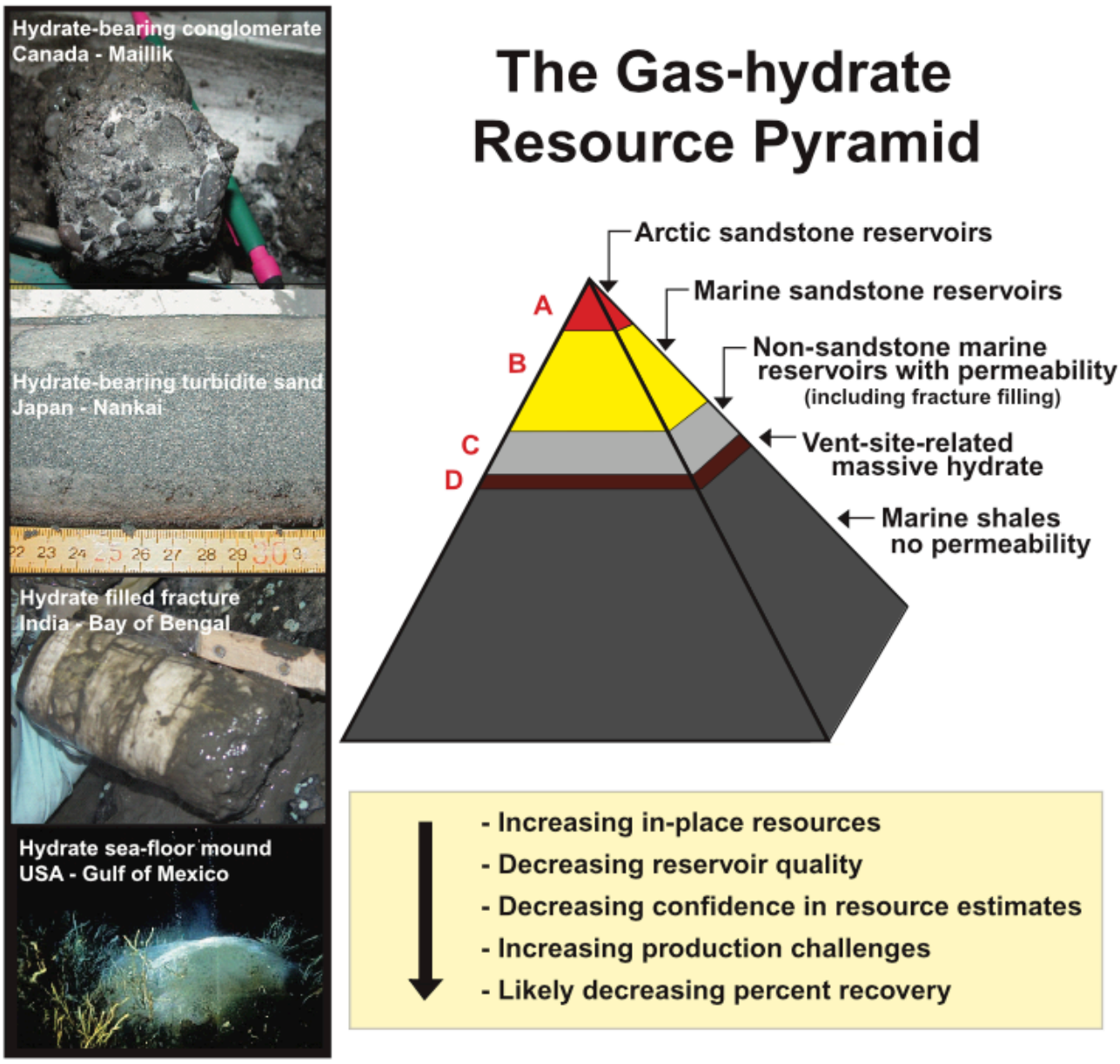

Figure 1-11: Gas hydrate resource pyramid. Illustrates the types of expected gas-hydrate reservoirs, and relative volume of gas hydrate in each type. Images to the left shows different examples of gas hydrate occurrences [16, 36].

1.4.3 Field Tests

There are some needs to be met in order to allow for a commercially and environmentally safe gas extraction from gas hydrate deposits. Current technology, from exploration through production to monitoring, must be further developed and adapted to be able to handle the challenges of gas production from gas hydrates. Also, research on gas hydrate characteristics and behavior, especially within sediments, are essential to be able to exploit this resource.

Various academic groups and companies have been involved in theoretical and applied research on hydrate gas extraction for more than a decade. A summary of completed field test, from a recent report from COST (European Cooperation in Science and Technology) and MIGRATE (Marine Gas

Hydrate), 2017, are found in Table 1.2, corresponding locations are found in Figure 1-12 [3]. Some of the typical issues met are sand production and injectivity problems.

COST and MIGRATE did not include the most recent record of the natural gas extraction volume from offshore gas hydrates, reached by China in May 2017 [37]. Reported by Rauters, July 29, they successfully produced natural gas from methane hydrate. The drilling platform deployed off the coast of the southeastern Chinese city of Zhuhai for 60 days, produced a total of 309,000 cubic meters of natural gas.

Table 1.2: Completed field test reported by COST and MIGRATE by August 2017 [3].

Year	Location	Description	Duration (h)	Gas production rate (Nm^3/h)	Water production rate (Nm^3/h)	Total gas production (Nm^3)	Total water production (Nm^3)
2002	Mallik 5L-38, Canada	Thermal stimulation	124	4	---	470	---
2007	Mallik 2L-38, Canada	Short pre-test by depressurization	12.5	70	---	830	20
2008	Mallik 2L-38, Canada	Depressurization	144	60-700	0.2-0.6	13000	---
2011	Qilian Mountain, China	Depressurization + thermal stimulation	101	1	---	95	---
2012	Prudhoe Bay, Alaska	CO_2-injection (N_2:CO_2 77:23%) by depressurization	936			24000	180
2013	Nankai Trough, Japan	Offshore field test by depressurization	144	840		120000	1100

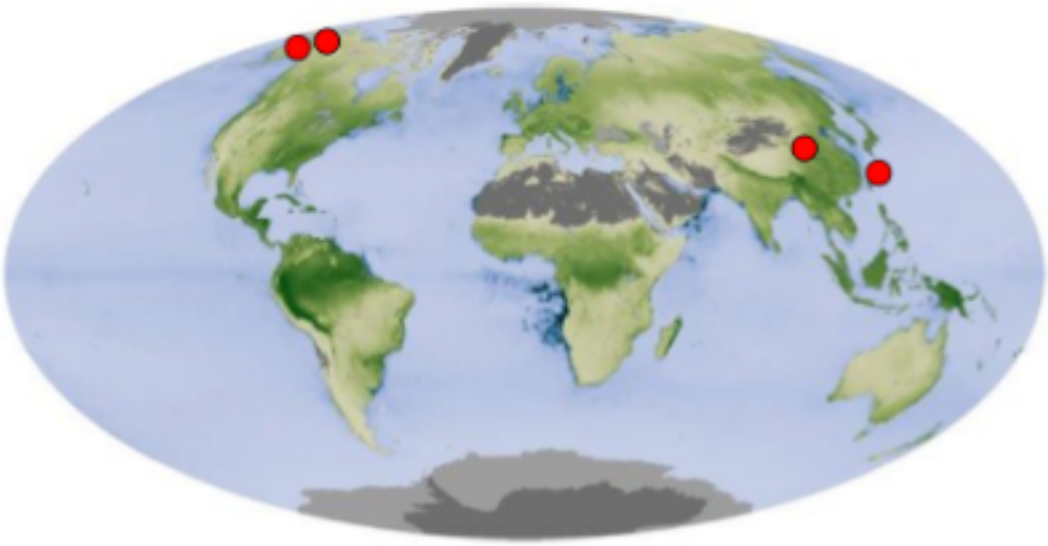

Figure 1-12: Map of previous production field test sites [3].

1.4.4 Pore-scale Hydrate and Permeability Dependency

As the last chapter pointed out, knowledge about the characteristics of hydrate in the porous media is essential for production evaluations. An important factor in most petroleum productions is the permeability of the pore media. This section will look at hydrate formation in a pore and permeability dependencies, Figure 1-13 is used in the explanation [5].

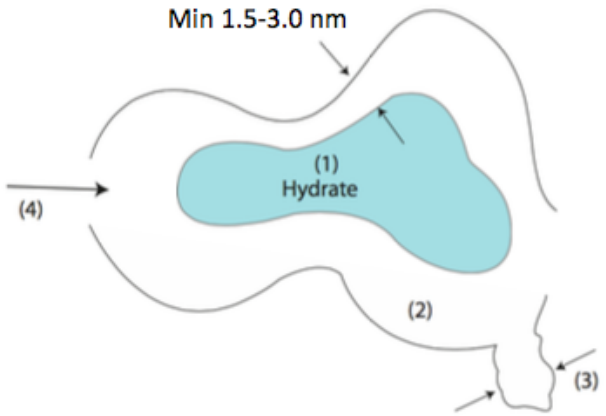

Figure 1-13: Illustration of hydrate in a pore. The four regions are discussed in the text under. Illustration is based on notes from a course by Bjørn Kvamme, 2016 [5].

1) Hydrate can never touch the mineral surface, because of the partial charge distribution on atoms in the surface and partial charges of the water molecules of the hydrate. This results in a minimum of 1.5-3.0 nm structured water separate hydrate from the mineral surface.

2) Mineral surfaces are most often water wetting, and adsorbs water well. Some hydrate formers can adsorb directly, like for instance CO_2 on calcite. Also, many different hydrate formers can adsorb secondary in pockets of low water density. Hydrate guests can be trapped in these pockets and up concentrated; mineral surfaces cannot connect to hydrate directly, but mineral surface can lead to up-concentration of hydrate formers, and then also result in hydrate nucleation.

3) Pore bounded water have additional mechanical constraints. It is believed that an approximately 4-7 nm is the minimum pore diameter for which the hydrogen bonded network can survive.

4) If the space between hydrate and mineral is filled with water, then permeability of water depends on:
    a. Hydrate saturation
    b. Interface stress (friction) between hydrate and liquid, and mineral and liquid.
    c. Salinity
    d. Possible other phases in the pore (Hydrocarbon liquid or gas, etc.)

2 FUNDAMENTALS MAGNETIC RESONANCE IMAGING

This chapter will first give an introduction of basic principles of magnetic resonance imaging (MRI). Thereafter, the focus shifts to MRI applications in core analysis relevant for this thesis.

Magnetic Resonance (MR) is based upon the interaction between a *nucleus that possesses spin* and an *applied magnetic field.* The technique uses ideas of *resonance absorption* and *relaxation* of the spinning nucleus to create images [38].

2.1 A SPINNING NUCLEUS

Almost all elements in the Periodic Table have at least one naturally occurring isotope that possesses the property of nuclear spin. The property of spin depends on the relationship between protons and neutrons in the nucleus. A spinning nucleus produces a magnetic field, known as the magnetic moment, see Figure 2-1.

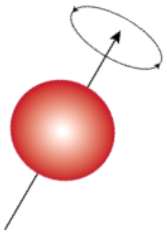

Figure 2-1: A rotating nucleus. The axis of rotation can be viewed as a vector, μ, with magnitude and direction. The magnetic moment is oriented parallel to the axis of rotation.

In principle, all elements that have this property can be examined by MR techniques. However, this text will focus on the ^{1}H nucleus, consisting of a single proton. This is the most common choice for MR applications. One of the reasons is that the ^{1}H nucleus' response to an applied magnetic field is one of the largest found in nature (another because tissues in the human body consist primarily of water and fat) [38].

2.2 THE APPLIED MAGNETIC FIELD (AND FORMATION OF NET MAGNETIZATION)

A sample of hydrogen nuclei in a natural/neutral magnetic environment consists of randomly oriented spins (Figure 2-2, left). Because spins in all directions will equalize each other out, a vector addition of all the spins, $\boldsymbol{\mu}$, will be equal to zero [$\sum\boldsymbol{\mu} = 0$]. If the sample is placed in a magnetic field $\boldsymbol{B_0}$, however, (some of) the spins will align either parallel or anti-parallel to this field (Figure 2-2, right). A vector addition in this situation will give a *net magnetization,* $\boldsymbol{M_0}$, parallel to the applied $\boldsymbol{B_0}$ [$\sum\boldsymbol{\mu} = \boldsymbol{M_0}$]

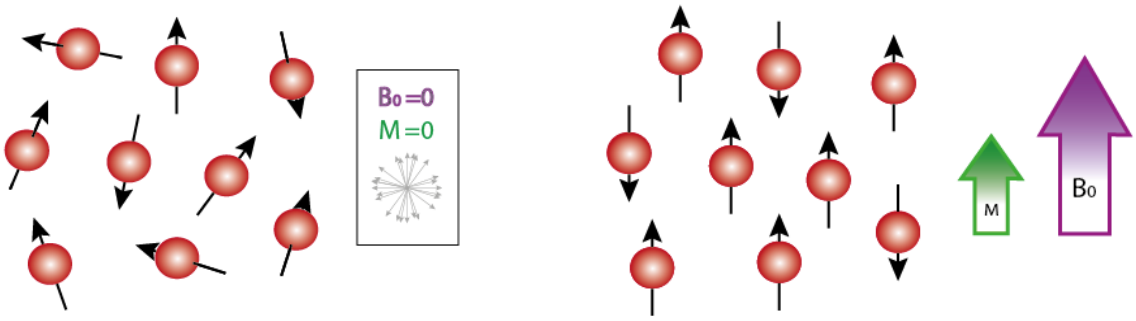

Figure 2-2: Left: Illustration of randomly oriented spin that equalize each other. No net magnetization. Right: Illustration. The spins are oriented parallel or anti-parallel to the applied magnetic field, B_0. There are more spins aligned parallel than anti-parallel. A vector sum in this environment will give a net magnetization M_0, parallel to B_0.

The protons aligned parallel with $\boldsymbol{B_0}$will have a coupling with $\boldsymbol{B_0}$, known as the Zeeman interaction. This causes a difference in energy, ΔE, between the protons aligned parallel and anti-parallel with $\boldsymbol{B_0}$, where the parallel protons have lower energy than the anti-parallel.

The illustrations in Figure 2-2 are simplifications; the protons are actually tilted slightly away from the z-axis ($\boldsymbol{B_0}$ direction), but the axis of rotation is parallel to $\boldsymbol{B_0}$ (Figure 2-3). This is a movement known as precession, and occurs because of the interaction between the spinning charge of the nucleus and the magnetic field [38]. The rate of precession is proportional to the strength of the magnetic field, and is expressed by the Larmor equation, where ω_0 is the Larmor frequency [MHz], $\boldsymbol{B_0}$ is the magnetic field strength [T], and γ is the gyromagnetic ratio [$s^{-1}T^{-1}$]:

$$\omega_0 = {}^{\gamma B_0}/_{2\pi} \qquad (2.1)$$

The protons' precession is of constant rate and magnitude around the z-axis, (Figure 2-3 Left), as a result the z-value will be constant, but there will be a wide range of x- and y-values. The coordinates parallel to $\boldsymbol{B_0}$, (here z-direction), are called *longitudinal,* and the perpendicular (x- and y-coordinates) is called *transverse*.

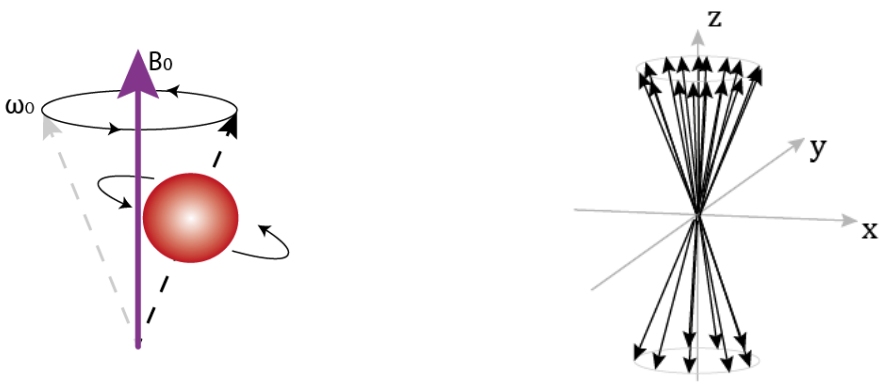

Figure 2-3: Left: The protons precess about the applied magnetic field B_0 (it moves like a "spinning top"). Right: Illustration of spins parallel and anti-parallel to B_0 (defined in z-direction). A vector sum gives a net magnetization M_0, in + z-direction. The vectors in this illustration will rotate about the z-axis. (It can also be viewed as a rotating system: x and y rotating about the z-axis, with stationary vectors).

2.3 ABSORPTION AND RELAXATION

The MR experiment is basically an energy transfer. The sample examined is exposed to energy at the correct frequency that will be *absorbed*. The energy will then be reemitted a short time after, known as *relaxation,* Figure 2-4. This generates a signal that can be detected and processed.

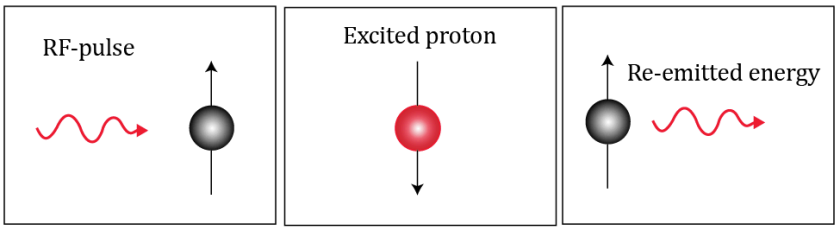

Figure 2-4: Illustration of a proton that absorbs RF- energy, and re-emits it a time after. Notice how the spin changes direction when the proton is excited to the higher energy state.

2.3.1 Absorption

Another way to describe the MR technique is as a manipulation of the net magnetization vector $\boldsymbol{M}$. The frequency that is absorbed by the protons is called the resonance frequency (RF). If the sample is exposed to a pulse with this frequency (a RF pulse), both the low- and high-energy protons will be affected. The low energy protons will absorb the energy and excite to the higher state, but the high-energy state protons will be generated to emit their extra energy and fall down in the lower energy state.

Because there are more "spin-up", than "spin-down" protons, there will be a net absorption in the sample, which causes a change in the net magnetization. If the sample is exposed to the RF pulse for a long enough time, $\boldsymbol{M}$ will rotate from the z-axis and into the transverse plane, known as a 90° pulse, Figure 2-5.

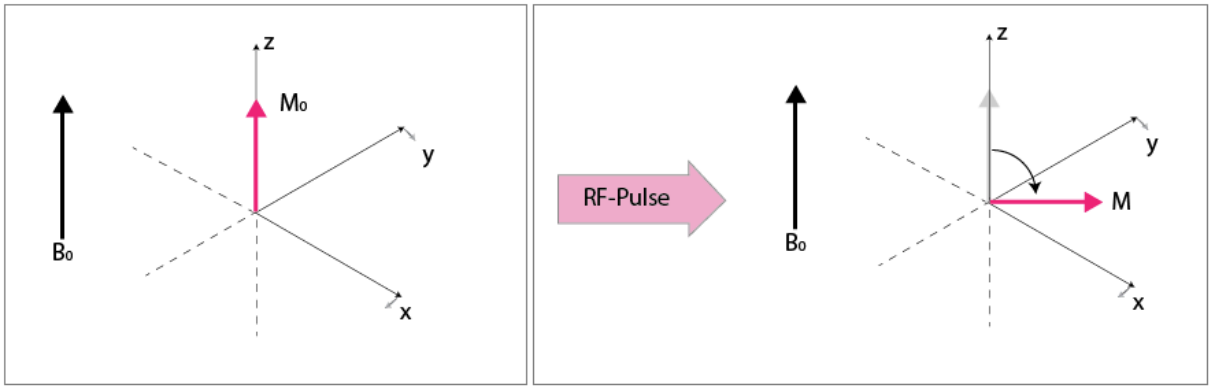

Figure 2-5: Illustration of how the net magnetization vector M_0 is rotated by a 90° pulse. M_0 start as longitudinal, but is rotated into the transverse plane. This illustration uses a rotational coordinate system.

2.3.2 Relaxation

When the RF pulse is turned off, the protons start to emit the energy absorbed. Relaxation is basically this release of energy, and the restoring of the protons original orientation. *Back to the state of equilibrium.*

The release of energy causes a voltage in the receiver coil, (description of the MR instrument will be given in chapter *6.1.1 Main Components of the MRI*). This is the MR signal, known as the FID (free induction decay). The FID is a wave function and is measured as a function of time, but will for practical

reasons be Fourier transformed to a function of frequencies. In other words, the signal is transformed from digital to analog. There are three aspects of the FID signal that are of interest:

- Magnitude of the signals amplitude
- Frequency
- Phase relative to the RF transmitter phase

There are two relaxation times that can be measured, T1 and T2. The two processes measure energy transfer, but differ in the final disposition of energy. They also focus on different magnetic components of net magnetization vector $\boldsymbol{M}$ [38].

2.3.3 T1 Longitudinal Relaxation Time

"The relaxation time T1 is the time required for the z component of $\boldsymbol{M}$ to return to 63% of its original value following an excitation-pulse" [38]. T1 is also known as the *Spin-Lattice* relaxation because it looks at the energy transfer from the protons to the surroundings, rather than proton to proton (T2).

Immediately after a 90°-pulse, all magnetization will be in the transverse plane (*xy*). The $\boldsymbol{M_z}$ component starts to grow as the spins start to realign along the longitudinal axis. T1 is therefor also known as the longitudinal relaxation. The $\boldsymbol{M_z}$ component follows an exponential growth process, Equation 2.2, visualized in Figure 2-6:

$$\boldsymbol{M}_z(\tau) = \boldsymbol{M}_0\left(1 - e^{(-\tau/T1)}\right) \qquad (2.2)$$

where τ is the time, and $\boldsymbol{M_0}$ the original value of the net magnetization.

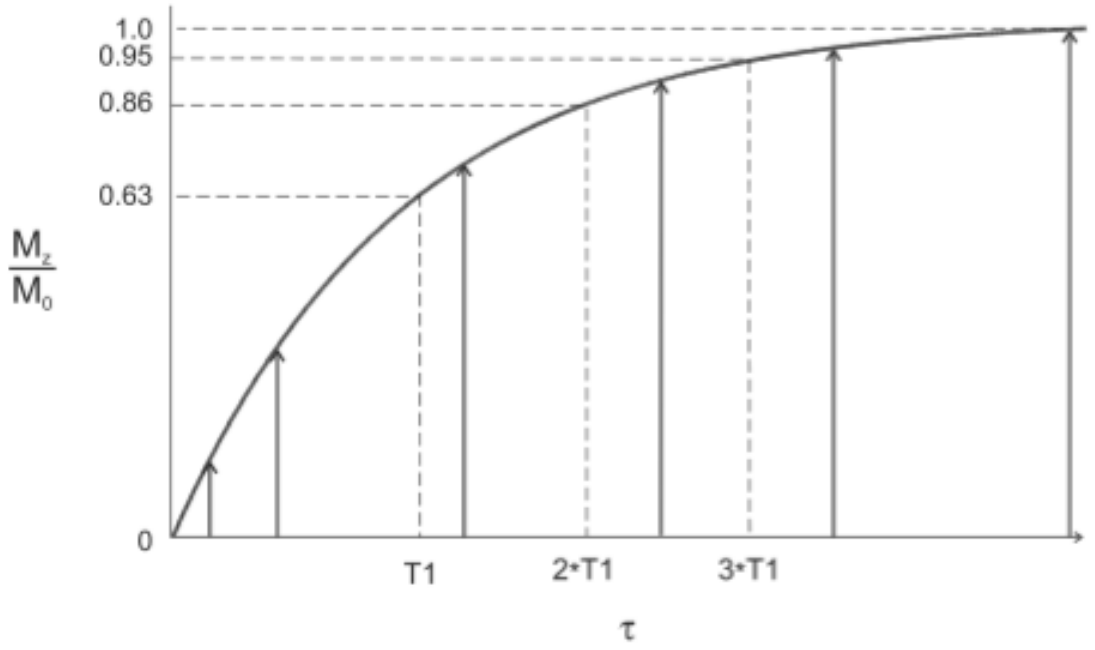

Figure 2-6 T1 relaxation curve[38]. Enough RF energy has been applied for all of the magnetization to be rotated into the transverse plane. As a consequence, the initial M_z = 0. As time goes by, more and more spins realign along the longitudinal (z) axis and M_z grows towards M_0 . After one T1 relaxation time 0.63% of M_0 is restored, and 95% after three T1 relaxation times.

2.3.4 T2 Transverse Relaxation Time

On the other hand, T2 relaxation time is a characteristic time representing the decay of the initial *transverse* component of $\boldsymbol{M}$, by $1/e$ (≈37%), via an irreversible process [39, 40]. The transverse relaxation is the result of random interactions, at atomic and molecular levels [8].

T2 is referred to as *spin-spin relaxation* because of the interaction between the spins (Figure 2-7), and *transverse relaxation time* because it describes the relaxation in the transverse magnetization plane.

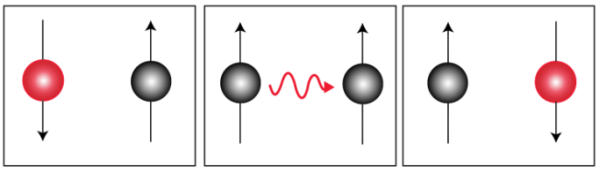

Figure 2-7: "Spin – Spin". Protons can absorb energy released from a nearby proton, if they have the same reference frequency.

The transverse component is made of protons spinning in phase: right after the excitation pulse, all the rotated protons start spinning at the same point, with the same frequency. As a result, all the spins are in phase in the transverse plane at start, but as time goes by they start to spin differently. In other words, the spins de-phases with time, see Figure 2-8.

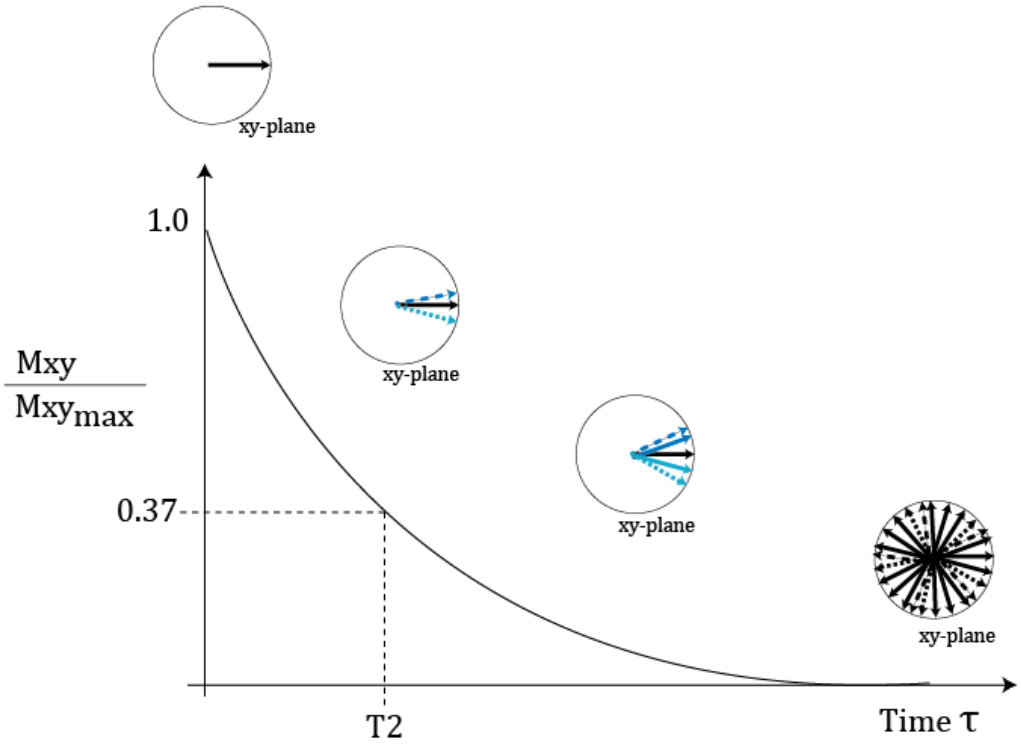

Figure 2-8: The curve illustrates how the transverse magnetization vector decays. At time τ = 0: the 90°-pulse is just turned off and there is phase coherence amongst the spins in the transverse plane, as shown in the top circle. As time goes on more and more protons release their energy and goes out of phase, as the following circles demonstrates. The release of energy generates the signal in the FID. At the end, all the spins are de-phased, and equalize each other out, resulting in M_{xy} = 0, as shown in the last circle. Figure modified from [8, 11].

T2 vs. T2*

In reality, there are more reasons for this dephasing than the molecular vibration/rotations causing the spin-spin relaxation, or "the true T2". The sample will never experience a uniform homogenous magnetic field, $\boldsymbol{B_0}$, which will locally affect the precession of the protons resulting in de-phasing [38, 39]. (*See the Larmor equation 2.1*).

T2* is the observed or *effective T2*, which are affected by the inhomogeneities, while T2 is the true, and always larger or equal to T2* (T2 ≥ T2*). The relationship can be written as [39, 41]:

$$\frac{1}{T2^*} = \frac{1}{T2_{(true)}} + \frac{1}{T2_{inhom}} \qquad (2.3)$$

The magnetic field inhomogeneity will be eliminated by the 180° pulse in spin-echo imaging, which results in T2 weighed magnetization [39].

2.3.5 Measurement techniques

There are several techniques and sequences developed to measure T1 and T2. This thesis will focus at T2, using the spin echo sequence CPMG (Carr-Purcell-Meiboom-Gill). CPMG consists of one 90° pulse (excitation) followed by multiple 180° pulses (refocusing), illustrated in Figure 2-9.

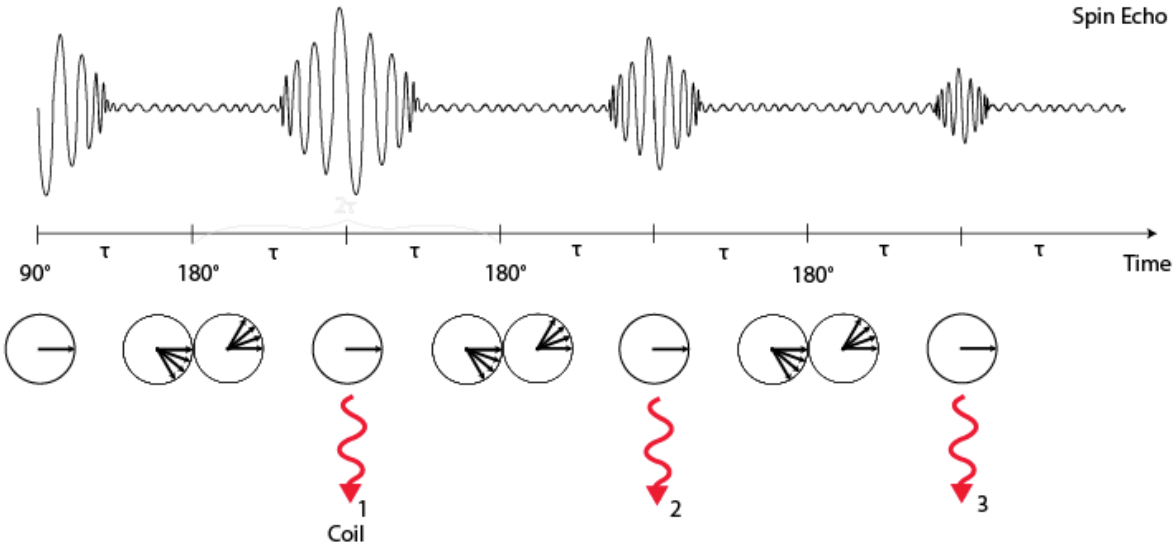

Figure 2-9: Illustration of echo development after one 90° (excitation) pulse, and three 180° (refocusing) pulses. Red wave arrows represent when the coil is receiving signals. Circles with arrows shows how the spins are de-phasing. Right after a 90° pulse all spins are in phase, as time goes on they start to de-phase. A refocusing pulse flips them 180° which makes them return and in one point meet again in phase (signal), but then they will continue to de-phase. A new refocusing pulse is added, and so on.

The echoes generated by the 180°pulses will be larges at start, and then decay with time, Figure 2-9, until it fades away when all spins are relaxed. This decay in echo magnitude, can be plotted over time, and give a decay curve following this exponential function:

$$y(t) = B + Ce^{-t/T2} \quad (2.4)$$

where C will be the initial intensity (cross-section with the y-axis), and B the offset of the curve.

2.4 T2 IN POROUS MEDIA

T2 for water in porous media will be shorter than for bulk fluid. The reason is that protons will collide with the solid surface of the pore walls, which will accelerate the relaxation (time). For core analysis, and the presence of a pore medium, it is important to choose a shortest possible echo time, due to the rapid decay. Longer echo times will not pick up enough information in the beginning, which will not be representative for the sample, especially is this sensitive for the C-value in Equation 2.4.

2.4.1 Porosity from the Signal Decay Curve

An interesting feature of decay curve is the initial signal intensity. Theoretically, porosity, ϕ, can be estimated, if the initial intensity for bulk water I_b, and initial intensity for water in the porous media I_p, is known:

$$\phi = \frac{I_p}{I_b} \quad (2.5)$$

The initial signal intensities of the different decay curves are illustrated as dots in the figure below.

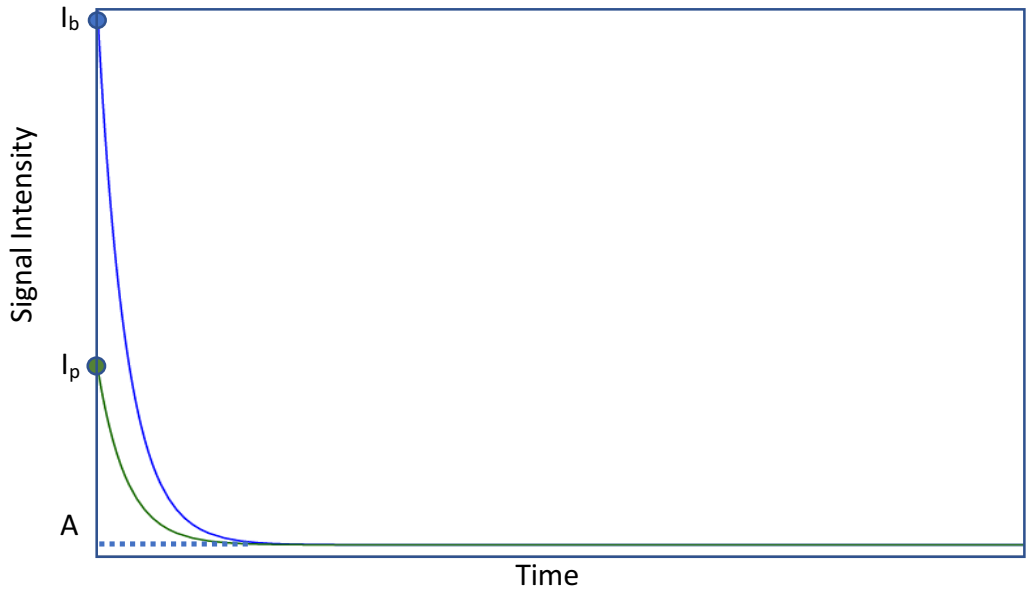

Figure 2-10: Illustration of difference in decay curves. Blue for bulk water and green for water in pores. Initial signal intensities are marked with points at the signal intensity axis, I_b for bulk water, and I_p for water in pores.

2.4.2 Pore Size Distribution from T2

A pore size distribution of a rock can give important information about properties such as porosity, permeability, free fluid, bound water and saturation. T2 measurements can be used to determine the pore size distribution [4]. This can be done by inverse Laplace transformation of the decay curve, which generate a T2 distribution of the individual exponential components of the decay curve [42, 43].

To simplify this topic, first a single pore is described, then a system with three different pore sizes, and finally the pore volume of a whole core sample presented.

T2 of water in a single pore

The observed MR signal *M(t)* at time *t,* will follow this exponential decay:

$$M(t) = A_0 e^{-\frac{t}{T_2}} \quad (2.6)$$

Where A_0 is the initial signal amplitude, and T2 is the decay time. T2 will be dependent on different relaxation times, as described by *equation 2.7*.

$$\frac{1}{T_2} = \frac{1}{T_{2bulk}} + \frac{1}{T_{2S}} + \frac{1}{T_{2GR}} \approx \frac{1}{T_{2S}} \quad (2.7)$$

The water molecules at the pore surface will collide with the pore wall (T_{2S}), which will be different from the molecules in bulk water (T_{2bulk}), and molecules diffusing in a gradient (T_{2GR}). Equation 2.7 can be simplified so that all the relaxation comes from the surface, because rock pores are typically small enough to ignore bulk relaxation and there are no gradient effects in laboratory experiments[44]. T2 will therefore be related to the interaction of the water molecules with the pore wall and their distance from the wall, and will be proportional to the effective pore radius, expressed by Equation 2.8.

$$\frac{1}{T_{2S}} = \rho \frac{S}{V} = \rho \frac{3}{r} \quad (2.8)$$

S/V is the surface to volume ratio, r is the effective pore radius, and ρ is the surface relaxivity, which will depend on lithology. If ρ is known the pore size can be estimated.

T2 of water in pores of three different sizes

It can also be shown from Equation 2.8 that in large pores, which will have a low S/V, T2 relaxation will be long in contrast to smaller pores, which will have a high S/V. This can be seen in Figure 2-11.

The initial signal amplitude and the peak height of the T2 distribution reflect the respective volumes of the three different pore sizes. In the example shown in the figure the micro- and meso-pores each represent about ¼ of the volume, and the macro-pores the other half.

The total pore structure's NMR-signal curve is a sum of all relaxation curves (sum of all pore sizes), and is described as:

$$M(t) = A_{micro}e^{-\frac{t}{T_{2micro}}} + A_{meso}e^{-\frac{t}{T_{2meso}}} + A_{macro}e^{-\frac{t}{T_{2maro}}} \quad (2.9)$$

For this example, an analysis of the raw signal decay data produces three distinct T2 values representing three different pore sizes.

T2 of water in a rock core

By comparison, a core sample will have a range of different pore sizes, and will therefore produce a continuous spectrum of T2 values. The signal decay can be expanded to the following:

$$M(t) = A_a e^{-\frac{t}{T_{2a}}} + A_b e^{-\frac{t}{T_{2b}}} + \ \ldots + A_N e^{-\frac{t}{T_{2N}}} \quad (2.10)$$

An illustration of a T2 decay curve and corresponding T2 distribution map for a sandstone, shown in Figure 2-12.

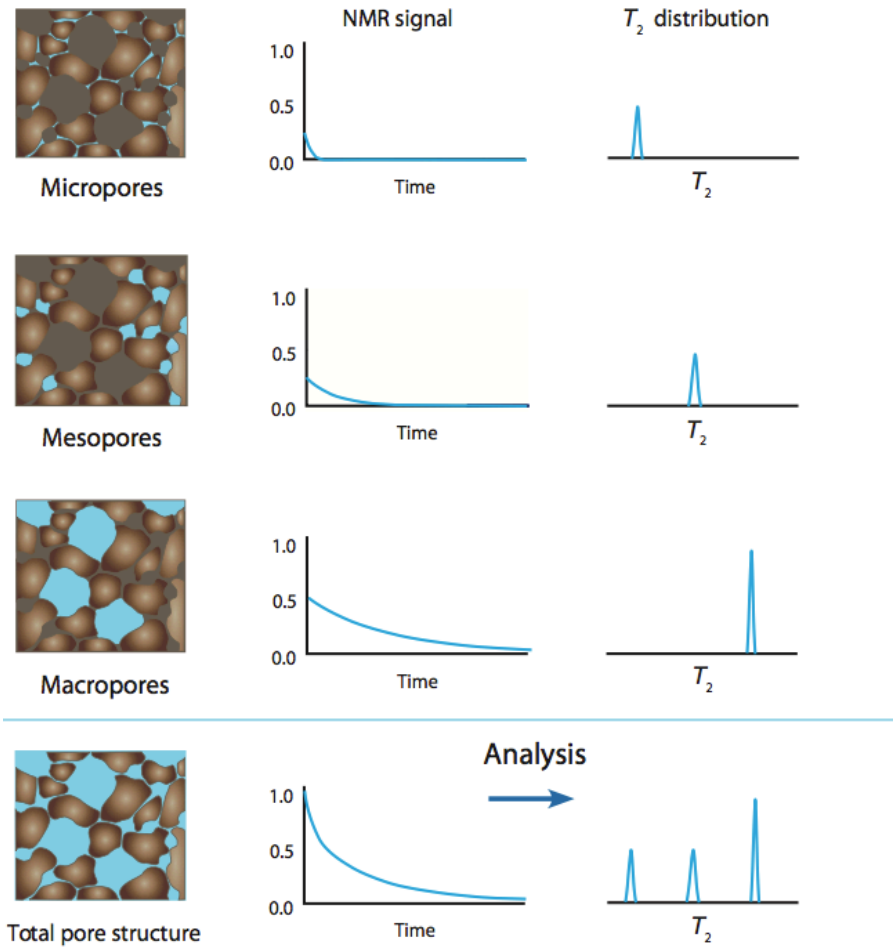

Figure 2-11: A model of a heterogeneous pore system, built from three different pore sizes, their signal decays and T2 distributions, and the sum of all. Figure [4].

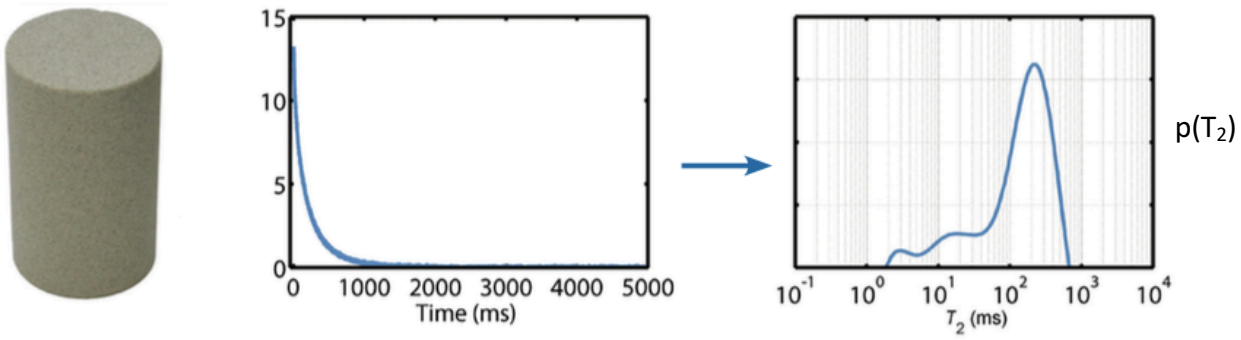

Figure 2-12: Example of a Berea sandstone core with the corresponding raw data NMR data and T2 spectrum [4].

In sum, two key observations are valuable for NMR studies of fluid saturated sediments:

- Smaller T2 values relates to smaller pores.
- The amplitude of each exponential is proportional to the total volume of pores at this size.

2.4.3 Porosity and Absolute Permeability from the T2 distribution

The T2- or pore size distribution map can be used to estimate porosity and the absolute permeability. Porosity can be estimated by a summarization of the whole T2 distribution, if the distribution is calibrated to a known porosity. Equation for porosity:

$$\phi = c \sum p(T_2) \qquad (2.11)$$

where c is a normalized constant from calibration to a water saturated porous media of known porosity [44].

The T2 spectrum is also used for the permeability estimation. There are developed several versions of the Kozeny-Carman equation. One version divides the spectra in contributions from trapped water versus mobile water [44]. Another permeability estimation is based the logarithmic mean $T_{2,LM}$ of the spectra, found in Equation 2.12. This equation has shown to be more suitable for a sandstone, rather than a carbonate system.

$$k = a\, \phi^b T_{2,LM}^2 \qquad (2.12)$$

with standard values $a = 1$, an $b = 4$ [45].

2.5 SPATIAL ENCODING AND K-SPACE

The main difference between NMR (nuclear magnetic resonance) and MRI (magnetic resonance imaging) is that NMR generates an overall *frequency spectrum*, whereas MRI measurements include *spatial dimensions - images*. To be able to do so, MRI takes advantage of spatial gradients. Spatial gradients are linear disturbances along $\boldsymbol{B_0}$, and are applied for short periods of time, called gradient pulses [38]. The magnetic-field will then be linearly dependent on the location inside the magnet:

$$B_i = B_0 + G_T \cdot r_i \tag{2.13}$$

where B_i is the magnetic-field at location r_i, and G_T is the total gradient amplitude.

There are three gradients in three directions perpendicular at each other (x,y,z):

1) SS – Slice selection
2) RO – Read out – Frequency encoding

$$\omega_i = \gamma(B_0 + G \cdot r_i) \tag{2.14}$$

3) PE – Phase encoding

which results in spatial dependency on the resonant frequency, ω_{RF}. The information gathered from all the radiofrequency signals generated, are stored in what is called *k-space*. Illustration of k-space reading are found in Figure 2-13. The signals are waves, and the "k" in k-space is a parameter used for:

$$k = \frac{wave\ cycles}{length} \tag{2.15}$$

k- space is a plot of all possible waves, meaning it is a kind of wave space, where all the points contribute to the whole picture. Where the point is located in the matrix depend on the waves magnitude and angle. Because waves are described by both frequency and phase, k-space is a matrix of real and complex numbers. The MR image is generated by Fourier-transform this matrix.

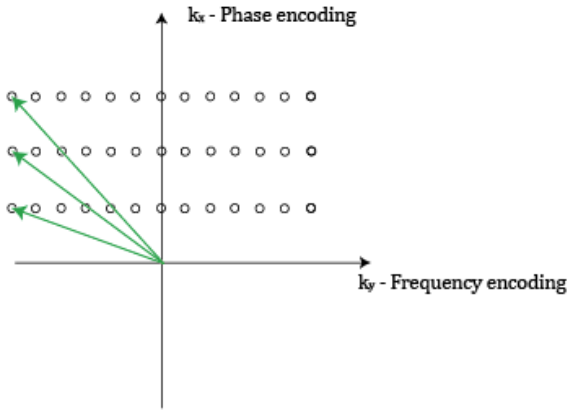

Figure 2-13:Illustration of k-space reading, phase encoding in x-direction and frequency encoding in y-direction.

A notable distinction, is that increasing the sampling rate results in no time penalty, but increasing the number of phase steps increases the time of acquisition proportionally. It can therefore be practical to use images that have fewer phase encodings than frequency encodings, (for example, 128 x 256).

2.6 MRI SIGNAL INTENSITY, WATER SATURATION AND GAS HYDRATES

An image generated from MRI, is built of "black to white" pixels. As mentioned before, hydrogen is the typical nucleus examined. In that case, the higher the pixel is on the white scale the denser the hydrogen concentration is in that location. It can be seen as a *hydrogen detector* where the scale measures the relative concentration in the sample.

2.6.1 Water Saturated Pores

When imaging a sandstone core filled with water, only water will generate signal. The matrix however, will not, and will be dark in the image. The resolution is normally not high enough to show pores. The fact that the signal is greater with higher hydrogen density, can be used to correlate signal intensities to water saturations, expecting a linear relationship. This will be shown in the saturation study described later.

2.6.2 Hydrate saturation

Only fluid or *mobile* water will be able to generate signal. If water freezes to ice, or form hydrates, their T2* will be too short to detect. As a result, gas hydrate formation is inferred from a loss of signal in MRI measurements [8, 46].

2.6.3 Saturation estimations

Assuming linear relationship between MR signal intensity and water saturation, change in saturation can be found by using the measured intensity, I, initial water saturation, $S_{w0,}$ and corresponding mean intensity I_0. Water saturation, S_w, can be estimated from:

$$S_w = \frac{I \cdot S_{w0}}{I_0} \cdot 100\% \qquad (2.16)$$

The loss of water saturation can be used to estimate saturation of hydrate formed. If the volume ratio, R_v, from water to hydrate is known, the saturation of hydrate and gas can be estimated from [47]:

$$S_h = R_v \frac{(I_0 - I) \cdot S_{w0}}{I_0} \cdot 100\% \qquad (2.17)$$

$$S_{gas} = 1 - S_w - S_h \qquad (2.18)$$

Yang et al. (2010) used R_v = 1.25. Since the hydrates concentrate former gas as much as a factor of 164 and 0.8 water (at standard temperature and pressure) [6], they assumed that one volume of water molecules can convert into 1.25 volume of hydrate [47].

3 LITERATURE SURVEY

The following literature surveys addresses relevant research on hydrate phase transitions from MRI/NMR measurements.

3.1 MRI: HYDRATE FORMATION AND DISSOCIATION

Baldwin et al. (2003) wanted to determine whether it was possible to develop a method, using MRI to monitor hydrate formation and dissociation. They studied THF (tetrahydrofuran) hydrates, both in a Berea sandstone and in bulk (a combination that will form hydrate at ambient pressures). They concluded that MRI was shown to be an effective tool for detecting the formation of hydrate with excellent contrast between the hydrate phase and the individual hydrate components. In addition, they concluded that MRI can be used to determine the spatial distribution of the hydrate and non-hydrate phases and quantify the rate of hydrate formation and dissociation [48].

3.2 MRI: CH4 – CO2 EXCHANGE

Graue et al. (2006) used MRI to visualize the conversion of CH_4 hydrate into CO_2 hydrate, in the porous media of a Bentheim sandstone. A number of experiments were conducted. Hydrate formation was monitored by the loss of signal intensity as water and free gas are converted into solid phase [28]. This signal-loss method studying CO_2 hydrates, have been used in several studies since then, amongst others, Ersland et al. (2009, 2010), who concluded that MRI provided excellent images of high resolution that distinguished between the hydrate and its liquid/gas precursors, and allowed for dynamic, spatial imaging of the formation and reformation of hydrates in the porous sandstone [46, 49]. Another study, by Husebø et al. (2009), used the same method to look the effects of salinity on CO_2 hydrate stability [50].

3.3 T2 DISTRIBUTION MAPPING

Kleinberg and Griffin (2004) used NMR measurements to investigate permafrost on the North Slope of Alaska. Since NMR is sensitive to the pore-scale distribution of liquid water, the distribution of ice within the pores can be determined. Comparison between core measurements and well logs demonstrated that the unfrozen water content of frozen sediments can be predicted from borehole NMR measurements. Interesting results applicable for this thesis is how the T2 distribution developed as the sandstone samples were melting, shown in Figure 3-1 [9]. A similar development will be presented in the results of the high-pressure hydrate study, as hydrate forms and dissociate in the porous media.

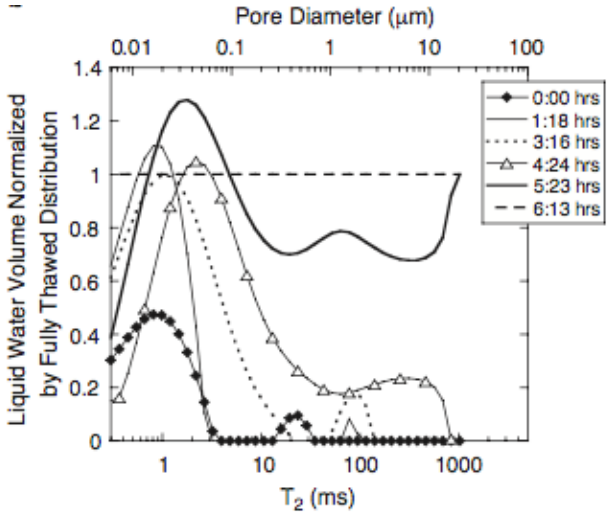

Figure 3-1: Relaxation time distributions of sandstone during thawing. Frozen samples are characterized by low signal amplitudes, and short relaxation times. As the sample is melting, the amount of NMR-visible (liquid) water is increasing. At the outermost line (6.25 hrs), all permafrost is melted, which reveals the pore size distribution of the sediments. Each T2 distribution has here been normalized by the T2 distribution of completely melted sample [9].

The shape of the T2 distribution profiles for water saturated sandstone cores are also of interest for this thesis. Relevant studies have been conducted by amongst others Petrov et al. (2010) and Vashaee et al. (2017) [42, 51]. One example from each of these studies are presented in Figure 3-2. Petrov et al. studied a water saturated Berea sandstone, by both CPMG-prepared SPRITE and SE-SPI measurements. Whereas, Vashaee et al. studied a brine saturated Bentheimer sandstone by CPMG measurements. Both of the T2 distribution maps were found to have one main peak, with more or less contribution in a second lower plateau. In other words, the T2 distributions of these water saturated sandstones were almost unimodal.

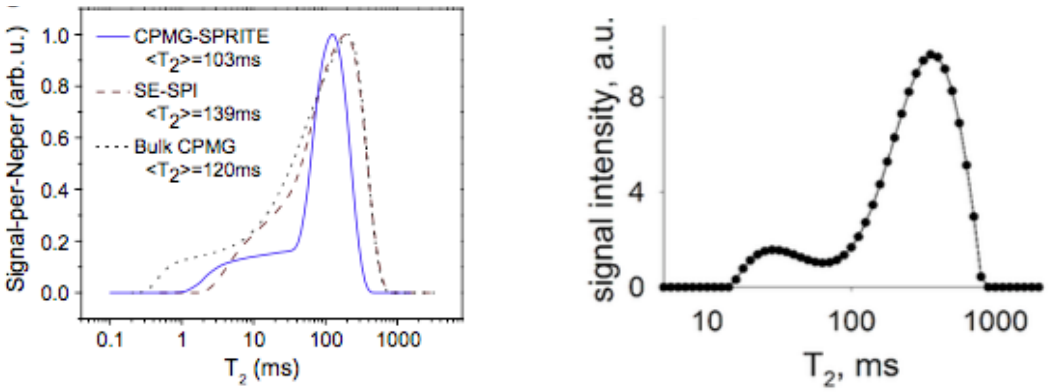

Figure 3-2: Left: T2 distribution map of a water saturated Berea sandstone core from studies by Petrov et al. (2010). Right: T2 distribution map of a brine saturated Bentheimer sandstone core from studies by Vashaee et al. (2017).

PART II. EXPERIMENTAL PROCEDURE AND METHODS

4 LABORATORY AND SCIENTIFIC APPROACH

In this part, two different studies will be described. The first study correlates water saturation of a sandstone core, with the signal intensity of the MRI measurements. The second, is a study of methane-propane hydrate, (in a high-pressure environment in a porous media), and how MRI can be used to visualize the gas hydrate phase transitions: formation and dissociation.

The chapters in this part, will follow these main steps, illustrated by Figure 4.1:

(1) **Experimental preparations**: Prepare the cores to the desired state, either at different water saturations, or at the right pressure for hydrate formation/dissociation.
(2) **Run experiments and MRI scans**: Measure the different states or change of state, of these core samples.
(3) **Gather and analyze the data using different programs such as MATLAB and Excel**

Figure 4-1: Pictures from the MRI laboratory. 1. The room where the pumps are located and where the high-pressure cell is prepared. 2. The room of the MRI instrument. 3. The computer with software to run the machine, and where the data is gathered.

5 EXPERIMENTAL PREPARATIONS AND SET-UP

5.1 MATERIALS

Three Bentheim sandstone cores with diameters of 1.5" and length of approximately 10 cm were used. Two of the cores were used in the saturation study, called SS2 and SS3. The third core was used in the high-pressure hydrate study, and was called HPH2. They were all saturated with water of salinity 0.1 weight% NaCl. (More details about the cores can be found in APPENDIX B). Saturation states of the different cores are displayed in Table 5.1**.**

The gas mixture used in the High-Pressure Hydrate Study consisted of 22% Propane in Methane. Fluorinert (FC-40) was used as confining fluid. Fluorinert is a fluorocarbon-based liquid and contain no hydrogen atoms, thus is not detected by the MRI. In addition, the low dielectric properties minimize RF losses [49].

Table 5.1: The different cores and their saturation states

Sample name	Water saturation (0.1wt% NaCl)	Gas added
SS2	Increasing	Non
SS3	Decreasing	Non
HPH2	65 % (initial)	22 % Propane/78% Methane

5.2 THE SATURATION STUDY

The Saturation Study had two different cores, called SS2 and SS3. SS2 was prepared with increasing water saturation for each measurement, while SS3 was prepared by desaturation; decreasing the water saturation for each measurement. The experimental steps are presented in Table 5.2**.**

Table 5.2: Water saturation steps

Step	Sw(SS2) [± 1%]	Sw(SS3) [± 1%]
1	36 %	96 %
2	58 %	86 %
3	67 %	73 %
4	81 %	66 %
5	96 %	57 %
6	-	44 %
7	-	34 %

Different methods were used to reach the desired saturation states. Saturations are estimated from mass balance. Porosity is estimated using grain density. Uncertainties are based on mass measurements.

5.2.1 Saturation methods

Increasing saturation steps (SS2)

1. The core was submerged in water, for approximately 10 seconds. Imbibition happened fast.
2. The core was fully submerged for a short time.
3. The core was submerged and stored in water for about 24 hours. (Assuming spontaneous imbibition is completed).
4. After the spontaneous imbibition was reached, the core was mounted in a core holder, and water was pumped in to increase the saturation. Outlet was closed for some periods to build up pressure, then open, and repeated.
5. The core was mounted in the core holder and water was pumped in.

Decreasing saturation steps (SS3)

1. To get as high as possible water saturation, the core was vacuumed before fully submerged in water.
2. To reduce the water saturation, the core samples was wrapped in paper and vacuumed for seconds to minutes, which causes water to escape from the core.
3. Vacuumed, wrapped in paper.
4. Vacuumed, wrapped in paper
5. To further reduce the saturation, the core was mounted in a core holder, and air is flushed through to desaturate.
6. Flushed with air, mounted in core holder.
7. Flushed with air, mounted in core holder.

The cores were wrapped in plastic film before they were placed in the MR scanner. A mark on the cores together with a tracer of silicone (visible in the MR image), was used to hold the placement and orientation of the core as identical as possible through the experiments.

5.3 THE HIGH-PRESSURE HYDRATE STUDY

By comparison to normal core analysis, the presence of the magnet with MRI, require special consideration to the equipment used. In other words, the equipment used must have minimal magnetic properties.

5.3.1 Core Preparation

The clean sandstone core was placed and stored in water, with assumption that spontaneous imbibition would give a desired saturation. It was desired to examine a large as possible volume, but because of sleeve limitations and volume limitations, both from the core holder and the examination room in the MR scanner, this study was done with the 1,5” core of approximate 10 cm length.

5.3.2 Choice of sleeve

Both shrink sleeve and nitrile rubber (Buna-N) sleeve were tested. Because the shrink sleeve leaked and was difficult to put on without breaking when heated, the rubber sleeve was the one chosen for this experiment. Picture of both under.

When the shrink sleeve was heated, it made water evaporate, thus making the water saturation more uncertain. In contrast to the thicker rubber sleeve, a shrink sleeve could give room for confinement fluid if a 2,5" core was used. Images below.

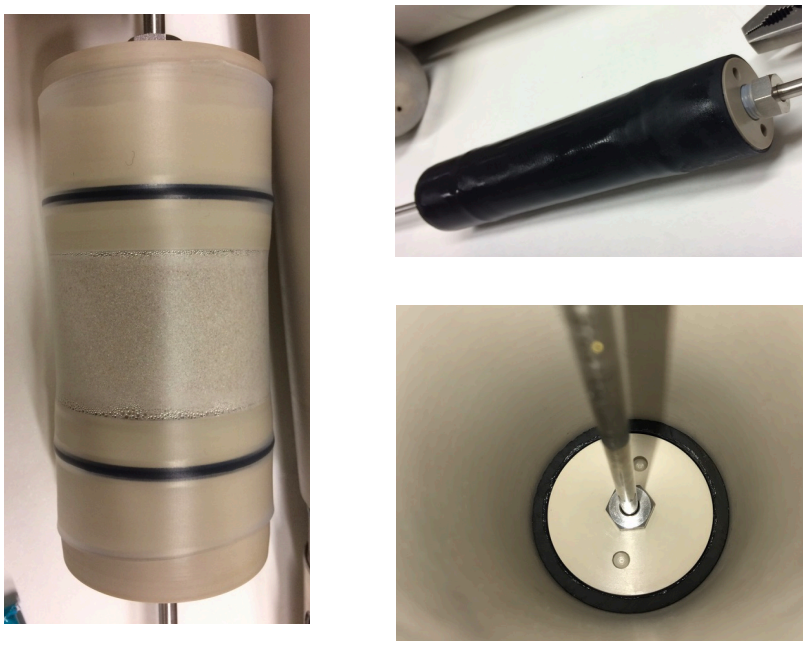

Figure 5-1: Left, picture of a 2,5" core inside a shrink sleeve, end-pieces mounted. Notice the accumulation of water droplets. Right top, 1,5"/10cm-core inside a rubber sleeve, end-pieces also mounted. Right bottom, no room for confinement fluid for a thick rubber sleeve around a 2,5" core.

5.3.3 The Core Holder

Schematics of the core holder, and an image showing the core holder ready to be assembled are presented in the following figures:

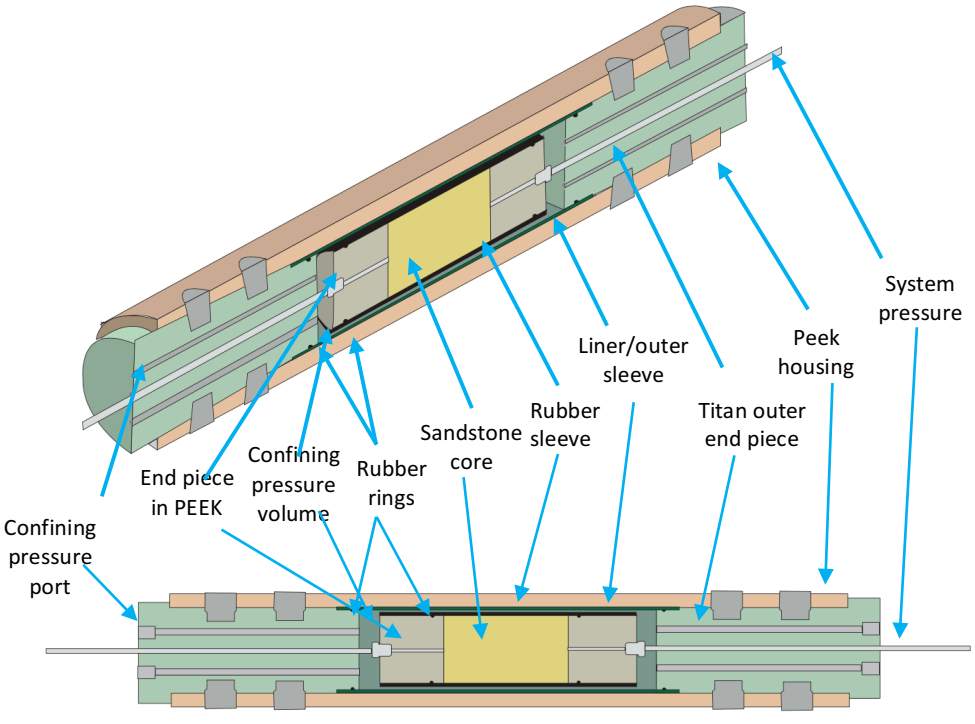

Figure 5-2: Schematics of the core holder.

Figure 5-3: Picture of disassembled core holder. The core is mounted in the rubber sleeve and ready to use.

5.3.4 Experimental Set-up and Procedure

This section is divided in preparations *outside* and *inside* of the MRI examination room. Schematics of the experimental set-ups are presented in Figure 5-4 and Figure 5-5.

Preparations outside of the MRI

The system was prepared outside of the MRI room; the cell was mounted, and pressures built up to 40/60 bar pore-pressure/confinement pressure. The system was pressure tested before it was moved inside the magnet. A more detailed description follows:

- The core was mounted in the core holder/high-pressure cell, se Figure 5-1 and Figure 5-2.

- The cell was placed vertically and Fluorinert was used as the confining fluid and pumped in from the bottom (in order to minimize air content). It was desirable to get the core back horizontally as fast as possible to minimize vertical segregation in the length direction.

- The pressures were then built up. First Fluorinert at 20bar. (It took time to stabilize). Gas was pumped in from both ends. The pressures were built up parallel, gradually, with a 20bar differential (confinement pressure desirable 20bar over pore/gas pressure). When the pressures were around 30-40bar and 50-60bar the pressures were set to constant pressure delivery. Pressure logs and pump volume logs was acquired to monitor potential leakages.

- When the system was closed, the cell was moved into the MRI. Valves were pre-mounted on the lines to make this an easy maneuver. See the stars in the figure.

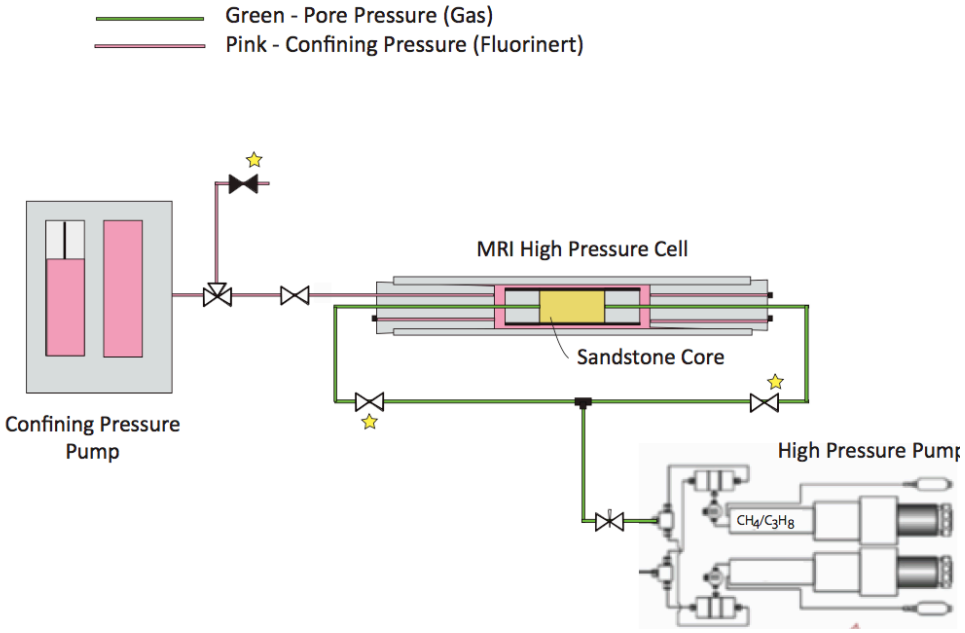

Figure 5-4: Schematics before the core holder is placed inside of the magnet

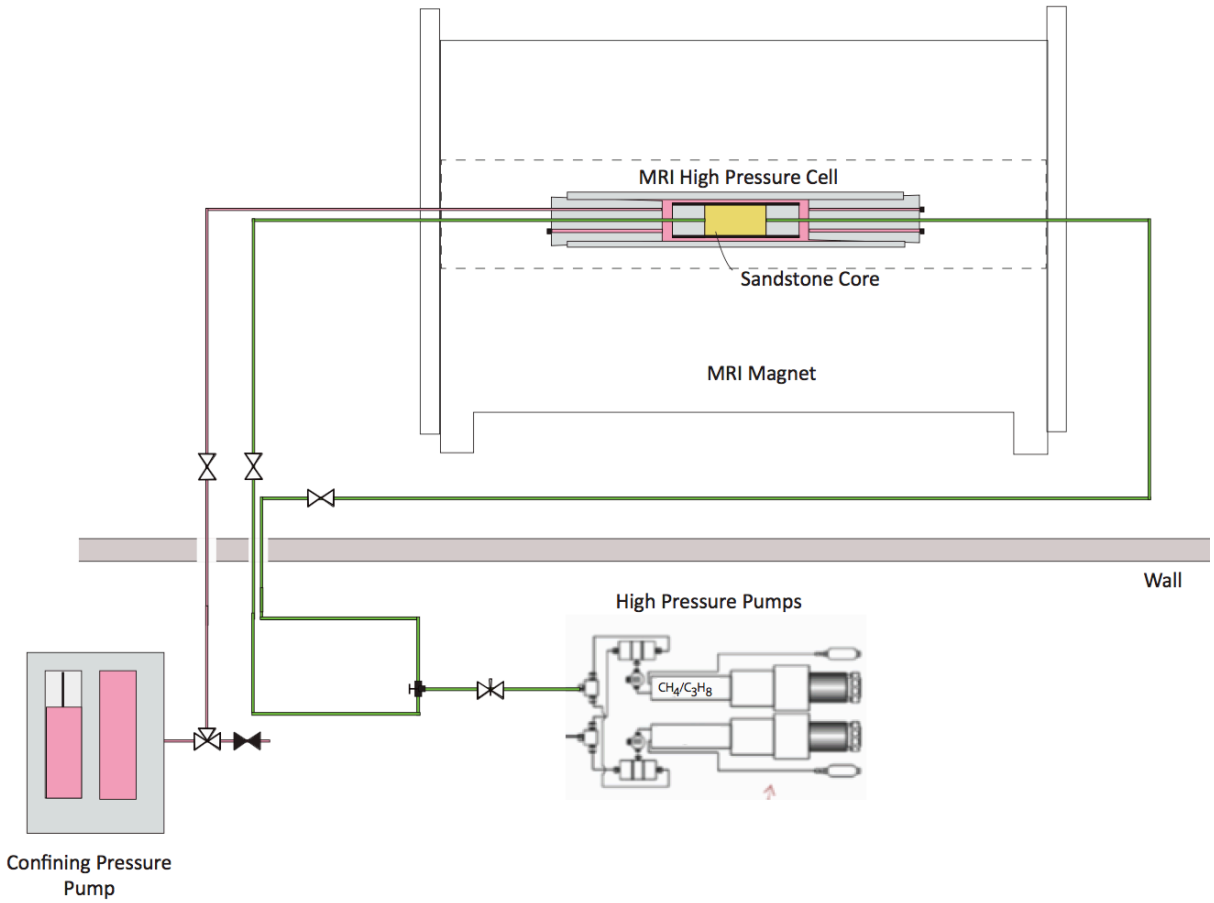

Figure 5-5: Schematics when the core holder is placed inside the magnet.

Inside of the MRI

The experimental steps with the core holder placed inside of the magnet are described in four sections, (1) Pressure build-up, (2) Hydrate stable pressure period, (3) Communication check, and (4) Depressurization. These four sections will be visible as separate steps in the results.

(1) PRESSURE BUILD-UP.

The lines were mounted, and the pressures built up before the valves were opened again. The system was left to stabilize before scan procedures (will be described in its own section) were started. The system was here at the blue spot in Figure 5-6. When the pressure built-up was continued, the pressures was gradually increased, until the pore pressure was inside of the hydrate stable zone (100 bar pore pressure), see red spot in Figure 5-6.

(2) HYDRATE STABLE PRESSURE PERIOD.

In this period, it was desired to have a constant pressure inside of the hydrate stable pressure region (at the red spot). In this experiment (HPH2) two errors occurred. The pump had to be filled with gas, and while the gas was filled, the valves to the system were not opened again. The scan procedure stopped right after this. This was discovered approximately 24 hours after. The valve was then re-opened, with a pressure drop of at least 3bar. Scans showed reduced water saturation, indicating hydrate formation. Scans were set on again, and the system left at same pressure condition as before (100/120bar), until the next day. Assuming gas was consumed in the hydrate formation, the pore-pressure was reduced some, green spot in Figure 5-6, just to illustrate a lower pressure.

(3) COMMUNICATION CHECK.

To check communication and potentially trigger hydrate formation a gas flush/pressure pulse was done (with expected reduced water saturation after, as water would be pushed out in the lines). One flush was done, and no communication was seen from the images. It was important that scans were started right after the flush to be able to observe any changes in the system.

(4) DEPRESSURIZATION.

The pore pressure was reduced by a rate of 0.5 mL/min. Confinement pressure was adjusted manually per 5bar. When the pore pressure reached 80 bar the system was set to be constant until the next day, the recording was also paused. The next day depressurization continued, but the confinement pressure pump malfunctioned. An error occurred in one of the pump cylinders, and the experiment had to continue by only using the other one. Pressure reduction was therefore continued until 20bar pore pressure was reached, and then held constant until the next day. The next day the pressure was further reduced until atmospheric conditions was reached.

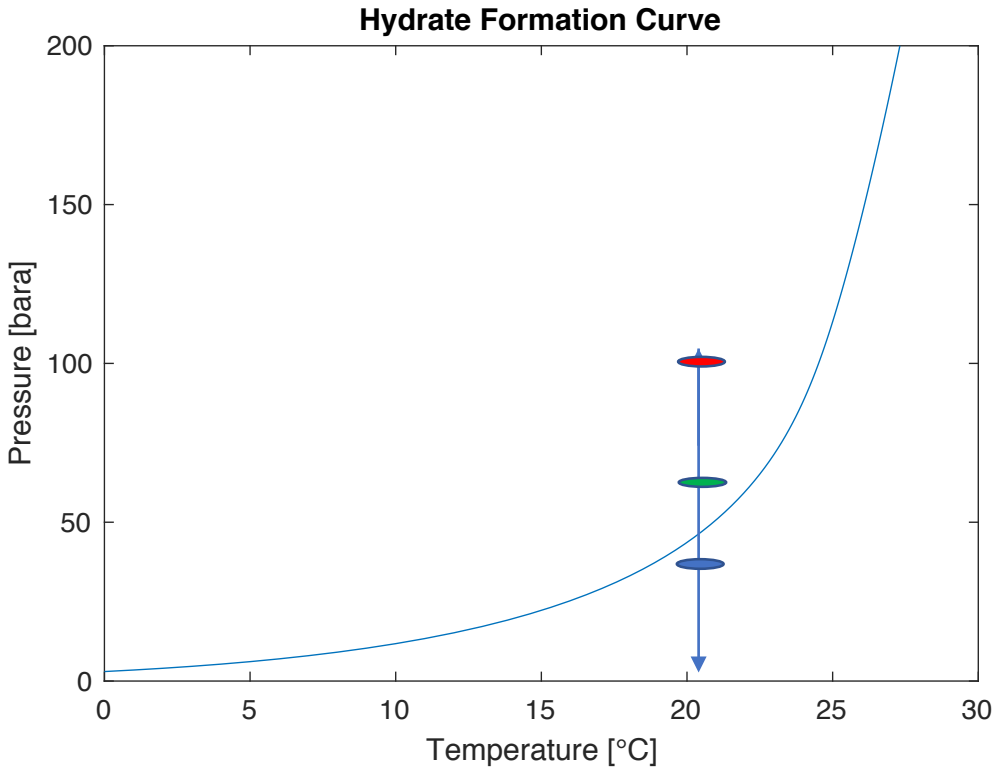

Figure 5-6: The hydrate equilibrium curve for this system. The arrow indicates the pressure regime, at 21°C. Blue spot: pressure when the cell is moved inside the magnet. Red spot: Desirable constant pressure, inside of the hydrate stability zone. Green spot: Pressure fall when hydrate formation consumes gas, without gas delivery.

6 THE MR – SCANNER AND SCAN PROTOCOLS

6.1 THE MRI INSTRUMENT

The Biospec MRI instrument used in this thesis, have a superconductive magnet with field strength of 4.7 Tesla. First of all, because of this extreme power the MRI room can be a very dangerous place without strict precautions. Metal objects can act as projectiles if they are taken into the magnet room, which can result in serious damage to people as well as the expensive instrument. It is therefore both important and necessary to have both equipment and tools of non-magnetic/metallic materials (but also, not wear any metallic objects, in clothing, jewelry or any other pocket fill).

Behind the rooms in Figure 4-1, a room consisting of a cooling system is located. The superconducting magnet is cooled by liquid helium. The concept of a superconductive magnet requires a system of low temperature for minimal resistance in the wire. Also, helium needs to be held at a low temperature to stay liquid. If the system is heated for some reason, the wire will become more resistant and lose its current, in other words; lose its magnetization. In such a scenario, the helium gas will be evacuated safely through lines out of the building.

As mentioned in Part I, Hydrogen is the nucleus of interest in these studies.

6.1.1 Main components of the MRI instrument

The main components of the MRI instrument are described under and illustrated in Figure 6-1.

The main magnet

The primary job of the main magnet is to produce a net magnetization of the sample (see *Chapter 2-Fundamentals MRI* for more information about net magnetization). Manipulation of this magnetization produces the signal in an MRI experiment. The magnetic field should be independent of time, and very homogeneous [40].

Gradient field

The second type of coils in MRI are linear magnetic field gradients. Their purpose is to spatially encode the positions of the spins by varying the value of the local magnetic field. As a result, the Larmor frequencies of the spins will vary as a function of their positions. The fact that these coils can rapidly switch during scans, allows collection of large regions of k-space in a short amount of time [40]. Gradient coils have three sets of wires, creating magnetic fields in x-, y-, and z- directions [52].

RF(Radiofrequency) coils

There are two types of RF coils in the instrument, which are named after their purposes: *The transmit coils* excite the magnetization, while *the receive coils* receive the signal from the excited spins. In contrast to the gradient and the main magnet systems, RF coils produce and detect time dependent fields [40].

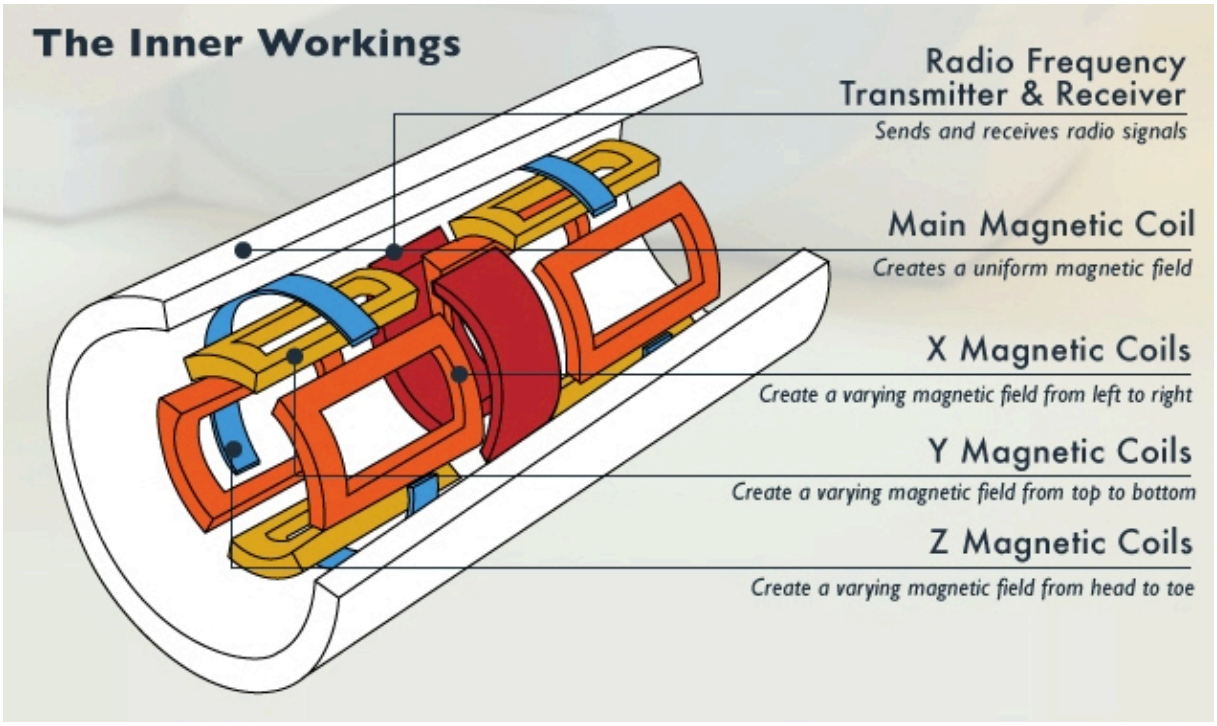

Figure 6-1: Illustration of the main components of the MRI instrument [53].

6.1.2 ParaVision®

ParaVision® is the imaging software that comes with Bruker's MRI package. Its functions include multi-dimensional MRI data acquisition, reconstruction, analysis, visualization, and data archiving [54, 55]. The software requires a computer with the Linux operating system.

It is from this software the scan protocols are found, adjusted and run. Data are both gathered manually, and from automatic generated files. (This will be discussed in Chapter 7).

6.2 SCAN PROTOCOLS/PULSE SEQUENCES

To get the information desired from a MRI scan, there has been developed a large number techniques containing different pulse sequences. Different sequences are constructed and run to get the desired information about the nucleus studied. The different settings of these sequences will have an impact on the results. For example, it requires a low echo time to detect signal from water in a porous media.

Besides suitable settings for the sample examined, it is also important that the magnetic field is as homogeneous as possible before the MR experiment is started, this can be done by *shimming*. During shimming the electric currents in the coils are adjusted, so that the resulting small magnetic field gradients cancel the residual in-homogeneity of the main field as completely as possible. The disturbances of the field are mainly from inhomogeneous distribution of magnetic objects within the surroundings, like steel armor in the walls, floor and roof, but can also be a result of the sample itself.

Also, before the MR experiment is started, a set of three plane, low resolution, large field of view *localizers* are obtained. These will be used as a guidance when choosing the field of view (FOV) and slice selection in the main scans.

For the purpose of this thesis, three different scan methods will be described, all based on the CPMG (spin echo) sequence:

- CPMG (basic form)
- MSME
- RARE

CPMG and MSME are in this thesis used to measure T2. CPMG was used in the High-Pressure Hydrate-study, while MSME was used in the Saturation-study. RARE was used in imaging and pixel intensity analysis for both studies.

6.2.1 CPMG (basic form)

As mentioned, CPMG is a spin echo sequence. It consists of one 90° pulse followed by multiple 180° pulses. CPMG was used for the High-Pressure Hydrate Experiment, and Table 6.1. displays some of the relevant settings used.

Table 6.1: Some settings used for CPMG, in the High-Pressure Hydrate Study

Echo spacing	5.00000 ms
Repetition time	4004.70 ms
Number of echoes	400
Number of averages	20
Scan time	1m20s93ms

6.2.2 MSME

MSME, (Multi Slice Multi Echo), is a CPMG sequence with slice selective RF pulses, which generates multiple spin echoes. This sequence makes it possible to investigate different slices/locations in one scan, in contrast to a single CPMG which measure the whole sample in one. MSME was used for the Saturation Study, and Table 6.2 displays some of the relevant settings used.

Table 6.2: Settings used for MSME, in the Saturation Studies

ROUTINE	
Echo Time	5.16029 ms
Repetition time	3442.61 ms
Number of echo images	50
Number of averages	2
Scan time	5m37s375ms
GEOMETRY	
Number of slices	12
Slice Orientation	Axial
Slice Thickness	3.00000 mm
FOV	51.0000 mm x 49.0000 mm
Slice gap mode	Non contigous

In addition to the standard MSME settings used for all the saturation stages, there was done some scan experiments with different settings, to look at how the results would vary, some of these was analyzed, and can be found in APPENDIX G.

Slice selection

Using a cylindrical core, the slices have to contain the same volume (at the same location) for comparison reasons. The slices' orientation was set to *axial* (since the core lies parallel with the magnet), which gave pictures with the same volume of circular pieces of the core. An example displaying the slices of SS3 at 73% water saturation is found in Figure 6-2.

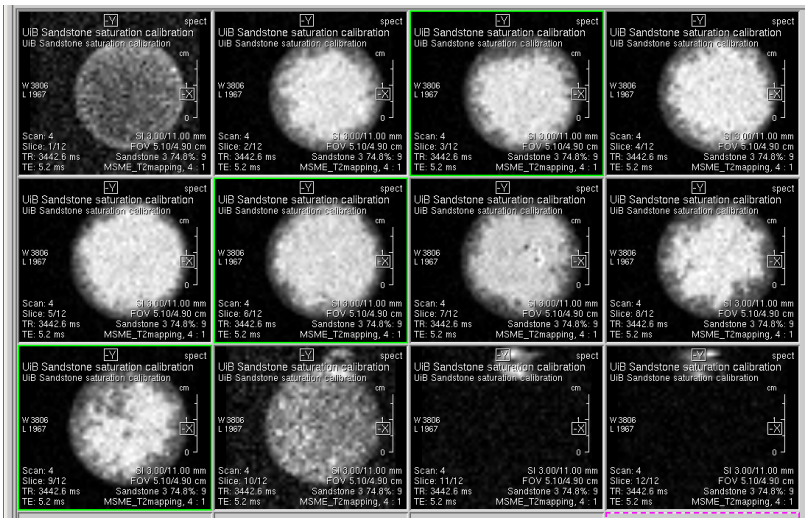

Figure 6-2: Image of the slices from SS3, at Sw = 73%. Using axial slices, the volumes representing the core will be the same. (Higher uncertainty with the two core slices at the ends).

6.2.3 RARE

RARE (Rapid Acquisition with Relaxation Enhancement), is in contrast to the two methods described above, used here to make images, for further analysis. The images consist of pixels with relative intensities, the values are assumed to be proportional to amount of (liquid) hydrogen. The technique uses multiple spin echoes (CPMG), together with selective RF pulses, as for MSME.

RARE factor

The number of 180° pulses (refocusing pulses) are called RARE factor. The echoes generated by the following 180° pulses will be smaller and smaller until it fades away, if not a new 90° pulse (excitation pulse) is added in between, see Figure 6-3.

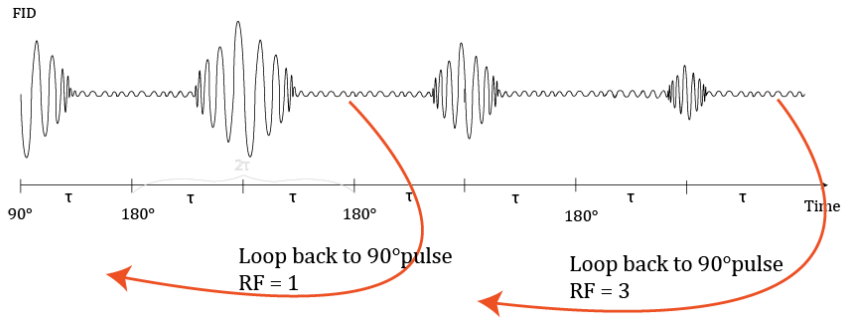

Figure 6-3: Illustration of an echo train and rare-factor.

Each spin echo gives one line in k-space. The contrast fades the longer it is from the 90° pulse, and will after a time completely fade away. The rare factor must be a balance between time saved and how much contrast quality that can be sacrificed.

A more detailed description of a RARE pulse sequence is found in Figure 6-4**.** The difference from MSME, is that MSME increments the phase gradient on every scan rather than every echo [8]. The RARE sequence used in this thesis is of the RAREst (Rapid Acquisition with Relaxation Enhancement with short echo time) variant. The technique is programmed to attain the shortest possible echo time and spacing. Some relevant settings of the RARE measurements are listed in Table 6.3.

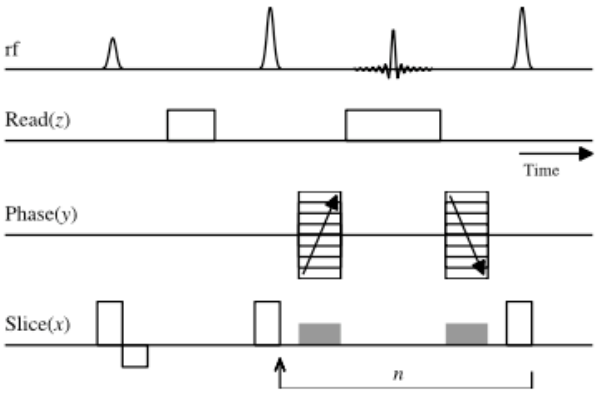

Figure 6-4: Schematics of a RARE pulse sequence. RF pulses: small top represents a 90° pulse, while the tall top represents a 180° pulse. An echo is illustrated between the two refocusing pulses. A series of *n* spin echoes are acquired, where *n* is the RARE factor. The phase gradient is incremented on each echo, while slice select gradients are applied to coincide with each 90° pulse. [8]

Table 6.3: Some settings used for RARE, in the High-Pressure Hydrate Study (HPH2) and in the Saturation Studies (SS2 & SS3) (* specified in chapter 7.1.3)

ROUTINE	HPH2	SS2 & SS3
Echo Time [ms]	4.80914	9.61828
Repetition time [ms]	3500.00	1395.75
Number of averages	5	40
Number of repetitions	1	3 or 1*
Scan time	7m0s0ms	41m52s350ms
RARE factor	2	4
GEOMETRY		
Number of slices	56	43
Slice Orientation	Axial	Axial
Slice Thickness [mm]	2.00000	3.00000
Number of pixels	47 x 49	60 x 60
FOV [mm^2]	47.0000 x 49.0000	60.0000 x 60.0000
Slice gap mode	Contigous	Contigous
PULSES		
Excitation pulse [°]	90.0000	90.0000
Refocusing pulse [°]	105.489	120.000

7 DATA ANALYSIS

Before the analysis could start, the data had to be extracted. The different scan methods resulted in different information, and thus need different processing. First is general information about RARE, the files used, and some specifics about the different studies presented. Thereafter MSME and CPMG will be described, which both was used to generate T2 distribution maps, described in its own section.

There is a lack of quantification when using fast medical MRI protocols, which has meant that these methods have lost favor in the core analysis community [8]. The following text will include some of the challenges met in this work. However, solutions to some of these should be possible to include in adapting a more user-friendly software for core analysis.

7.1 RARE

7.1.1 DICOM files

Results from the RARE studies, are exported to DICOM files. DICOM, acronym for "digital imaging and communications in medicine", is the standard image file format used by radiological hardware devices. DICOM files store a large amount of data. Each file has two main parts. The first, "the header", contains amongst other items, acquisition parameters, operator identifiers and image dimensions. The other part contains the image data. They often contain multiple high-resolution images, which is why they tend to be large. DICOM files usually need to be viewed on dedicated workstations, but can also be transferred electronically to other DICOM viewing software [56]. For the purpose of this thesis, MATLAB has been used for analyzing DICOM files.

There was a lot of information gathered, and which needed to be systematized. From one study, the different scans come in different folders, containing one DICOM file per slice (times repetitions if added in settings). For example, the High-Pressure Study had 129 folders times 56 files in each.

Lesson learned: The folder name contains the scan number. When the study is set up, it can be practical to get the scan numbers in the right order of time, as the software does not do this automatically.

7.1.2 Data Analysis

MATLAB was used to analyze the DICOM files. The presentation of these data is divided in MR images, and pixel intensity analysis (part III – results and discussion). The first script used for both, reads and sorts the files in time, making a workspace for further analysis. The scripts used are found in APPENDIX D.

The MR images

RARE gave MR images of each slice. The slices for each time step or saturation step were put together in montages. The montages could then be compared, and used in spatial analysis of the development, either for saturations or in time. The 129 montages from the High-Pressure Hydrate Study were put together in a movie, visualizing the development in each slice through time.

Pixel Intensity Analysis

Three scripts were developed for the pixel intensity analysis. The first script read all the files in all the folders, for example for HPH2: 56 files in 129 folders. A lot of information can be gathered from the DICOM files. For this work, the pixel matrix of the MR image, the corresponding time, and placement in the core were of interest. Resulting in 4 dimensions of information, as the montage movie. The pixel matrix was therefore reduced to a value representing the condition of a certain slice of a certain time. This reduces one dimension of the image information: image matrix(x,y), through the core (z), through time (t), going to relative slice intensity (x), through the core (y) through time (t).

To sum up, the script makes (1) a matrix, where each number represents the sum of all the intensities for the corresponding slice at a certain scan, (2) time and length vectors to get the real dimensions (spatial and in time), and sorting the matrix in the right order.

7.1.3 The Saturation Study

Intensities were summarized for each slice in a matrix of "*slice number* x *increasing saturation steps*", and the workspace was saved.

The saturation folders, contains DICOM files for each slice, for each repetition. The first experiments were conducted using 3 repetitions, but because they showed no remarkable difference, this was skipped for the last two experiments. This resulted in difference in number of files in the folders (and a little complication when analyzing). Also, there are missing a saturation step in the SS3 study, because different settings were used.

A second script was developed to make figures. For practical reasons a cropping section was added. The three sets of repetitions were reduced to one, and the slices at the ends not containing the comparable volume of the core were removed. Water saturation vectors were defined for the two studies. Figures generated was both 2D and 3D illustrations of the development, and will be presented in the results.

7.1.4 The High-Pressure Hydrate Study

Intensities were summarized for each slice in a matrix of "*slice number* x *time*", and the workspace was saved for the further analysis. Results from the saturation study was presented as function of intensity, with known water saturation, illustrating the linear relationship between the two. The High-Pressure Hydrate Study uses this linear relationship to estimate water saturation from the measured intensity. Equations and theory used in the estimations are described in chapter 2.6. A similar script as for the saturation study was developed to crop and make figures, but here as a function of water saturation rather than intensity. The figures generated are presented in the results.

7.2 CPMG

7.2.1 Data Gathering – The Signal Decay Curve

Information from the CPMG study was extracted from folders of Unix Executable files (Linux system), which must be processed by MATLAB to get readable text files describing *the signal decay curve*.

Every time step through the HPH2 study was processed one by one (129), which makes this a very time-consuming procedure. It may be possible to modify the script to process all inside a folder automatically.

7.2.2 Decay Curve and Initial Intensity

Initial intensity of the decay curve was gathered from two methods. The decay curve values were loaded in MATLAB:

First method: Using *the curve fitting tool* in MATLAB to extrapolate the signal decay curve. But only an exponential decay function without the offset was possible (see *equation 2.4*):

$$f(t) = C \cdot e^{b \cdot t} \qquad (7.1)$$

Second method: Plotting the curves, and using the cursor in the decay plot directly. First point from first echo, in other words not at *t=0*, as a result the values will be smaller than the real initial intensity. This is actually the first intensity value, and could easily be gathered directly from the text file (without MATLAB).

7.3 MSME

7.3.1 Image Display and Processing – Slice Analysis

When the MSME study is opened in the "Image Display and Processing" tool in ParaVison, images from all the slices can be shown, Figure 7-1. From here the different slices was further processed, one by one. Since this data extraction method is time consuming, only tree slices were investigated for each saturation step, marked in green. The selected slices were consistent for all saturation steps. When comparing the different saturations, it was desirable to look at how the exact location/volume changed through time. Care was taken to hold the placement of the core as accurate as possible for each measurement.

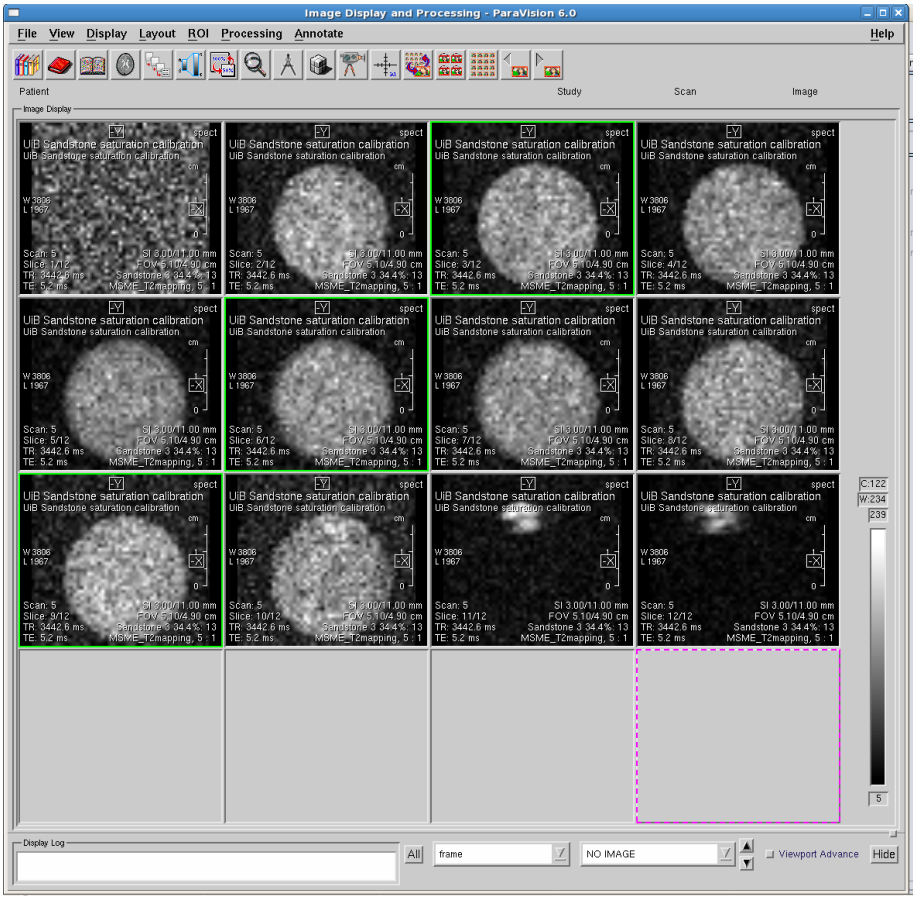

Figure 7-1: Screenshot of the slices in the MSME study. Opened in ParaVision: "Image Display and Processing". Slices marked in green frames are ones further investigated.

7.3.2 Image Sequence Analysis Tool & ROI

The selected slice was then open in the "Image and Sequence Analysis tool", where a ROI (Region of interest), can be defined. See circle and squares in Figure 7-2. Different standard shapes and sizes are available.

As is shown in the image, the saturation varied with the diameter, more water at the center of the core than toward the edge. Both a circular ROI of 9.57cm^2 and a square ROI at approximately 6.25 m^2 were defined for all the slices investigated, because the fraction of light and dark areas will vary some.

When a ROI was defined, the signal decay curve for this region could be extracted from the table in Figure 7-3. The table includes also estimated T2 relaxation time, and *initial signal intensity*. The text file generated are then exported to Excel. From Excel, the intensity and time values was extracted to separate text files.

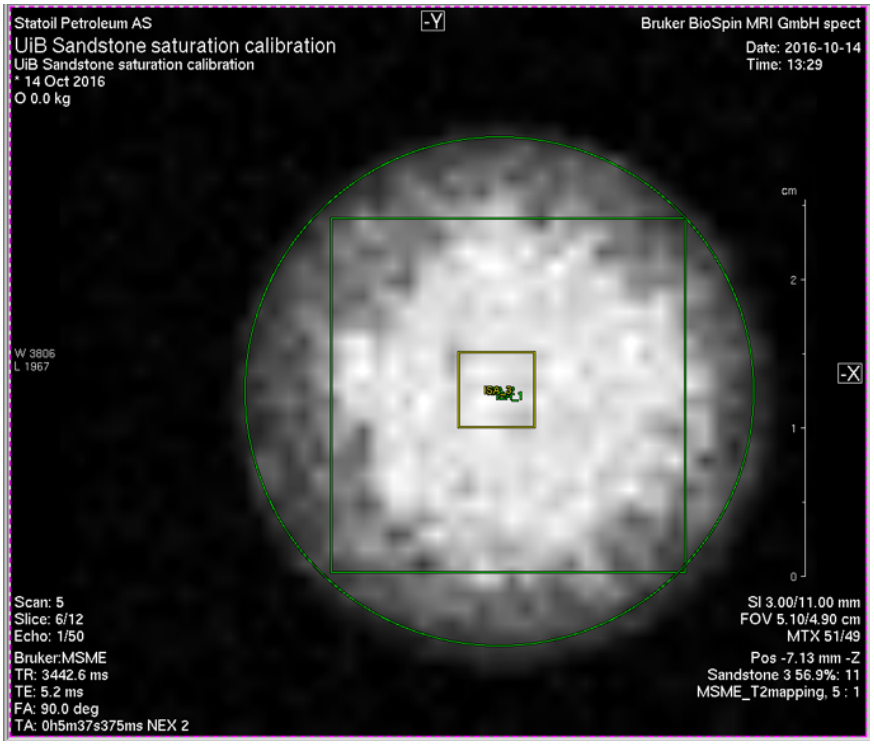

Figure 7-2: Screenshot of a slice in the Image Sequence Analysis Tool. Two square and one circular ROI are defined.

.

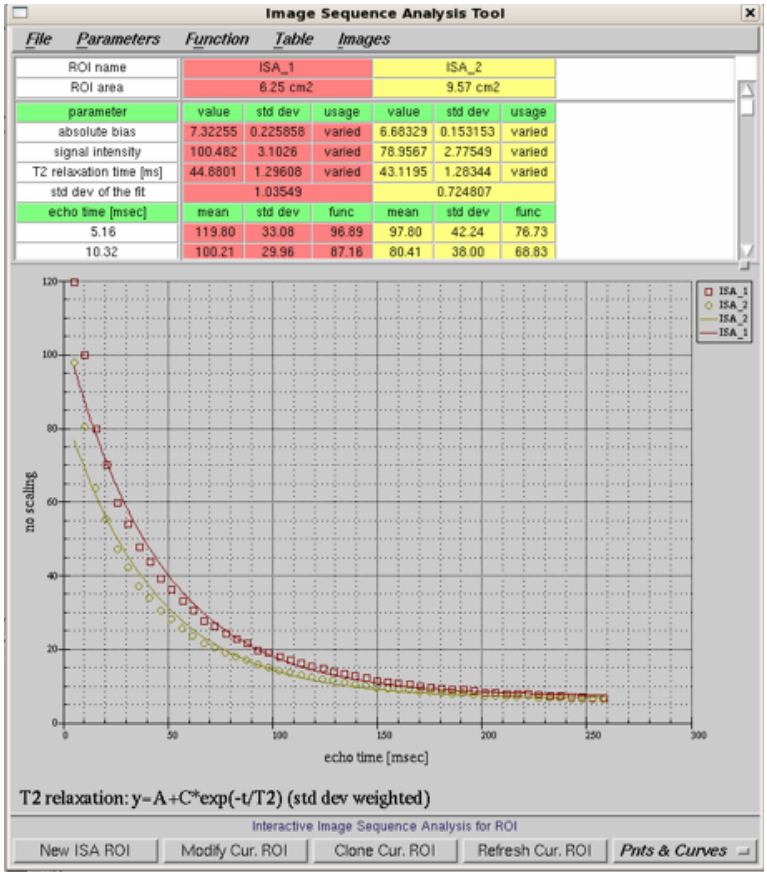

Figure 7-3: From the ROI chosen, (here ISA_1 and ISA_2), decay curves are generated, and values presented in the table above the curve.

7.4 T2 DISTRIBUTION MAPPING

2D Laplace inversion of the decay curves was calculated by a program in MATLAB. Here the two text files describing the signal decay curve were loaded, and with some manually adjustments in the program, new files (.out) were generated. Then these new files (.out) were loaded in another script plotting the T2 distribution maps. This procedure was also time-consuming, since it had to be done to every decay curve individually.

More information about the "2D Laplace Inversion"-program are found in the APPENDIX D. All the scripts used for CPMG and MSME, excluding the "2D Laplace Inversion"-program, are provided in APPENDIX D

In the MSME studies of SS3, the signal decay curve from both square and circular ROIs was generated. Illustrated in Figure 7-4, water saturation step S_w = 65%, from both square (x) and circular (o) ROI. (All the saturation steps are found in APPENDIX F). There was found a difference between the two ROIs. In the results only the circular ROIs are used, as they represent more of the heterogeneous saturated volume of the core.

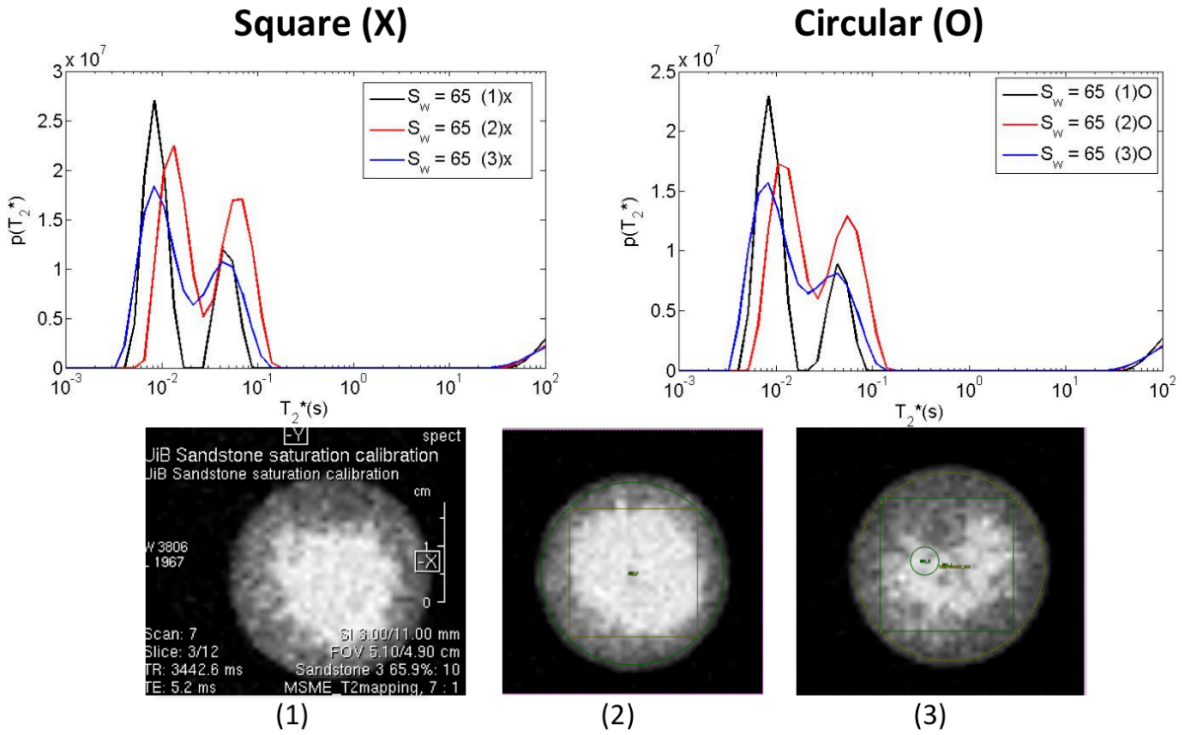

Figure 7-4: SS3 at 65% water saturation. Three slices of the core were selected. The figures on top show the different T2 distribution maps of the three slices, left for a square ROI, and right for a circular ROI.

PART III. RESULTS AND DISCUSSION

8 THE SATURATION STUDY

Before studying phase transitions to gas hydrate, a study correlating (liquid) water saturation and signal intensity was conducted. The signal intensity was found to be strongly dependent on water saturation, and they were found to have a linear relationship.

Two sandstone cores were used in the study: The one identified as SS3, started with high water saturation, which thereafter was desaturated for each measurement, the other one SS2, started with a low water saturation which thereafter was increased for each measurement. The increasing water saturations was found to give the most homogeneously distribution of water in the pores, when the core had saturations of 67% and less. The method used for the three first increasing water saturations reaching 67 %, were also the easiest conducted, by only submerging the core in water for an increasing time. However, the desaturating steps of SS3, were found to give a more homogenously distribution of high water saturations (approximately 96-81%). The method reaching the high saturation in the SS3 study, included vacuuming the core before fully submerging it in water. To summarize, the methods where the core was submerged in water either vacuumed or not, gave the most homogenous saturations, in contrast to methods where water or air were pumped/pushed through. The method of submerging the core in water, is recommended for later experiments on hydrates, or other experiments desiring a homogenous water saturation of approximately 55-70%. If a higher water saturation is desired with a homogenous distribution, it is recommended to vacuum the core before submerging it in water.

It can be comment that the first step of SS2, with the lowest water saturation of 36%, was found to have a relative even saturation in the length of the core, but indicate an uneven water saturation towards the center of the core.

The results from the two saturation studies are divided as follows: The first section looks at RARE results, first presented as images, thereafter a further analysis of the pixel values correlating intensity and water saturation are presented. The pixel analysis includes two-dimensional and three-dimensional maps, figures, and plots of the linear relationship between intensity and saturation. The second section looks at MSME results. First are the T2 distribution maps presented, thereafter an analysis of initial signal intensity.

8.1 RARE – MR IMAGES

To illustrate the development of water saturation through the core, the image slices for each saturation step were put together in montages, see Figure 8-1 and Figure 8-2. The hydrogens in the water molecule generates the signal. The brighter the pixel is, the higher signal intensity was detected, and the more water the representing location contains. Notice, the slices at the end of the core are often darker because they may contain a smaller volume of the core, (blue cross in the montages). In other words, the core is not necessarily less water saturated here. They are therefore not relevant for comparison. The small circle(s) in the last slice(s) is signal from the silicone tracer used for localization of the cores. The location of the cores is not identical for each measurement. The first slice the core is visible in, and the core volume it contains will therefore vary some.

Sample SS3, the one which was desaturated, are presented in montages of 42 images. The other one, SS2, are presented in montages of 36 images. The montages are presented in time wise order, SS3 in a decreasing order of saturation, whereas SS2 in an increasing order of saturation.

8.1.1 Montages of sample SS3 (desaturated core)

The core started as fairly even water saturated, see the first montage in Figure 8-1, but became more uneven through the reduction steps in the study, see the last montage in Figure 8-1. The reduction is most prominent in the ends and edges of the core. At the last step, with 57% water saturation, the core is left with an uneven saturation where the center in the middle of the core has the highest remaining saturation.

Main observations:
(1) Reduction of signal intensity with decreasing water saturation
(2) More reduced in the ends and edges of the core than in the middle and center.

8.1.2 Montages of sample SS2 (increased saturation)

The main trend development for SS2, was increasing signal intensity. In line with theory, as the core had an increasing water saturation. The first three water saturation stages, were found to have a more even water distribution through the length of the core than the two last ones, as will be visible in the following montage illustration, Figure 8-2.

The first step, with water saturation of 36% was found to be the most heterogeneously saturated in each slice. A circle is visible in most of the slices in the first montage, but disappears in the following montages. In other words, the first montage of 36% water saturation had the most signal variations towards the center of the slice. In the three following montages, with water saturations of 58, 67, and 81 %, a bright contour of the edge of the core is visible in some of the slices. This bright contour can indicate that there was an accumulation of water on the surface of the core at corresponding regions. Another reason for the bright contour may be a susceptibility artifact. The second last montage, with water saturation of 81%, illustrate an uneven saturation through the core. The ends of the core had more signal than the middle, indicating higher water saturation in the ends. This distribution disappears with higher water saturation in the last montage.

Main observations:
(1) Increased signal intensity with increased water saturation
(2) Most steps were fairly evenly saturated in the length of the core, except the montage of S_w = 81% where the ends contained more water than the middle.

Montages of sample SS3 (desaturation)

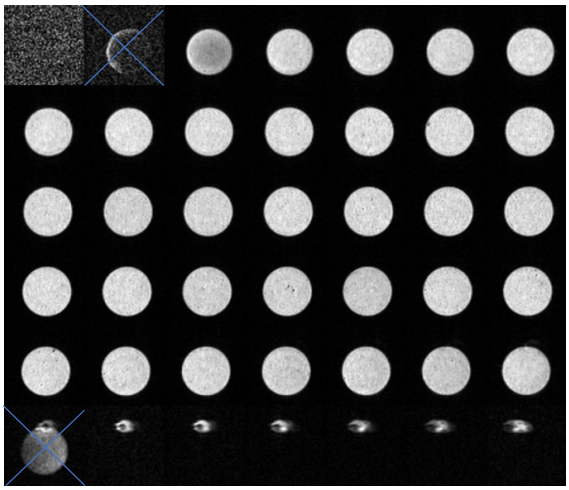

Sw = 96%
Initial water saturation. The slices were fairly evenly saturated with water.

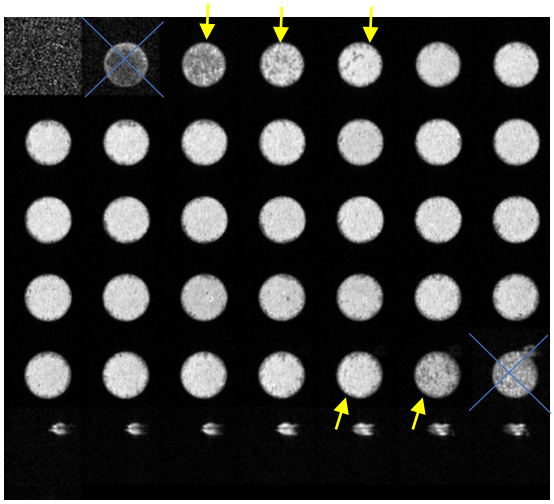

Sw = 86 %
Signal reduction was observed in the ends and edges of the core, see examples in yellow arrows.

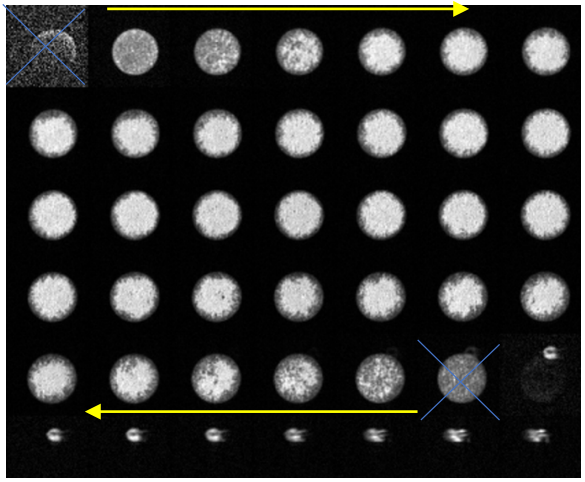

Sw = 73 %
More signal reduction was observed in the ends and edges of the core. Yellow arrows illustrate the development.

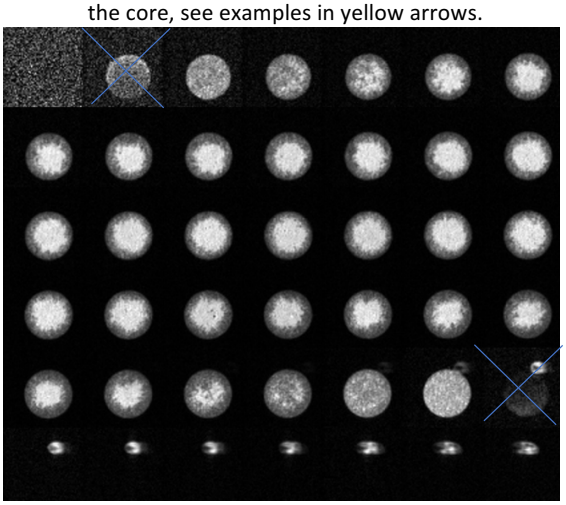

Sw = 66 %
Even more signal reduction was observed in the ends and edges of the core.

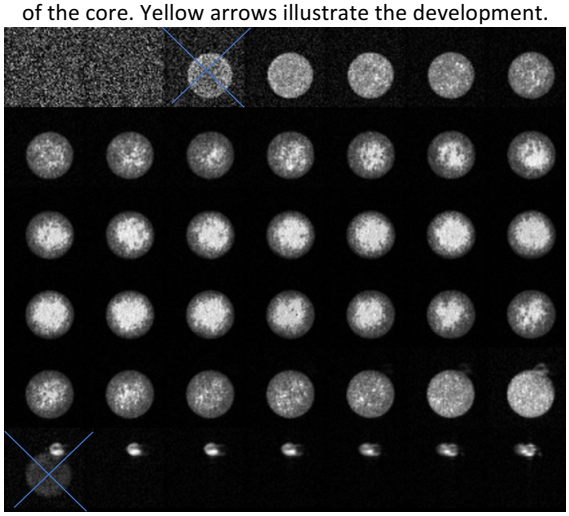

Sw = 57 %
Most of the signal were found in the middle and in the center of the core. In other words, the highest remaining water saturation was in the middle and in the center of the core.

Figure 8-1: Montages of the MR images of the slices of SS3, in decreasing order of saturation. The main trend of the development was less water in the end and edges of the core as the core was desaturated. Each montage contains all the slices of the core, (in addition to some of the surroundings). The first and last image of the core are not representative in comparison to the rest, illustrated by the blue cross.

Montages of sample SS2 (increased saturation)

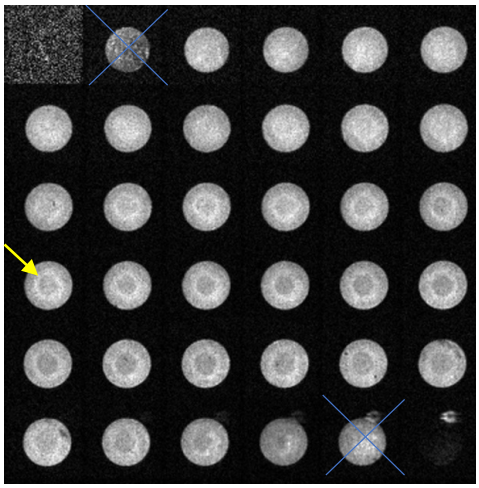

Sw= 36 %. Initial water saturation. The core was heterogeneous saturated towards the center of the slices. Yellow arrow points out an example of a slice with a visible circle.

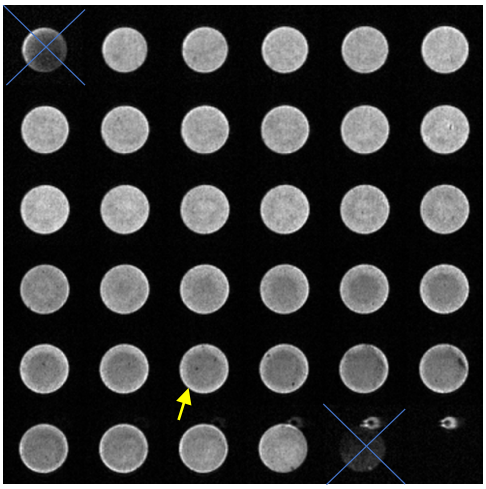

Sw = 58 %. A jump in water saturation make the core look more homogeneous saturated. The upper rows had a little more signal than the lower ones. The lower rows were characterized by a brighter contour in the edges, ex: the yellow arrow.

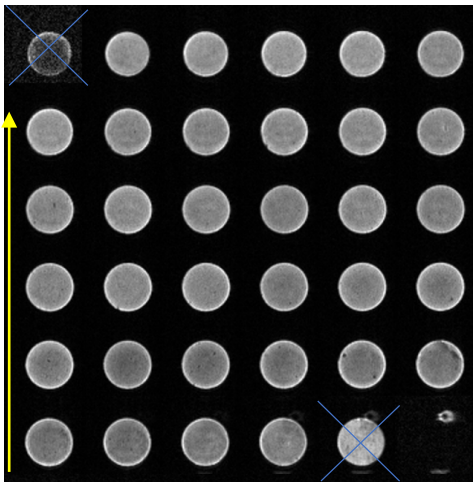

Sw = 67 %. Less variation through the core was found here. The bright contour in the edges were here seen in even more slices than before, developing from one end (yellow arrow).

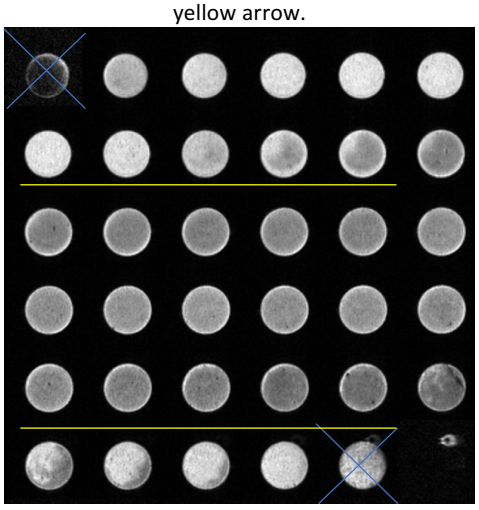

Sw = 81 %. More signal was found in the ends of the core length. Illustrated by the yellow lines. Bright contours were still visible in the slices in the middle.

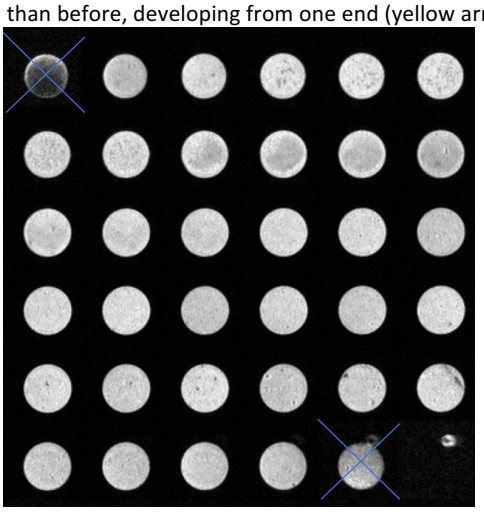

Sw = 96 %. This stage was found to be more homogeneous saturated than previous montage.

Figure 8-2: Montages of the MR images of the slices of SS2, in increasing order of saturation. The main trend development was increased saturation with increased signal intensity. Most steps were found to be fairly evenly saturated, except at Sw = 81%, where the ends of the core contained more signal than the middle. Each montage contains all the slices of the core, (in addition to some of the surroundings). The first and last image of the core are not representative in comparison to the rest, illustrated by the blue cross.

8.2 RARE – PIXEL INTENSITY ANALYSIS

8.2.1 Intensity Maps

Pixel intensities were summed for every slice, which made it possible to make a matrix with dimensions: *slice number* times *saturation*. From these matrices, intensity maps of the different saturations were created, and where slice number was used as length of the core. One flat two-dimensional map and one three-dimensional map, where intensity was lifted as its own axis, were created for both core samples, see Figure 8-3 and Figure 8-4. In the intensity maps, the saturation steps are presented in increasing order, in contrast to the MR images presented in time wise order. Only the slices that contained the core were included in the figures.

The colors in the maps illustrate signal intensity, and a color bar is added in the figures to illustrate the scale. Yellow indicates high signal intensity whereas blue indicates little signal intensity. The relative scale of the colors is more visible in the three-dimensional figures, but the two-dimensional makes it easier to look at the whole sample.

Since the intensity maps were built on the MR images, the same main observations as described in chapter 8.1.1 & 8.1.2 were found. The intensity maps made the variation of signal intensity through the length of the core easier to identify, giving a more detailed scale with clearer contrasts.

8.2.2 Intensity maps of sample SS3 (desaturated core)

Main observations from the image montages of SS3 were decreasing signal with desaturation, and an uneven reduction profile through the core. The reduction was most prominent in the ends and edges. The intensity maps illustrate the same development. The two-dimensional map has a brighter region with more signal in the middle of the length, which becomes larger and brighter as the water saturation increases. The three-dimensional map visualizes the saturation profiles through the length by a fold. The fold has a slope following the increased saturation. The shape of the development indicates the same; the core is generally higher saturated in the middle.

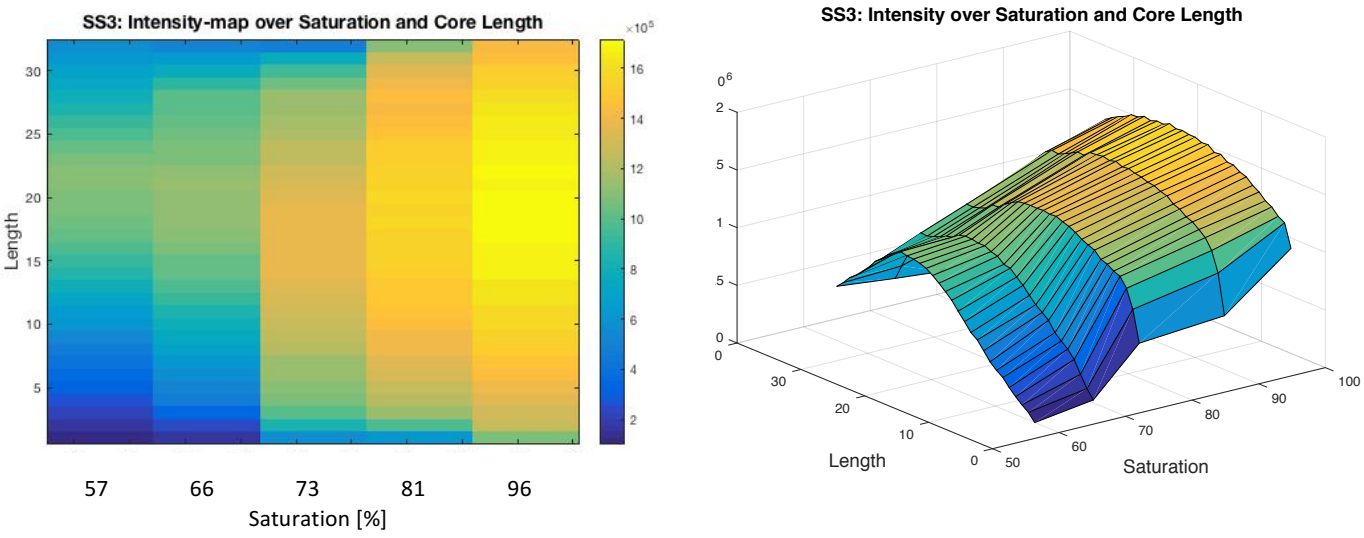

Figure 8-3: Intensity maps of SS3. Left, intensity map over saturation and core length, color-bar shows intensity scale. Right, 3D illustration of the intensity map, where intensity is added as its own axis. Saturation in %.

8.2.3 Intensity maps of sample SS2 (increased saturation)

Main observations from the image montage of SS2 were increased signal with increased water saturation, most of the steps were fairly evenly saturated, except at S_w = 81%, where the ends contained more signal than the middle. The intensity maps illustrate the same development, but give more detailed profiles of through the core. Especially the profiles of the two highest saturations give more information: At S_w = 81 % the profile was, as observed in the montage, highest in the ends. At S_w = 96% the profiles in the intensity maps illustrate a higher intensity in the middle of the core, and a reduction in the ends compared to the previous stage.

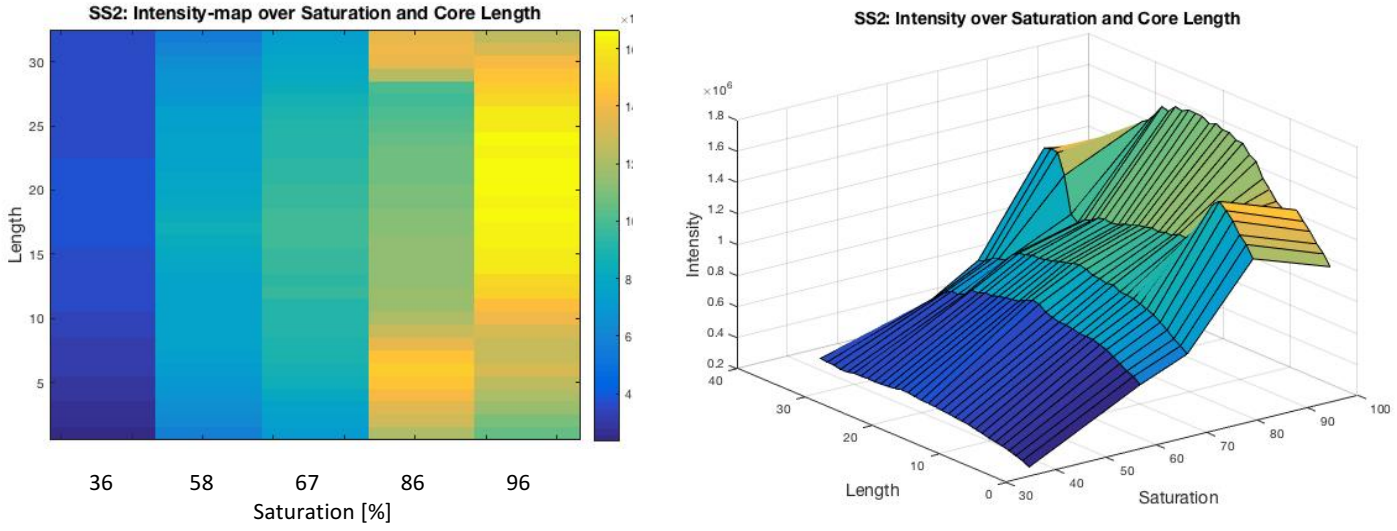

Figure 8-4: Intensity maps of SS2. Left, intensity map over saturation and core length, color-bar shows intensity scale. Right, 3D illustration of the intensity map, where intensity is added on its own axis. Saturation in %.

8.2.4 Intensity profiles per saturation

In addition to the intensity maps, figures of the intensity profiles through the length of the core for each saturation step were made, see Figure 8-5. In this case, it is the saturation axis which are excluded.

The intensity profiles for SS3, illustrate the same development through the desaturation, but makes is easier to analyze the development in the length of the core. The profiles for the higher saturations were more even over the length, but a little less signal from the ends of the core. As the saturation was reduced, the profiles of the ends became steeper. At the lowest saturations, the profiles have a steep peak towards the middle of the core. The development illustrates that saturation reduction was highest in the ends, also desaturation resulted in higher saturation variety through the core.

As for the profiles of SS3, the first saturation stages of SS2 gave the most even profiles through the core. These were reached by spontaneous imbibition, as the first profile of SS3. The profile of S_w= 81% illustrate increased water saturation in the ends of the core. This saturation was reached by pumping water through the core from the ends, which can explain the shape of the profile.

Comparing the two profiles at Sw = 96% for both samples, two different shapes were found. The one reached by (vacuuming and) spontaneous imbibition (SS3) was found to be more even through the

core. The other one reached by pumping water in (SS2), left a top in the middle and higher variety through the core.

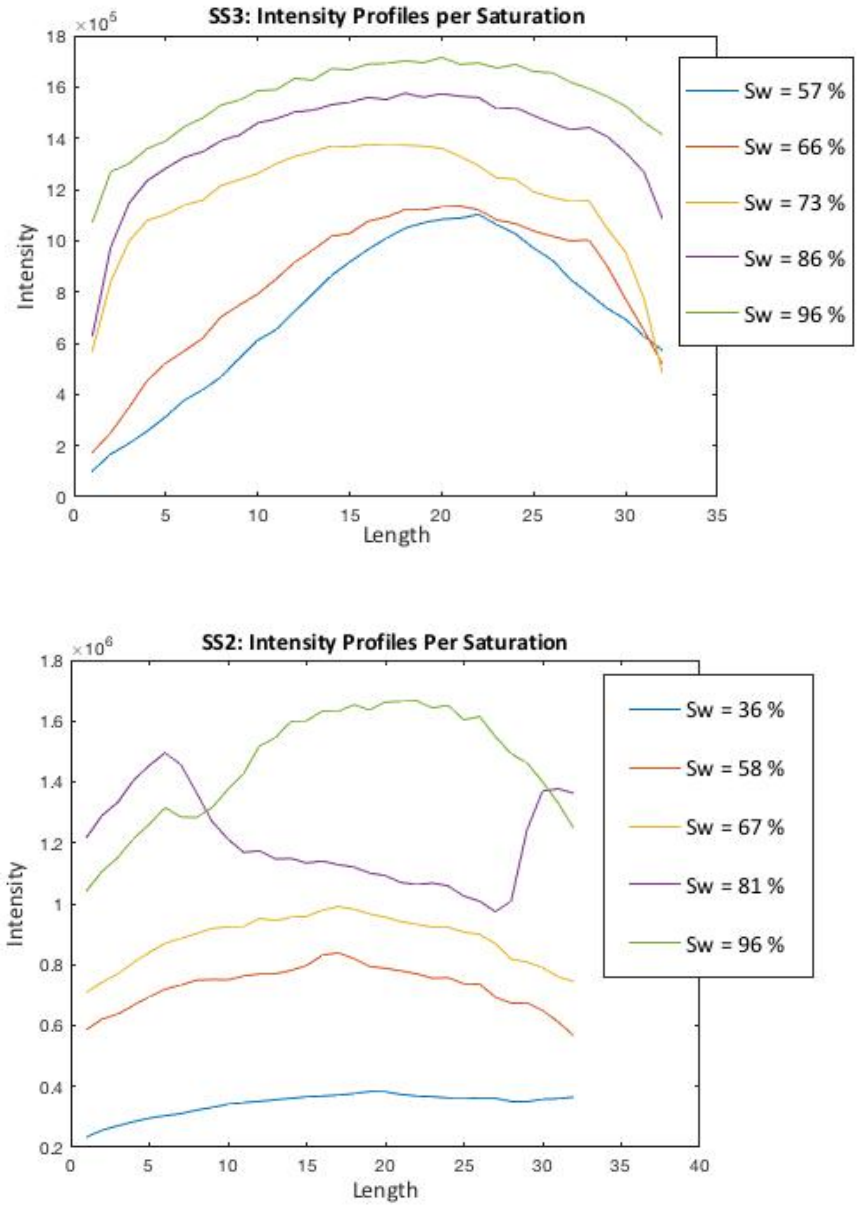

Figure 8-5 : Signal intensity profiles through the length of the core at the different saturations.

8.2.5 Correlating Signal Intensity and Water Saturation

Signal intensity and the amount of water, here referred to as saturation, should ideally have a linear relationship. The intensities of all the pixels of one measurement were summed, giving a value for "total intensity measured". Total intensity measured were plotted over saturation, for each core separate, (Figure 8-6 and Figure 8-7), and together, (Figure 8-8). A line with best fit to the points and intersection in (0,0) were added in all the plots. A residuals plot illustrating the point's deviation to the line were also added.

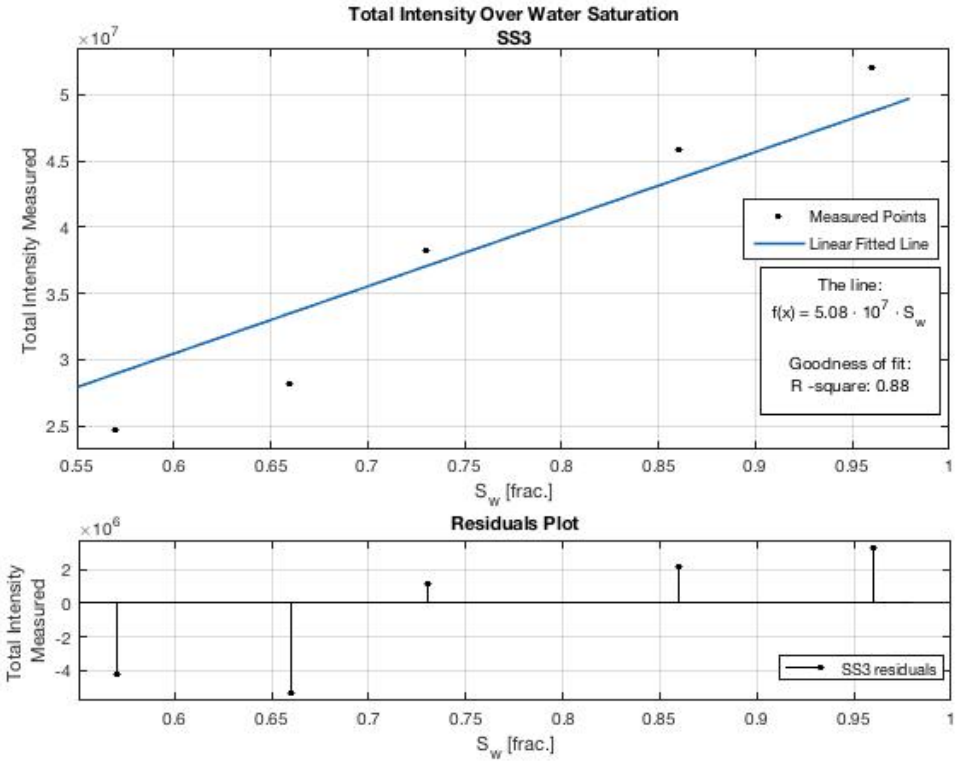

Figure 8-6 : SS3 Total measured intensity plotted over saturation. A line with best fit to the measured points and (0,0) is added in the figure. The equation of the fitted line is found in the figure, together with correlating R-square value. The residuals plot illustrates the deviation of the points.

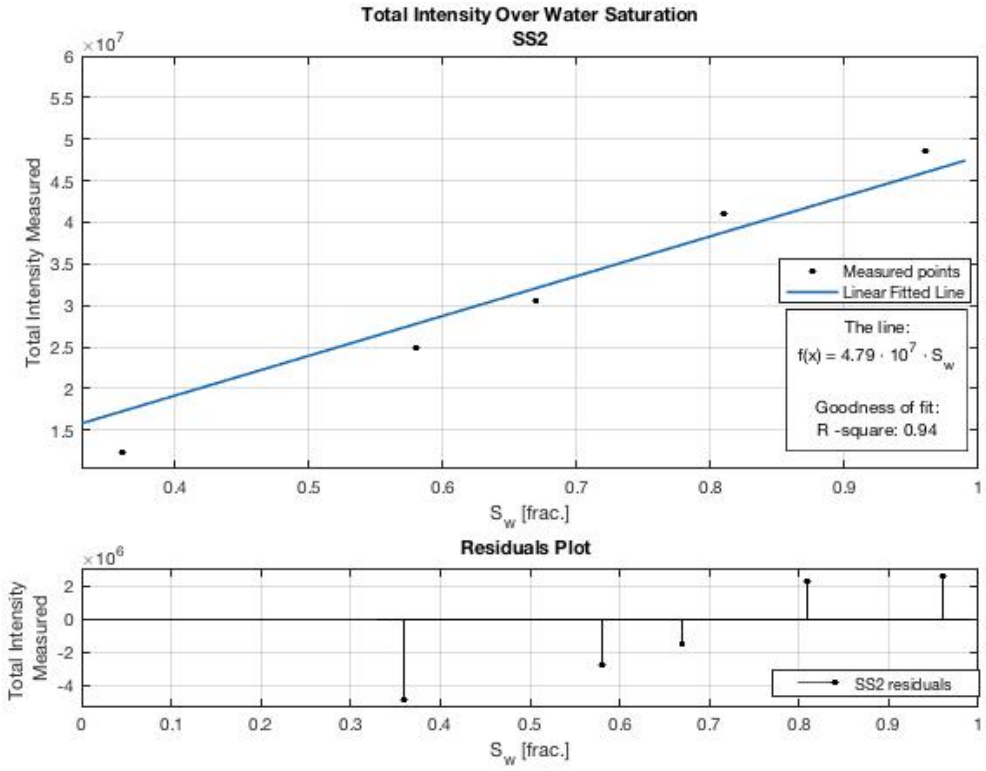

Figure 8-7: SS2 Total measured intensity plotted over saturation. A line with best fit to the measured points and (0,0) is added in the figure. The equation of the fitted line is found in the figure, together with correlating R-square value. The residuals plot illustrates the deviation of the points.

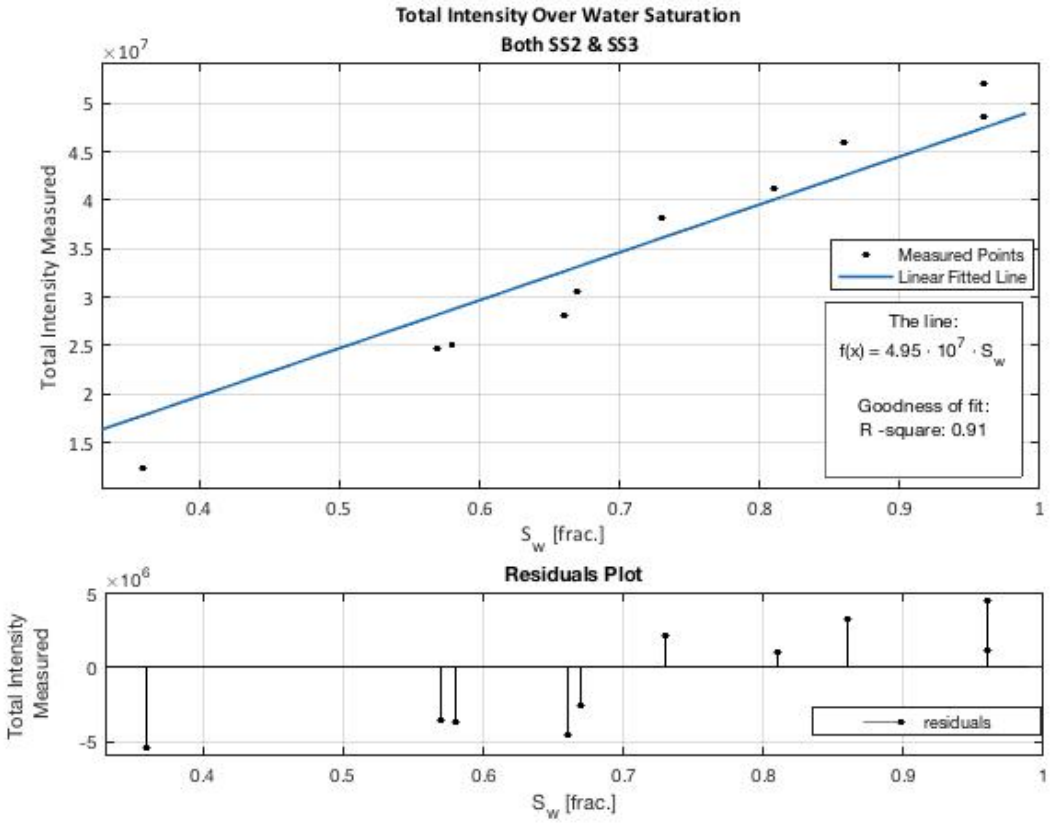

Figure 8-8: Both SS2 and SS3. Total measured intensity plotted over saturation. A line with best fit to the measured points and (0,0) is added in the figure. The equation of the fitted line is found in the figure, together with correlating R-square value. The residuals plot illustrates the deviation of the points.

The lines were in good agreement with the measured points. Goodness of fit are given as R-squares. Lines with a 100% fit to the points have R-square equal to 1. R-squares were found from 0.88 (SS3) to 0.94 (SS2). Putting the two cores in one figure gave a better fit for SS3 points, but less for SS2 points.

A trend of lower saturation points under the fitted line, and higher saturation points over, was identified for both core samples. The trend was visible both by the measured point versus the line, and in the residuals plots. Since the sandstone core is water wetting, water will have an affinity towards the surface of the pore walls, and fill the small pores first. As the saturation increases, so does the distance to the wall/thickness of the water layer. The trend of the points can therefore be explained by the fact that lower saturations will be more affected by the short surface relaxation. Lower saturations will have a higher fraction of water in contact with the pore walls versus free water in the pores. In other words, less signal will be generated as a result of the fraction between surface and pore bulk-volume relaxations, (when the scan protocol is T2 weighted). Illustration of a low versus a high saturated pore in Figure 8-9.

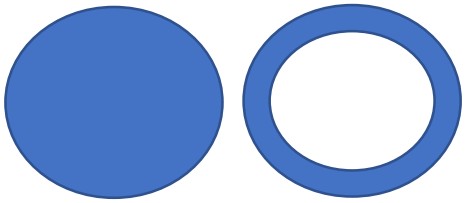

Figure 8-9: A simple illustration of a high water saturated vs. a low water saturated pore.

Even though the lines gave a good fit to the points, saturations including uncertainties of ±0.01 did not reach the line. The highest deviation of saturation to the line was found to be Sw = 0.11 [frac.]. The two points with the highest deviation were Sw = 0.36 for SS3, and Sw = 0.66 in the plot of both. A deviation of 0.11 of 0.36 is 31%. The given saturation points were estimated from weight measurements. The weight measurements were done before the core was put in the MR examination room. Most measurements were first done at the University when the cores were prepared, and later corrected at Statoil before the core was scanned. The weight-scale at Statoil were later found to be less reliable. There is a possibility that the uncertainties of the saturation points were underestimated.

A comment to the plot of both samples: Saturation was used as water scale, which were not accurate when looking at two different cores. The saturations are given in fractions of the pore volume, which was not exactly the same for the two samples.

To conclude, the linear relationship found from the saturation methods and scan protocols used here, gave saturations within 31% uncertainty. Overall, the lines give a relatively good indication of intensity and saturation dependency. The trend of lower saturations under and higher saturations over the line, may suggest better predictions with a line not necessarily intersecting in (0,0). A better fit between the points and the line could also possible been obtained by: more points, more accurate measurement techniques of saturation and/or another method of intensity quantification.

8.3 MSME – T2 RELAXATION

Three (of 12) slices from each of the MSME measurements were chosen for further analysis. Results from the MSME study are divided in two sections, and how these vary with saturations:

1. T2 distribution maps
2. Initial intensity value of the decay curves

T2 relaxation time values can be found in APPENDIX E.
Even though the T2 distribution maps generated from the MSME measurements of this study were shown to be unsuccessful, an analysis of the initial signal intensity of the decay curve gave interesting results. Initial signal intensity and water saturation were found to have a linear relationship, which can be used in water saturation predictions.

8.3.1 T2 Distribution Mapping

T2 distribution maps from the three slices for every saturation stage were generated. Figure 8-10 and Figure 8-11, displays the T2 distribution development with water saturation for each slice. The first observation is how the distribution profiles increase with increased water saturation. However, the shape of the T2 distributions are not in agreement with literature about T2 distribution in water saturated Bentheimer sandstone cores. The T2 distribution examples in Chapter 3 – *Literature Survey*, illustrated one main peak with a lower plateau, an almost unimodal shape [51]. In comparison, the T2 distribution from SS2 and SS3 presented here gave mostly bimodal distributions. The unusual shape of the distributions may be a result of low quality data, and/or sensitivity of the program used to generate these distributions. As a consequence, these curves are not considered reliable for detailed description of the water in the pores, however they show the main characterization, of increased signal with increased saturation.

8.3.2 T2 Distribution Maps of SS3

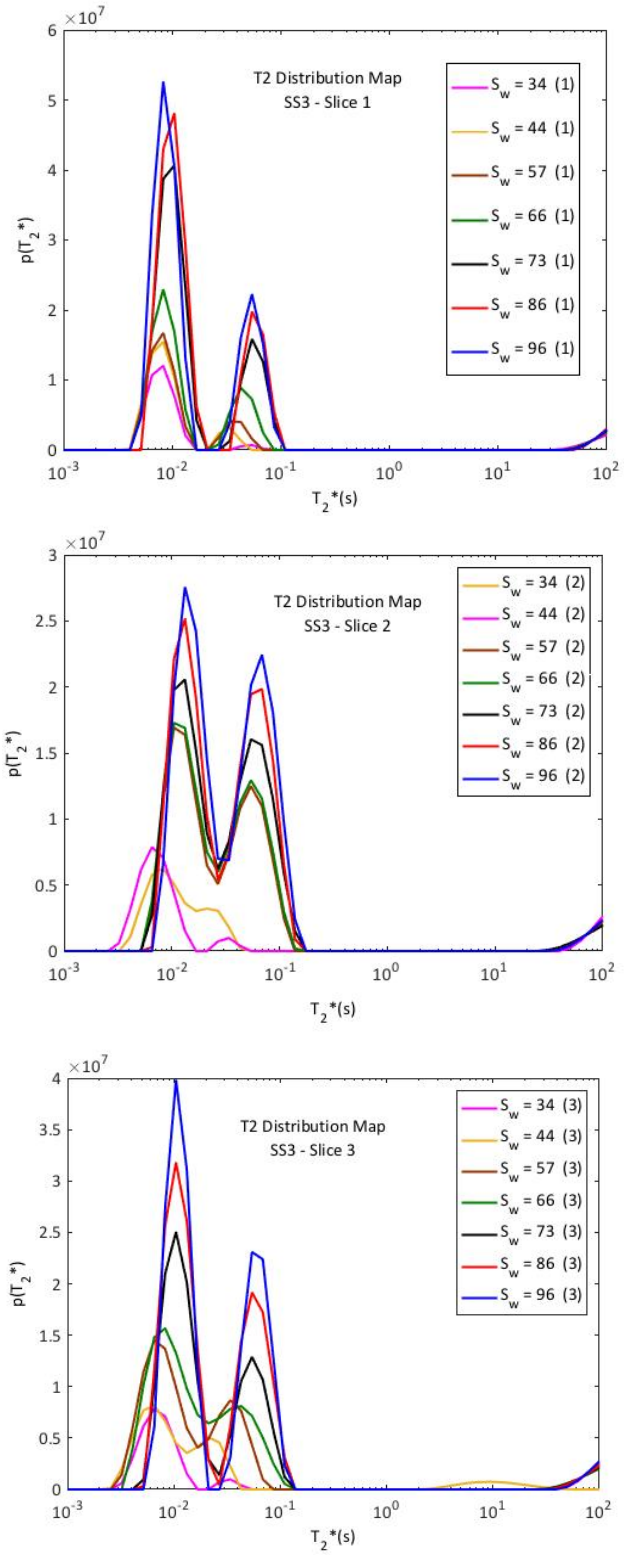

Figure 8-10: SS3 - T2 distribution maps, from the three slices. (Sw is given in %).

8.3.3 T2 Distribution Maps of SS2

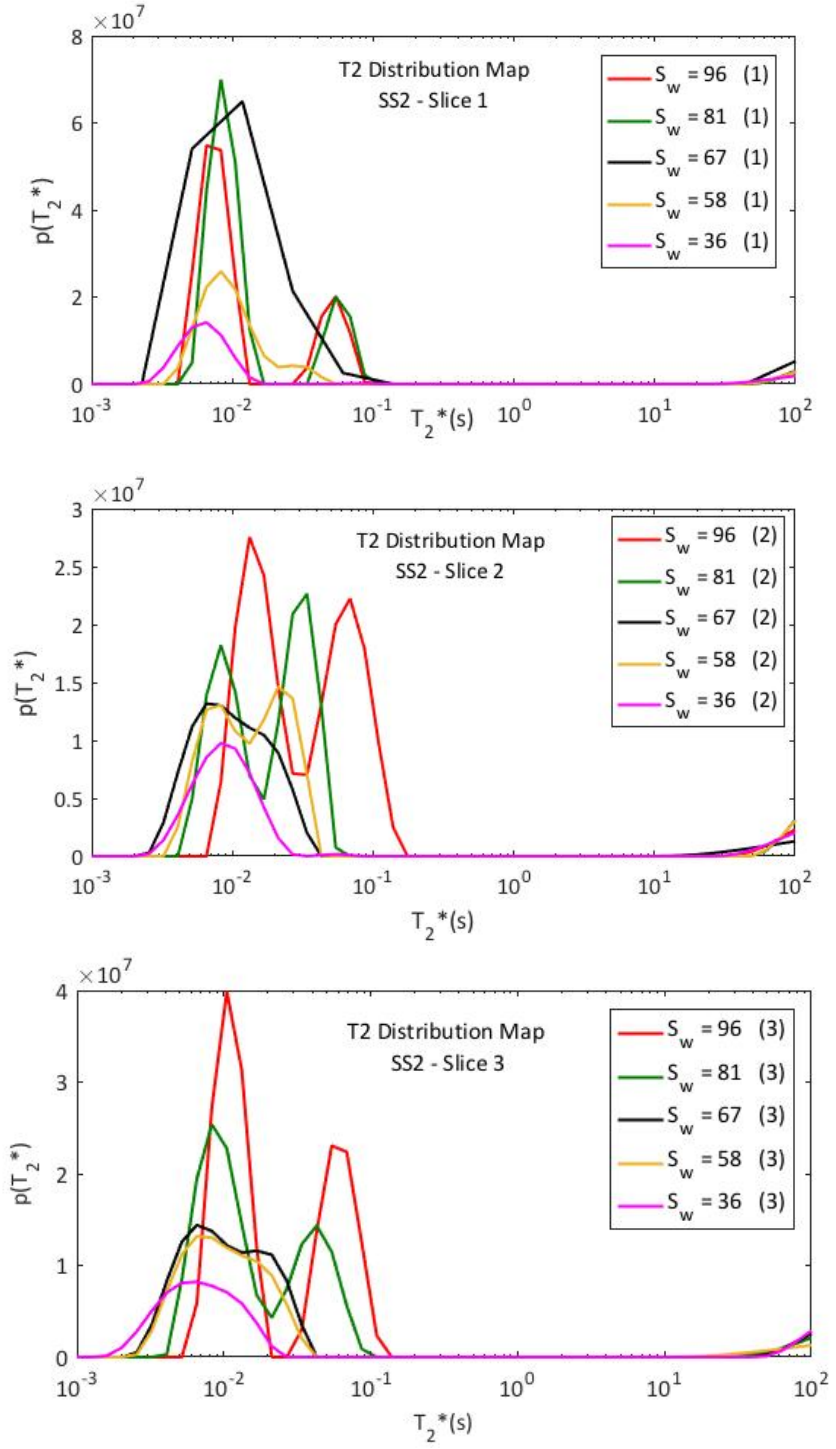

Figure 8-11: SS2 - T2 distribution maps, from the three slices. (Sw is given in %)

One detail worth mentioning in the first slice of SS2, is how the curve for Sw = 96% is found below the curve for Sw = 81%. This is in agreement with the RARE study, which illustrated that the local variation in this end shifted from higher saturation at average Sw = 81% to lower at average Sw = 96%. A similar shift was observed in the other end as well, but does not show in the third slice. The location of the third slice could be outside the elevated saturation zone.

Another curve worth mentioning is the black at Sw = 67%, in slice 1. Which has a different shape than the others, as well as it is placed between Sw = 96% and Sw = 81%. This is an example illustrating that this method and/or data are not able to quantify the saturation.

8.3.4 Initial Signal Intensity of the Decay Curve

In chapter 2.4, an equation for porosity was introduced by using the fraction of the initial signal intensity of the decay curve, for 100% water saturated pores over bulk water. This section looks at how these initial intensities vary with water saturation, as water saturation also is a "volume of water"-fraction: *Porosity is the fraction of pore volume of the total bulk volume. Saturation is the fraction of volume water in the pore volume.*

The MSME measurements gave the initial signal intensity of the decay curve directly for each slice. Water saturations with correlating initial signal intensity (*Ip)* of each slice and the average of the three, are given in tables for each core, SS3 in Table 8-1 and SS2 in Table 8-2.

First the average *Ip* (of the three slices) over water saturation of the core are illustrated, SS3 in Figure 8-12 and SS2 in Figure 8-14. The orange line (and points) illustrates the best fit to a linear relationship of the measured points in blue when intersecting in (0,0). The goodness of fit between the measured points and the line are given as R-square, where a 100% fit is given as R-square equal to 1.

Both plots of the average *Ip* show a linear relationship. The average values for SS2 seem to be more linear than the average values for SS3. The SS2 values gave a better fit to the line, with an R-square as high as 0.97, compared to SS3 which have a R-square of 0.89. An explanation may be that SS2 was generally more homogeneously saturated than SS3, resulting in better agreement with the average saturations.

Second a plot of the *Ip* of the individual slices over water saturation is presented, SS3 in Figure 8-13 and SS3 in Figure 8-15. The plots include also the orange line from the first plot, illustrating the best fit to a linear relationship of the average points. Lines with best fit to the points of the individual slices, and intersection in (0,0) were also added in the plots.

For SS3, the same trend as in the RARE study is observed. Generally, the highest value lies in the middle of the core. See Figure 8-13*:* the yellow points and line representing the slice in the middle gave the highest values in total. The plots of the individual slices indicate some more variation in the SS3 values, than in the SS2 values.

It must be emphasized that there is an additional uncertainty in the given water saturation of the slices, as the values used are the average found for the whole core.

8.3.5 SS3 - Initial Signal Intensity of the Decay Curve

Table 8.1: SS3 Initial signal intensity of the decay curve, Ip, of each slice and their average, for each saturation step.

Sw [frac]	0,34	0,44	0,57	0,66	0,73	0,86	0,96
Ip - 1. Slice	33,68	43,45	37,00	45,77	80,56	102,47	115,35
Ip - 2. Slice	28,63	41,56	78,96	84,90	104,46	123,28	147,83
Ip - 3. Slice	26,48	37,97	58,59	66,20	78,51	113,07	129,63
Average Ip	29,60	40,99	58,18	65,62	87,84	112,94	130,94

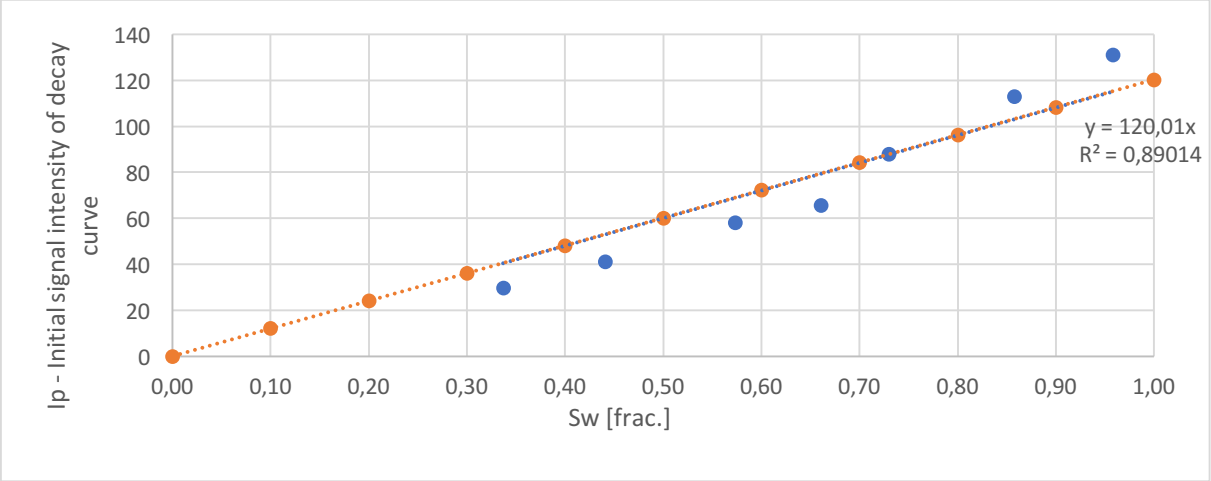

Figure 8-12: SS3 – Average initial signal intensity of the decay curve plotted over average water saturation, blue dots. A line (in red) illustrates the best fit of the linear relationship of the measured points when intersecting in (0,0). Red dots only illustrating the line. The equation of the line and goodness to fit, given as R-square, are given in the figure.

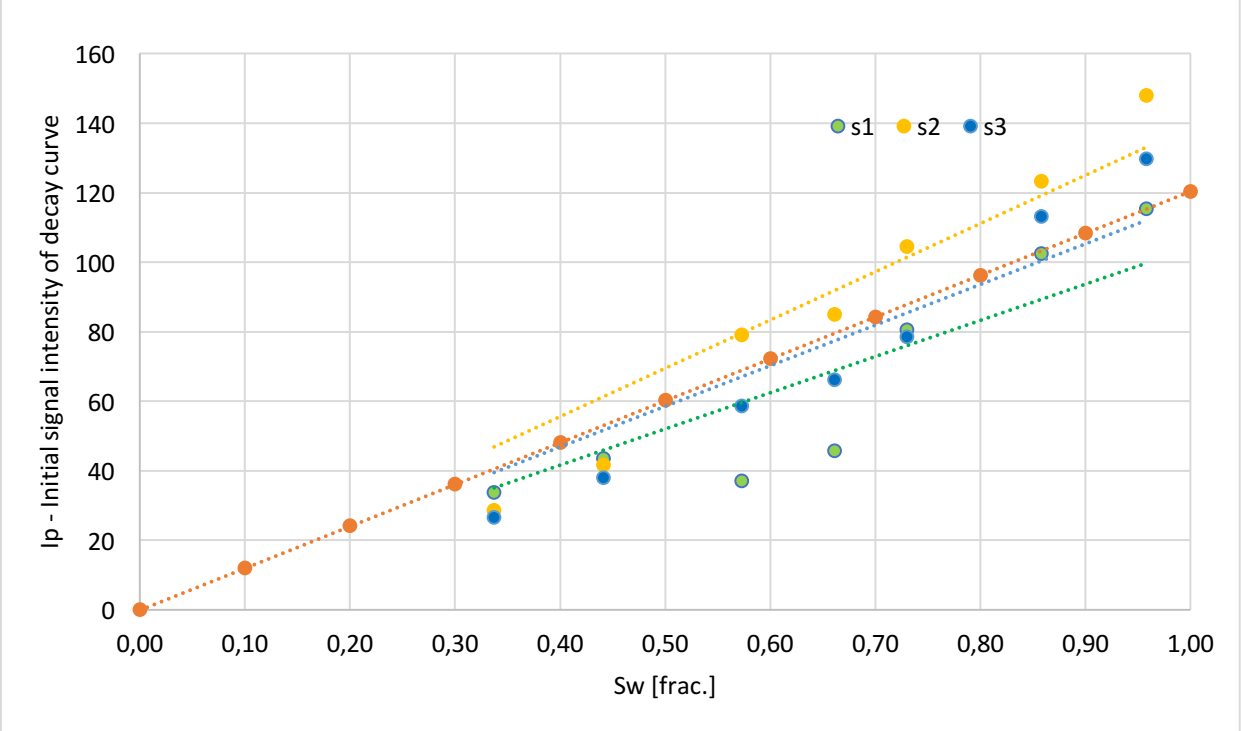

Figure 8-13: SS3 - Initial signal intensity of decay curve for each slice, over average water saturation. Dots and their best fitted line intersecting in (0,0): green – 1st slice, yellow – 2nd slice, blue – 3rd slice. Red is as in previous figure fitted to the average points.

8.3.6 SS2 – Initial Signal Intensity of the Decay Curve

Table 8.2: SS2 Initial signal intensity of decay curve, Ip, for each slice and their average, for each saturation step.

Sw [frac]	0,36	0,58	0,67	0,81	0,96
Ip - 1. Slice	51,16	94,98	101,54	106,21	90,62
Ip - 2. Slice	44,20	82,72	92,42	101,50	147,43
Ip - 3. Slice	43,79	73,39	79,88	94,66	129,63
Average Ip	46,39	83,70	91,28	100,79	122,56

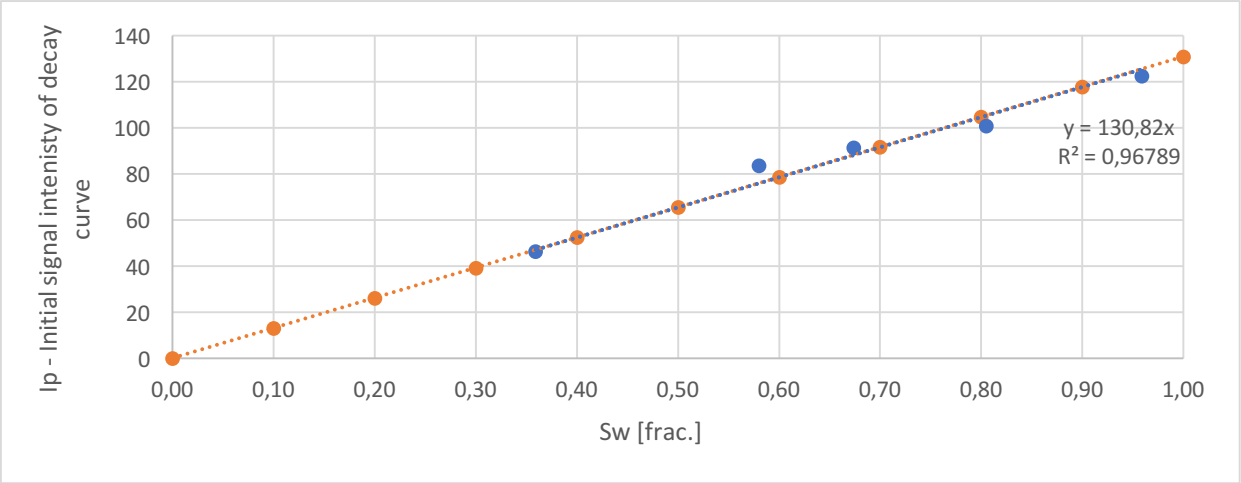

Figure 8-14: SS2- Average initial signal intensity of the decay curve plotted over average water saturation, blue dots. A line (in red) illustrates the best fit of the linear relationship of the measured points when intersecting in (0,0). Red dots only illustrating the line. The equation of the line and goodness to fit, given as R-square, are given in the figure.

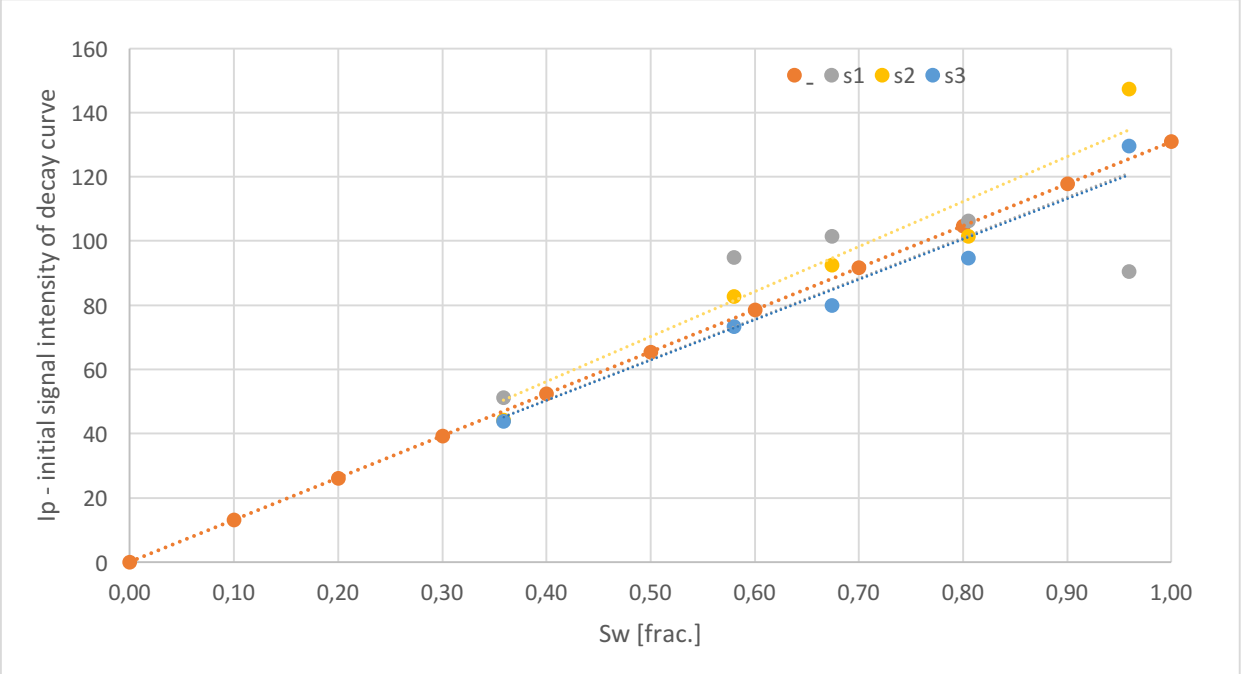

Figure 8-15: SS2 - Initial signal intensity of decay curve for each slice, over average water saturation. Dots and their best fitted line intersecting in (0,0): green – 1st slice, yellow – 2nd slice, blue – 3rd slice. Red is as in previous figure fitted to the average points.

9 THE HIGH-PRESSURE HYDRATE EXPERIMENT

9.1 SUMMARY OF THE STUDY

There are three parts of the high-pressure hydrate experiment that stands out in the results. A summary of these are given before the results are presented.

(1) PRESSURE BUILD-UP.
In the first part of the experiment, the pore pressure was increased from 40-100bar. As the pressure was increasing so did the gas content in the core. The MR signal was found to be relative stable in this period.

(2) HYDRATE STABLE PRESSURE PERIOD.
This part of the experiment started when the pore pressure was at 100bar, which is inside of the hydrate stable zone. After some scans, the gas supply line was closed, and the MRI data acquisition stopped. After a day, the acquisition was restarted and valves were opened again. Gas pressure dropped when opened to the core, and it was a visible loss of MR signal in the new scans.

(3) DEPRESSURIZATION
Right before the depressurization started, a pressure-pulse test was conducted, but no pressure communication was identified, indicating hydrate formation in the cell. In the depressurization part, there was a time period where the pore pressure was held constant with no acquisition. The next day, depressurization and acquisition continued until atmospheric conditions.

9.2 RARE

Data gathered from the RARE study is presented as (1) MR images, and (2) further processing of pixel intensity values. The MR images and figures in this section are based on the same DICOM files.

9.2.1 MR Images

All the 56 slices were put together in a montage-video, to visually analyze the large amount of data collected. The following pages shows a summary of the development. Each picture contains all the slice-images for a certain time, put together in a montage. The slices of the end of the core are often darker because they may contain a smaller volume of the core. In other words, the core is not necessarily less water saturated here. The first (top left) and last (bottom right) slices shows the gas supply line, or system pressure line. The white in the lines may indicate water that has been pushed out. Sometimes the structure on the end-piece surfaces became visible, as water accumulated in the circles, see Figure 9-1. For example, as in image number (5) (*Tiff 82)*.

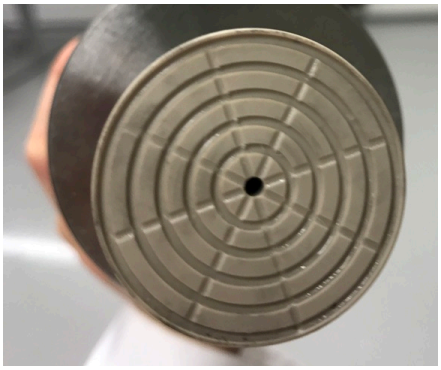

Figure 9-1: Structure on end-piece towards the core.

It is recommended to look at the montages together with Figure 9-3 in section *9.2.2 - Average water saturation of the core over time.*

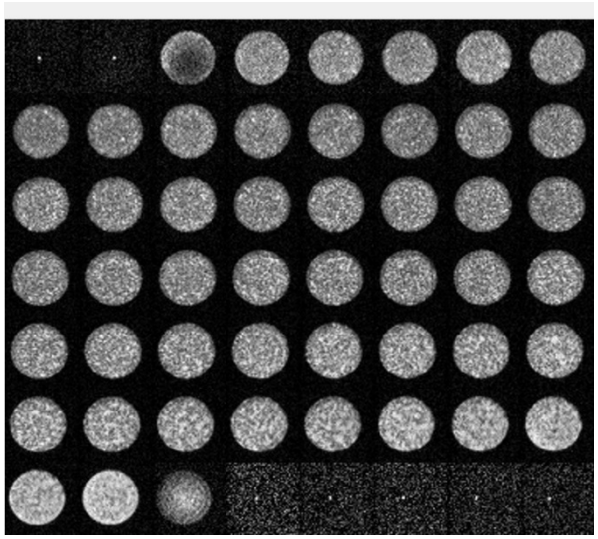

(1)
Montage of the first scan.
The cell was just mounted in the magnet. Pore pressure was approximately 40bars, and outside of hydrate stable region. (*Tiff 1*)

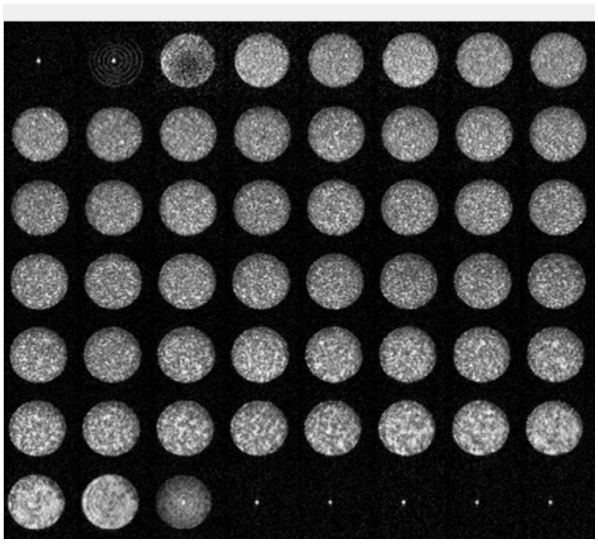

(2)
Last scan before recording stops.
Last known pressure was 100bar, but valves have been closed. Little change was observed, gas may have affected water saturation some, and contribute with some signal. Less noise observed around the line, indicating higher hydrogen content, gas or water, in the line. (*Tiff 45*)

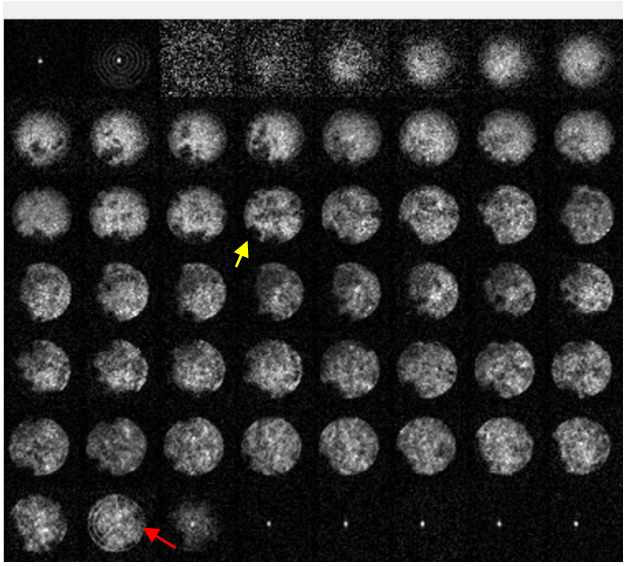

(3)
First scan when recording starts again.
Hydrate formation was visible as black spots. See example marked by the yellow arrow. The structure on the end-piece are more prominent, red arrow, and can indicate water accumulation. (Surfaces in pipelines have been covered in plastic to prevent hydrate formation on the wall). (*Tiff 46*)

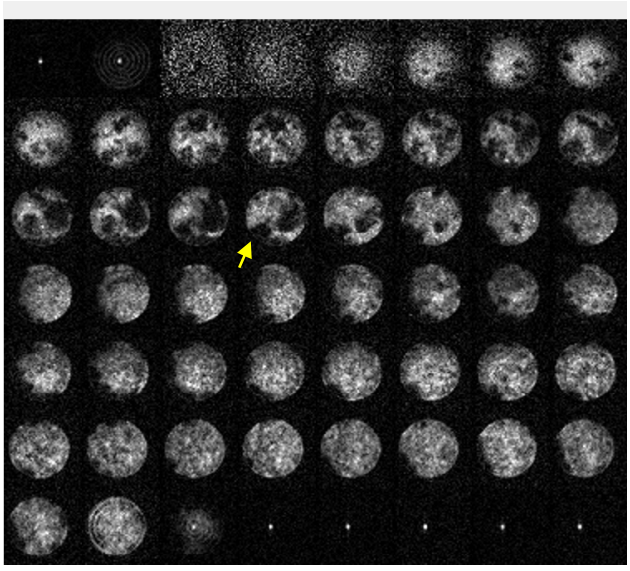

(4)
Last scan before the pressure pulse.
The images show more dark regions and larger dark spots than (3). For example, compare the two slices marked by the yellow arrows (3 vs. 4). Pressure reduction starts after this scan. (*Tiff 71*)

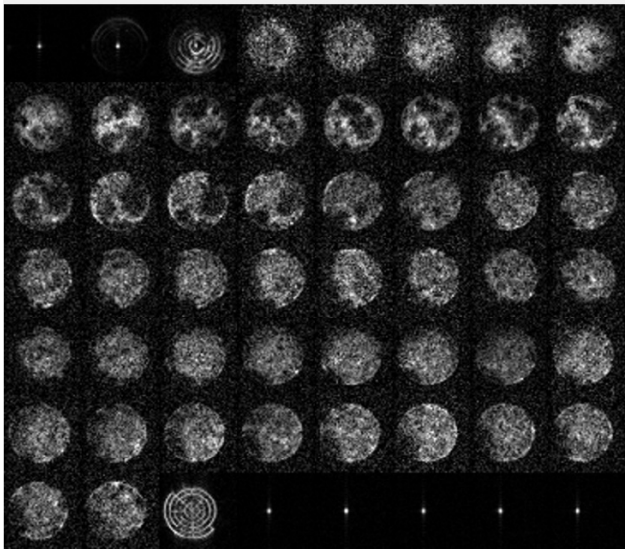

(5)
Pressure reduction.
Last scan before pause at 80 bar pore pressure. (*Tiff 82*)

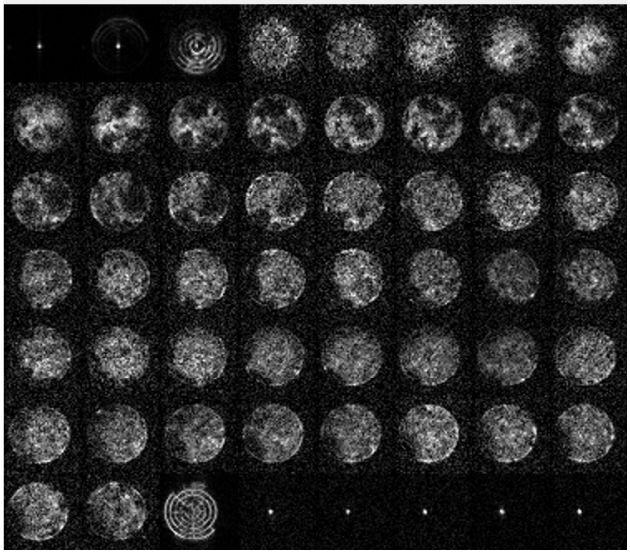

(6)
First scan when pressure reduction starts again.
No remarkable change observed. Still 80 bar pore pressure. (*Tiff 83*)

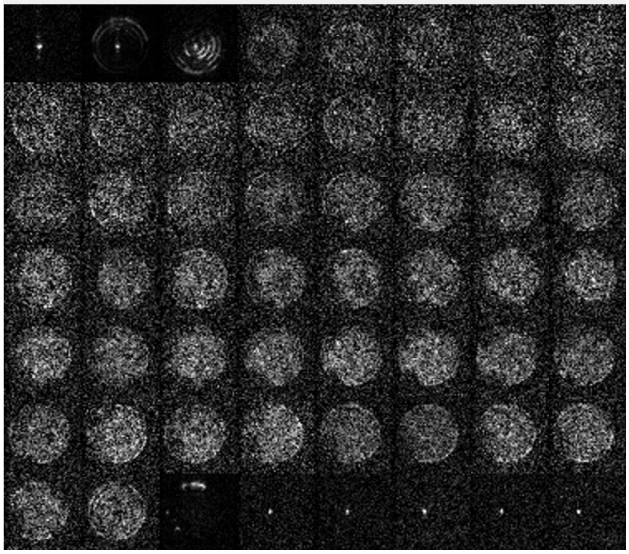

(7)
Pressure reduction continued.
This scan is the one with the least detected signal. (This will be visible in “Average saturation over time” figure). Water has been pushed out of the core. The noise became more prominent. S/N (signal to noise) ratio was much lower at this time, especially in the three first rows. (*Tiff 92)*

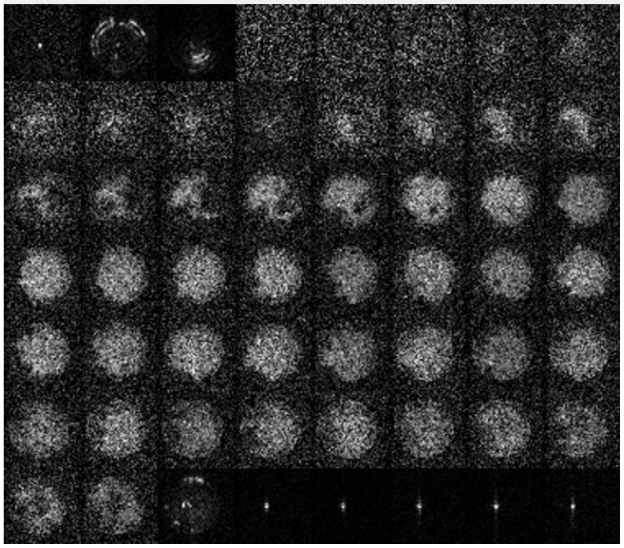

(8)
Signal starts coming back.
Still a lot of noise and some black spots visible. (*Tiff 116*)

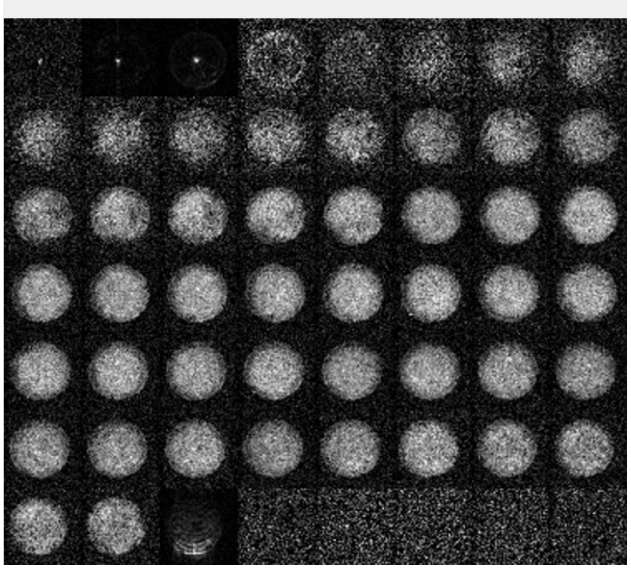

(9)
Even more signal was coming back.
Less dark spots. Center of the core lighter than the edges. More noise in the upper rows, where there were the most dark-spots. (*Tiff 119*)

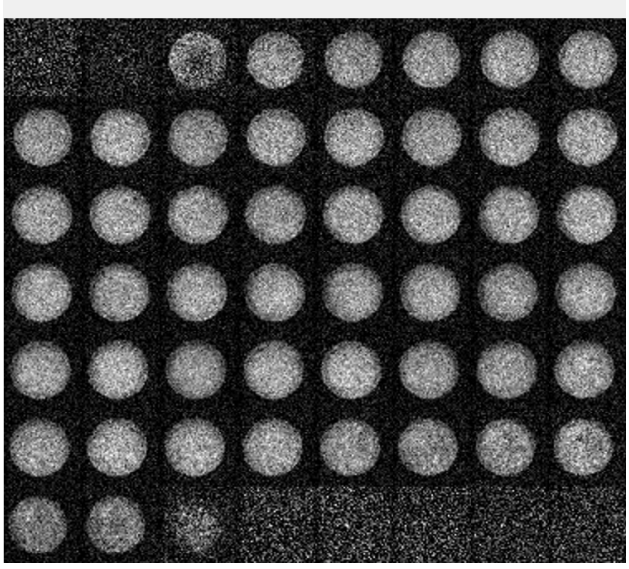

(10)
Tiff 128: Second last scan.
The signal reappearance indicated that the ends melted slower than the middle, and the edges slower than the center. The core was more homogeneous saturated at the end, but water saturation was strongly reduced.

Figure 9-2: Ten montages of images through the core, showing the development in the study. Details are described under the montages. The point of the montages, numbered 1-10, are marked in Figure 9-3.

9.2.2 Pixel Intensity Analysis

In this section figures made for further analysis are presented. The figures are made as functions of water saturation, estimated from pixel intensity of the images by Equation 2.14, (introduced in chapter 2.6).

First, Figure 9-3, illustrates the core as a whole, giving the average saturation change over time. The three pressure regions described in the introduction of chapter 9 are marked at the top of the figure, and the previous montages are marked by numbers.

(1) The pressure build-up period:
Water saturation was relatively constant. A saturation top is visible in the very beginning of the pressure build-up period. When people are working in the MRI room, the room temperature can be affected, and since the signal intensity of the MR measurement is strongly dependent on temperature, this can be a plausible explanation of the temporary top (increase and decrease). Another explanation can be some rearranging in the pores as gas was introduced and increased, also water may have been pushed out off the line.

(2) The hydrate stable pressure period:
The main trend in this period was signal loss. The fact that the valve was closed gave limitations of gas consumption and hydrate formation. When the valve was opened again more signal was lost, indicating that the hydrate formation continued. Because the recording stopped, detailed information of the hydrate growth is missing.

(4) Depressurization period:

This period was characterized first by signal loss, because free liquid water got pushed out of the sample by the depressurization. Thereafter the signal reappeared from water released by hydrate dissociation.

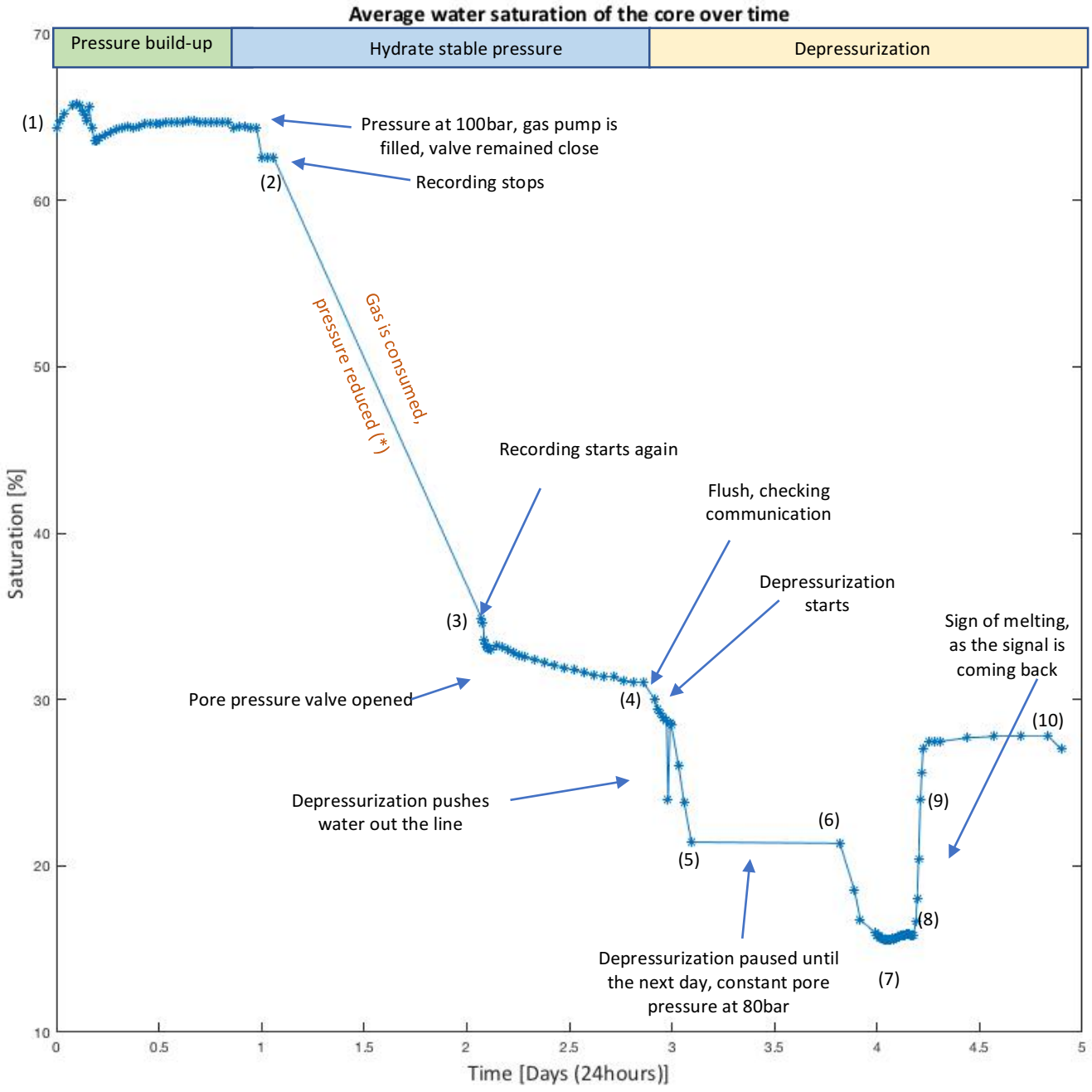

Figure 9-3: Average water saturation of the core through the study. Pressure regions illustrated at the top. Numbers illustrate where the MR images (above) belongs. Arrows and relevant information are included.

Figure 9-3 illustrates water saturation development of the core. Water saturations were estimated based on initial signal intensity and initial water saturation. Figure 9-4, illustrates the different saturations of water, gas and hydrate, in the core before and after hydrate formation. Estimations

were done by equations described in chapter 2.6. For this illustration, only the *hydrate stable pressure period,* from approximately 100 bar and until water is pushed out by depressurization, is represented.

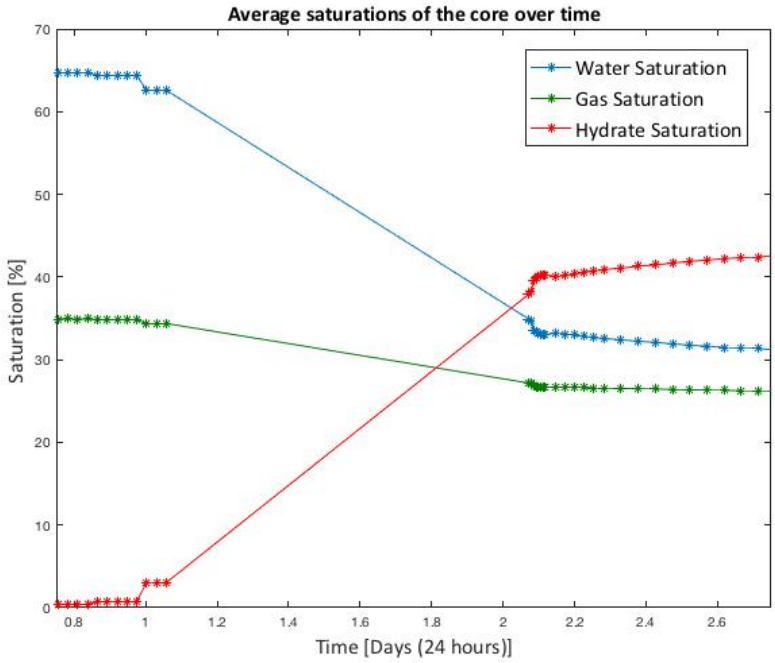

Figure 9-4: Average saturations through the core, before and after hydrate formation. Blue: water, green: gas and red: hydrate. Estimated from equations described in chapter 2.6, based on initial water saturation. This figure illustrates only the hydrate stable pressure region.

Following Figure 9-4, a hydrate saturation of approximately 42% is reached in this study. The lines got brighter (outside of the core) after the system was pressured up. If this signal came from water and not gas, the given initial water saturation will be overestimated. An overestimated water saturation will subsequently affect the estimated hydrate saturation, with less water available for formation.

Figure 9-3 and Figure 9-4 illustrated average water saturation of the whole core, the next section will include the water saturation variations through the length of core. Saturation estimations are based on initial intensity and initial water saturation. Because of the heterogeneous initial water saturation through the core, converting to hydrate saturation gave unrealistic values. However, the loss of water saturation will indicate hydrate formation (or water pushed out of the core), which will be enough for this illustration.

As for the saturation study, intensity maps, here converted to saturation maps were made. Both a two-dimensional saturation map, Figure 9-5, and a three-dimensional saturation map, Figure 9-6, will be presented. Four main regions became visible in the saturation maps: (1) The green-yellow region, representing the high water-saturation period, before hydrate formation. (2) The light blue region, with some green, representing the hydrate period. The blue line in this region are found as a drop of saturation in Figure 9-3 and Figure 9-5. In the end of the light blue region a gradation towards darker blue became visible. (3) The dark blue region, representing the depressurization period, where free water has been pushed out, and little signal was detected. (4) A second light blue region became visible. The reappeared signal represent water released from melted hydrates.

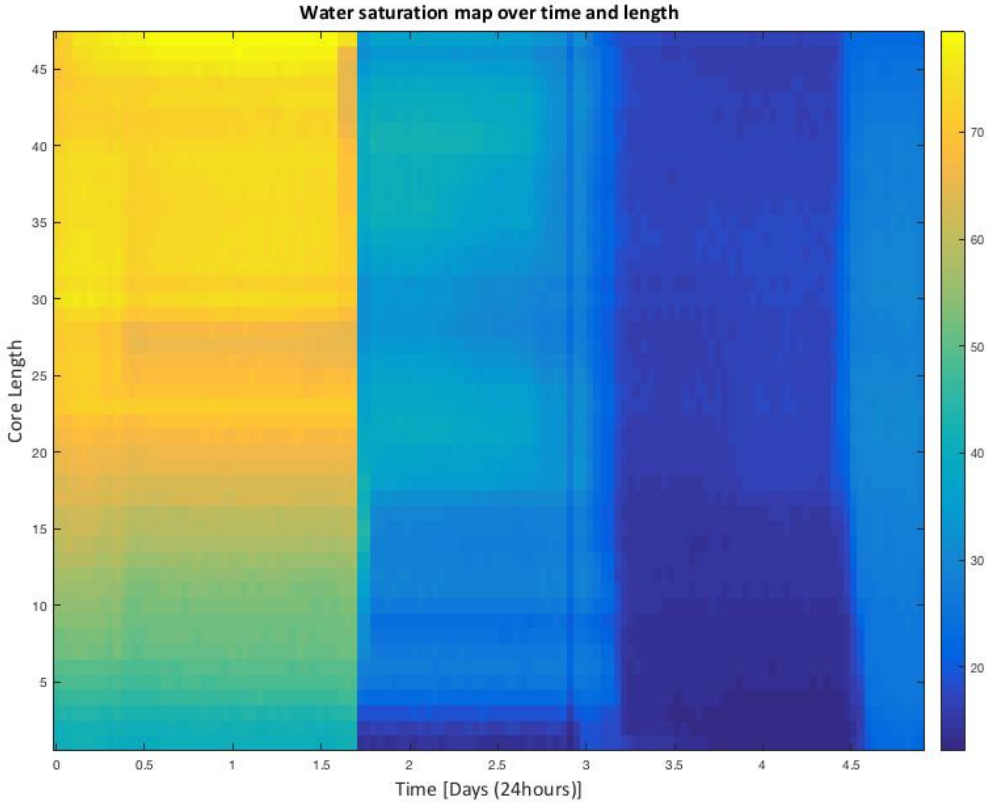

Figure 9-5 : Water saturation map. Each pixel in the map represents one slice at a certain time. The color-bar to the right shows water saturation [in %]. NB! Hydrate formation did not occur abruptly, the data for the growth time span is still lost. (This is better visualized in the next figure).

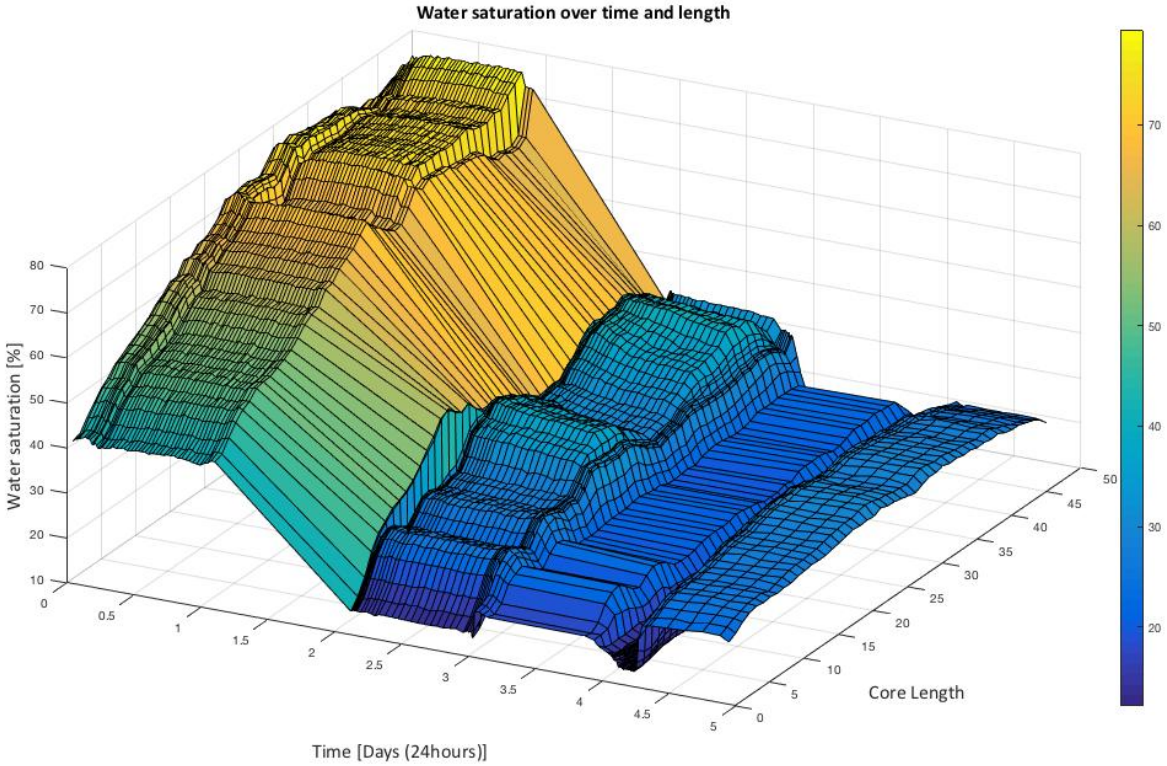

Figure 9-6: 3D illustration of water saturation over time and core length. The color-bar to the right illustrates water saturation [in %]. This plot is similar to the saturation map, only saturation is added as it sown axis, compared to the 2D map.

The maps gave information about the saturation distribution in the length of the core. Two regions of the core in the hydrate period are found to have higher water saturation than the rest. Water saturation in the hydrate period can be read from the maps to be 10 to approximately 43%.

To sum up the four regions found in the saturation maps, some selected saturation profiles through the core is illustrated in Figure 9-6. Notice how the profiles at regions (1) and (2) were more heterogeneous than the other two. In other words, after the depressurization, where water was pushed out and/or melted from hydrates, the water saturation became more homogeneous. However, it has to be emphasized that the water saturation was reduced from 65% to approximately 28%.

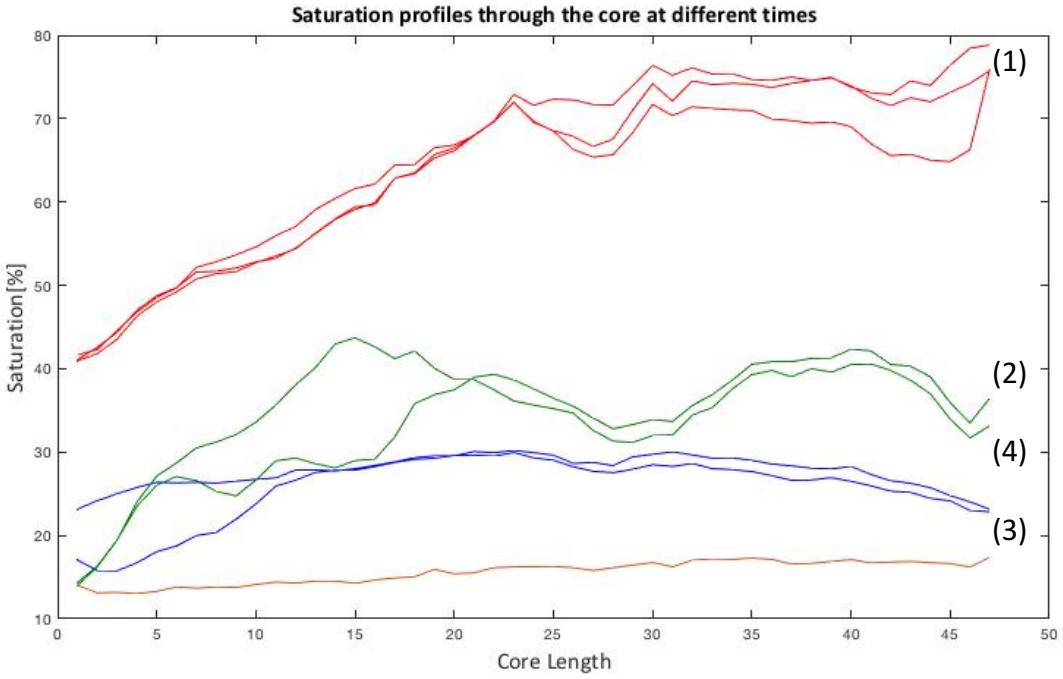

Figure 9-7: Saturation profiles of the core at different times. (Only 8 of 129 profiles are showed here). (1 - red): Pressure build-up until stable 100bar, the bottom red one last before scan stopped, (2 - green): Hydrate formation, top first after restarting scanning, bottom before depressurization, (3 – yellow): Depressurization reaching the point with the least signal detected, water is pushed out, (4 – blue): The signal increases as more hydrate melts.

9.3 CPMG – T2 DISTRIBUTION MAPPING

In contrast to the MSME measurements in the saturation study, CPMG measurements were found to be more successful when generating T2 distribution maps. CPMG measures the whole sample, in contrast to the slice selective MSME, giving less room for uncertainties. This section will look at the T2 distribution maps, divided in four periods, in addition to a summary of the whole experiment, and an estimation of hydrate saturation based on the T2 distribution maps:

(1) Pressure build-up,
(2) Hydrate formation
(3) Depressurization, where water is pushed out
(4) Depressurization, with visible melting
(5) Summary
(6) Estimation of hydrate saturation

9.3.1 Pressure Build-up

The T2 distribution map for the pressure build-up period are found in Figure 9-7. The pressure was increased from 40 to 100 bar. The pore pressure started outside, but ended inside of hydrate stable zone. As pressure was increased, more and more gas was introduced in the pore volume. The T2 distribution map illustrates increased distribution in the larger pores, and a distribution shift towards even smaller T2.

Since the sandstone core was water wetting (pore walls will be water-coated and water will fill the smallest pores), an increased density in the larger pores is in agreement with the theory. Smaller T2 values can indicate that even smaller pores were filled, by gas or water pushed by the gas. But also, a denser environment for the hydrogens may contribute to shorter relaxation times. Both as two phases of water and gas where the density of gas increases with pressure, and from gas saturating the water.

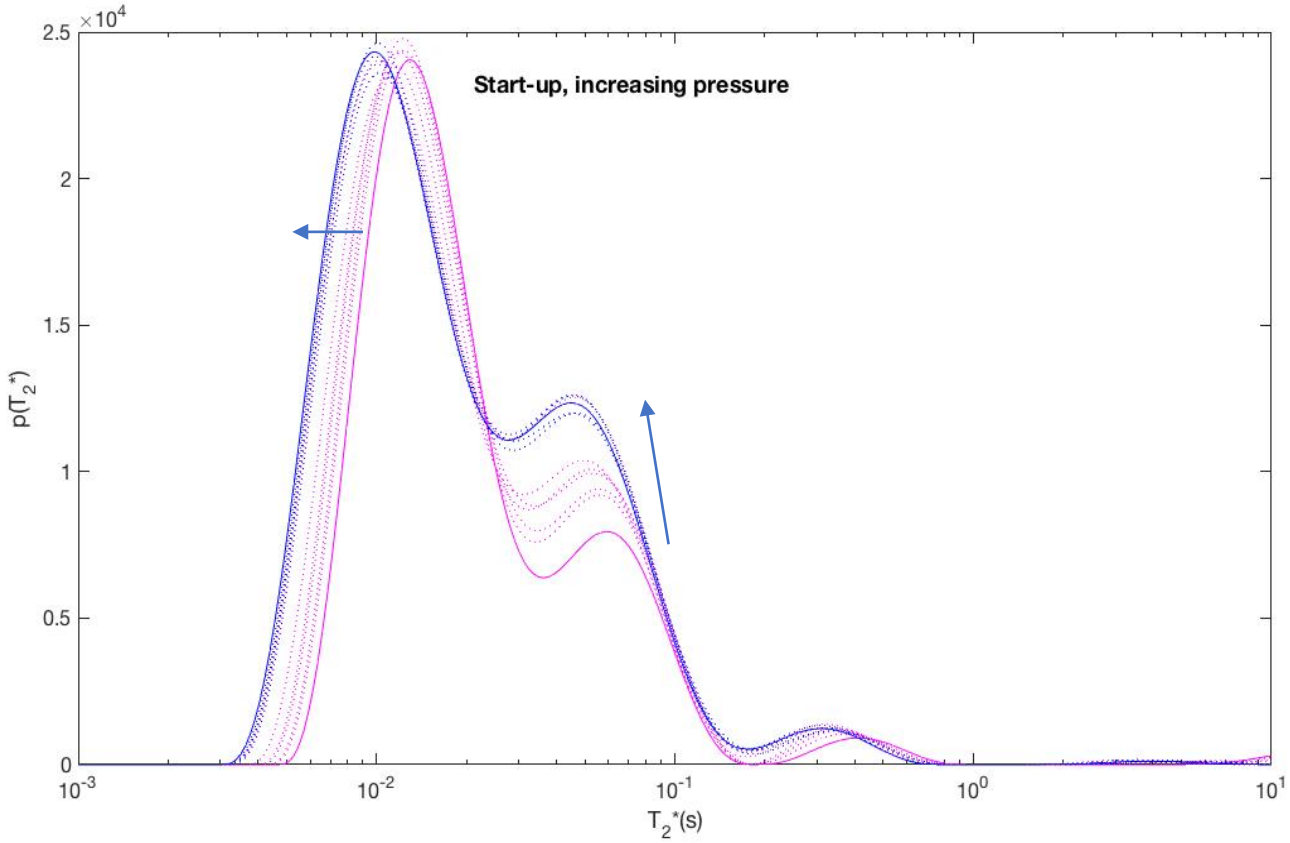

Figure 9-8: T2 distribution map of the start-up. illustrating the pressure build-up region in pink, starts at the solid line (40bar pore pressure). Blue is at 100bar pore pressure, the solid line is the last scan before recording stopped. The arrows indicate the trend movement of the curves. As pressure was increased more gas was introduced to the pore volume.

9.3.2 Hydrate Stable Pressure

The hydrate stable region is here presumed to start 100 bar. As described before, the valves to gas supply was closed, and opened again after a day. Meanwhile, gas had been consumed by hydrate formation, and a pressure drop was seen. After the gas supply was opened again (at 100 bar), even more signal got lost with time, indicating more hydrate formation.

From Figure 9-8, a clear signal loss is visible between the T2 distributions marked in black and blue, indicating the hydrate formation. It is not clear if there is a preferred pore size for hydrate growth, as the whole curve was reduced similarly. However, the top in the middle (larger pores) was flattened more.

The T2 distributions in Figure 9-9, were also found to have a shift towards shorter T2 values. This can be explained by the introduction of another solid surface (of the hydrate), and more surface relaxation. Also, the volume expansion of hydrate may push water in smaller cavities and/or small pores not introduced to water before.

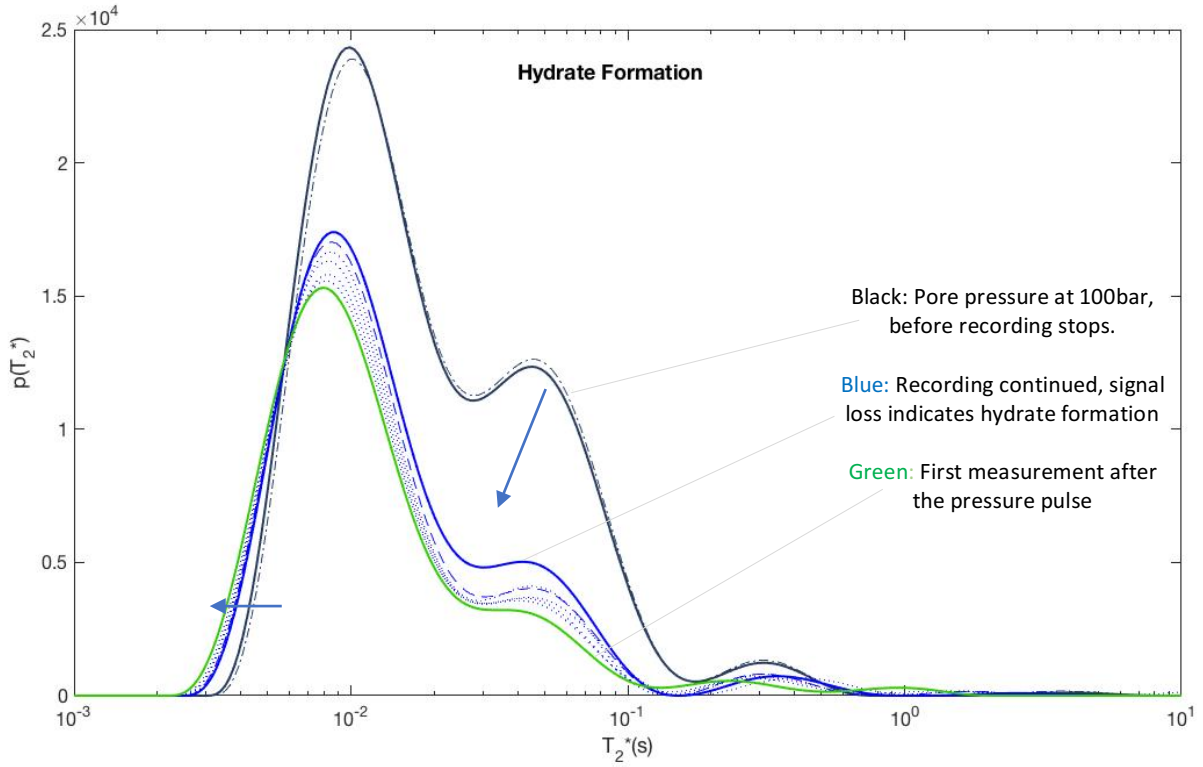

Figure 9-9: T2 distribution of hydrate formation region. Black solid line is the last measurement before recording stopped, (dashed black line is the first measurement at 100bar). Solid blue was the first measurement when recording was continued, blue dashed was first after valves to gas supply was opened again. Blue dotted was the development after this, until the green line, which was right after the pressure pulse. Arrows indicates the trend movement.

9.3.3 Depressurization

Depressurization are characterized by two different developments; first water was pushed out, resulting in signal loss, second, the signal came back, indicating liquid water from melted hydrate. The two developments are shown in Figure 9-10 and Figure 9-11.

The T2 distribution after the flush, or pressure pulse is marked in green in Figure 9-10. The flush was found to redistribute water in the pores, reaching larger pores. As the depressurization (water reduction) else follows the same distribution shape as with hydrate, the redistribution was seen as a temporary condition. However, there was a shift towards even larger pores as water was being pushed out. The primary development of the distributions in the first part of the depressurization, was the clear *signal loss*, the distribution shapes are similar but reduced in density.

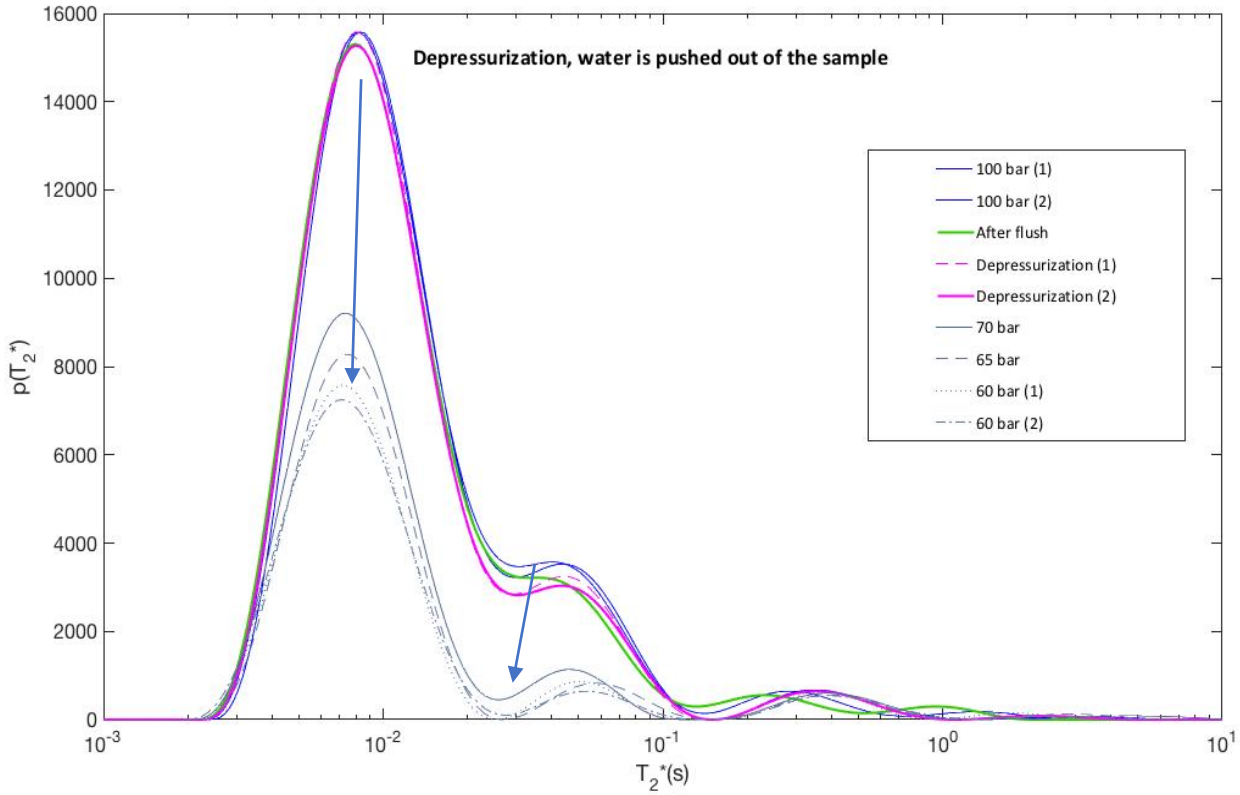

Figure 9-10: T2 distribution map for the first depressurization region, where the water was pushed out. This figure shows pore pressure region 100 – 60bar. Starting with the last blue curves from previous figure, and the green, after flush (pressure pulse). Depressurization start with the pink ones, going over to the grays, and decreasing as water is pushed out.

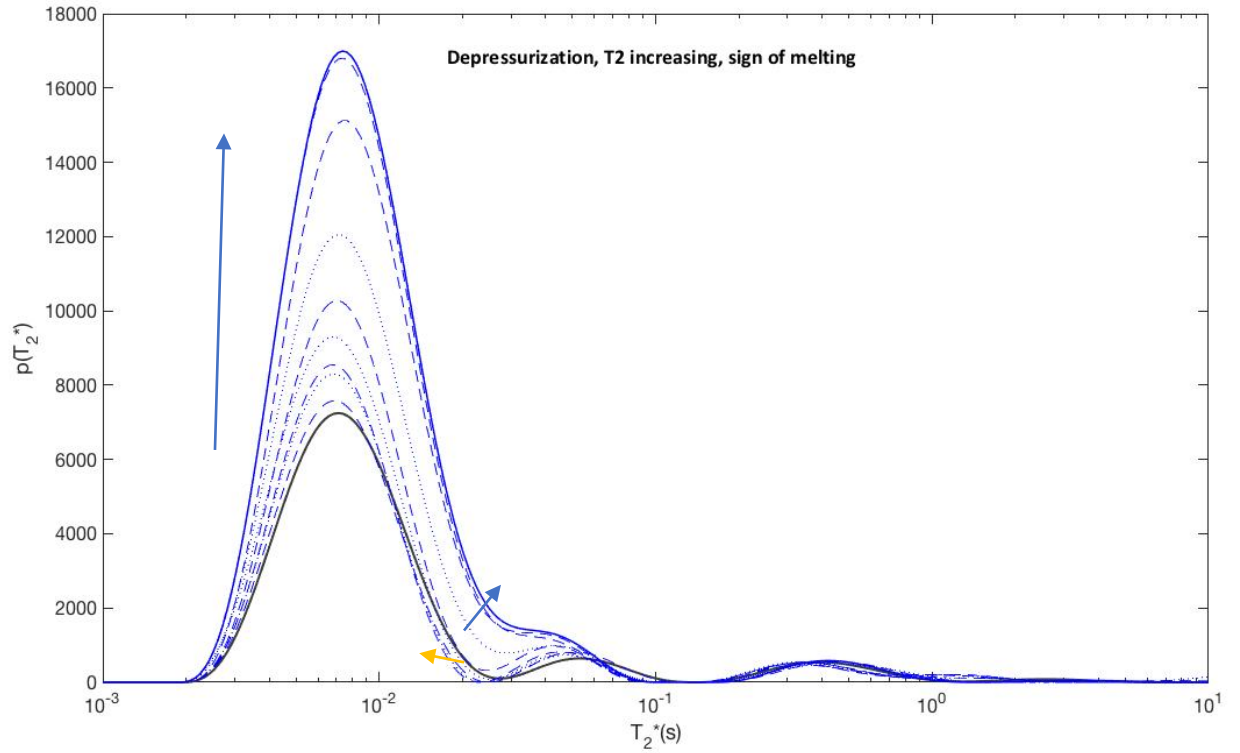

Figure 9-11: T2 distribution map for the second depressurization region, where the signal from water melted from hydrates increases. The black curve at the bottom is the last point from previous figure. This figure starts with the black at 60bar and grows towards the last at atmospheric pressure, the blue solid line, as the arrows indicate. Orange arrow shows a little shift to shorter T2 values in the beginning, but increases later with increased water saturation.

In contrast, the main development in the second part of the depressurization, was the clear *signal increase.* In the beginning, there is a little shift towards smaller pores (orange arrow). The shift may indicate more water going out, or water filling smaller pores as they become available. Thereafter the general trend shifts to increasing signal (blue arrows).

In contrast to the two first T2 distribution maps presented, Figure 9-8 and Figure 9-9, the T2 distribution maps of the depressurization, Figure 9-10 and Figure 9-11, does not retract the observed shift to the lower T2 values. In the depressurization period the distributions seem to decrease and increase from the short T2 obtained. In other words, the shift towards shorter T2 is an irreversible process. Which can make sense if the water was pushed to cover more surface, and/or trapped in smaller pores and cavities in the pore volume. If this is the case, then an assumption that irreducible water saturation will be increased after gas hydrate has been formed in the pores, can be done.

9.3.4 T2 Distribution Summary

A summary of the development is found in Figure 9-12. The main steps and trends here correlates with the main regions found in the RARE analysis, therefore the same color codes are used here.

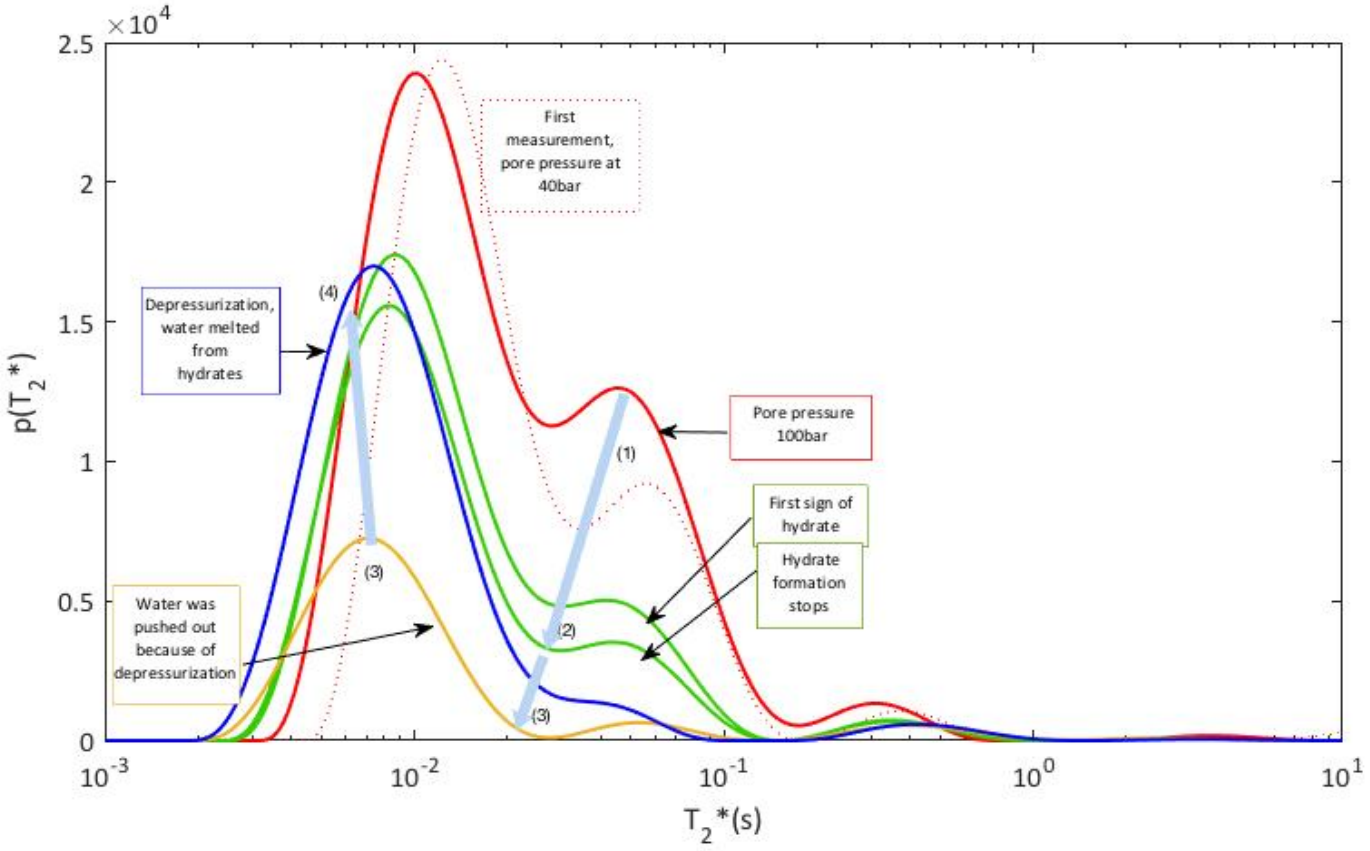

Figure 9-12: Summary of the main steps in the T2 distribution map development through the study. (1) Red: Pressure build up, (2) Green: Hydrate period, (3) Yellow: Depressurization pushed water out, (4) Blue: Depressurization, signal comes back as liquid water increases from melted hydrate.

To sum up some of the observations from the T2 distribution maps:

- Pressure build-up: Gas contributed in the T2 map as increased signal. Signal from larger pores were increased. In addition, new and shorter T2 values was observed.

- Hydrate formation: Hydrate formation was found as a drop of signal. In addition, a shift towards shorter T2 values was observed.

- Depressurization: When water was pushed out, the signal dropped even more. No shift was observed. The signal increased as water was released from hydrate. No shift was observed of the shortest T2 values.

- The shift towards the shorter T2 values was found to be an irreversible process, see red versus blue T2 distribution in Figure 9-12. The shift indicates an increased gas or water saturation in the smaller pores and cavities compared to the initial saturation of the core.

9.3.5 Saturation Estimation from T2 Distribution Maps

Because the T2 distribution curves represent the relative volume of water, a comparison of the curve before hydrate formation with known water saturation, together with the last curve of hydrate formation, can give an indication of (1) volume of water that has gone into the hydrate formation, and (2) estimates of hydrate saturation by using this volume of water. The fraction of remaining water can be found by the volume fraction, volume of the curve of remaining water, over volume of the curve of known saturation (without hydrate). See Figure 9-13.

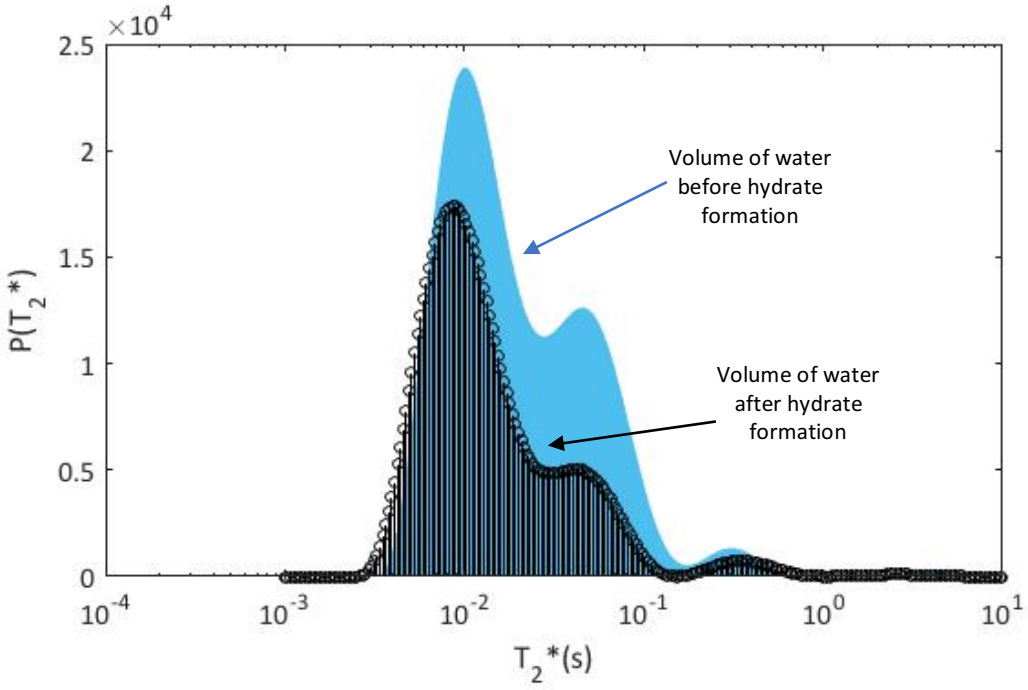

Figure 9-13: T2 distribution maps used in saturation estimations. Blue: The relative volume of water, when the pores are 65% water saturated. Black: The relative volume of water left after hydrate formation, unknown saturation.

The volume of the distributions was summed in MATLAB, and by using the principle described over, the fractions was estimated. The estimated water saturations and hydrate saturation are found in Table 9.1. Both the first distribution at 40 bar and the distribution at 100 bar were used as initial at 65% water saturation. The curve at 100 bar have more signal contribution from gas. They were compared to the distribution of the maximal reached hydrate formation. Hydrate saturation was estimated from the water differential multiplied with the expansion factor described in Chapter 2.6.3 - *Saturation Estimations*.

Table 9.1: Estimated hydrate saturation and corresponding water saturation.

T2 distribution map as S_w = 65%	Water saturation, S_w	Gas hydrate saturation, S_h
The first, at 40 bar	45%	25%
The one where 100 bar is reached, gas contributes to higher signal	34%	39%

The shape of the T2 distributions is depending on the settings in the program used to make them. Amongst other settings, how many exponential functions that are taken in consideration *(chapter 2.4.2 - Pore Size Distribution)* can affect the shape, which may affect the volume fraction.

Depending on which of the two T2 distributions chosen as S_w = 65%, different saturation estimations of water and hydrate were found. The saturation estimations from the T2 distribution at 100 bar correlates better with the estimation from the RARE study, with a hydrate saturation of 42%. The gas contribution to the signal when there is hydrate present is unknown here, but assuming it will contribute some, and that the curve at 100 bar is the more reliable of these two.

The accuracy and certainty of the program generating these curves are in need of further investigation/understanding, before detailed assumptions can be made for sure. However, a clear signal loss and growth represented the formation and melting of hydrates. In addition, the signal development was found to be in good agreement with the RARE measurements.

9.4 CPMG - Decay Curve and Initial Intensity

The same signal loss/growth trend found from RARE measurements and in the T2 distribution mapping, are also found in the signal decay curves from the CPMG scans, found in Figure 9-14. The T2 distribution maps are built on these decay curves. The color codes (described in the figure text) are used to illustrate the same regions as in the RARE summary and the T2 distribution map summary:

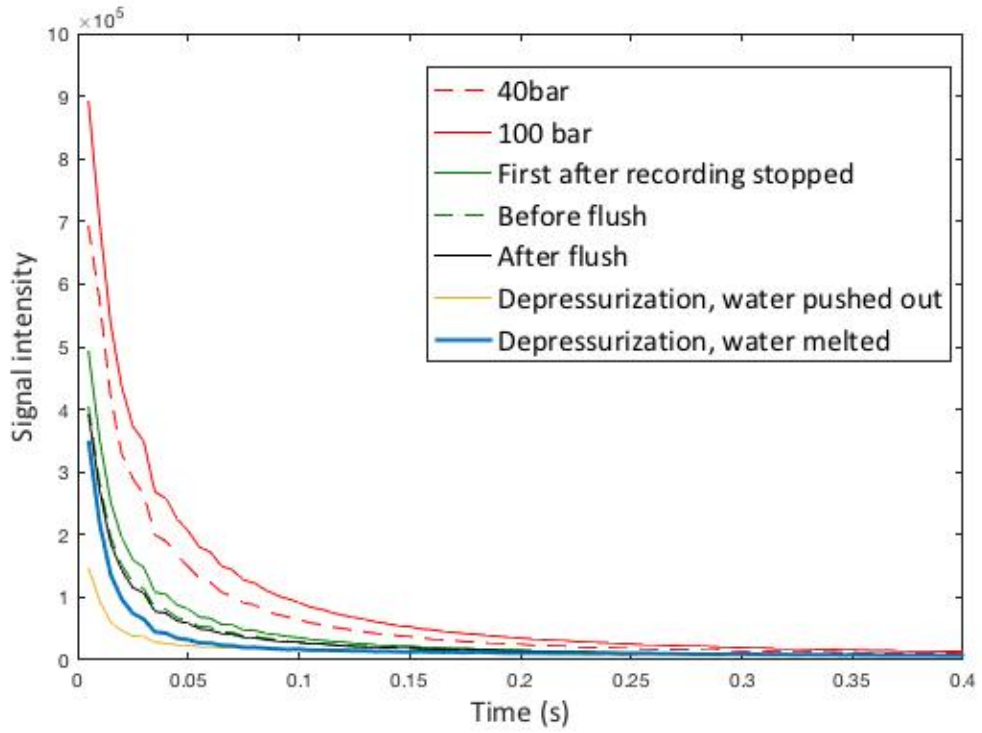

Figure 9-14: Signal decay curves from CPMG. Legend illustrates the different measurements. (1 - red): Pressure build-up until stable 100bar, the bottom red one last before scan stopped, (2 - green): Hydrate formation, top first after restarting scanning, bottom before depressurization, (3 – yellow): Depressurization reaching the point with the least signal detected, water was pushed out, (4 – blue): The signal increased as more hydrate melted.

In the saturation studies, the initial signal intensity of the decay curve was found to be a good indicator of saturation. As the CPMG measurements were sampled in a different type of file than MSME measurements, the initial signal intensity values had to be found outside of the ParaVision software.

First values from a curve fitting and extrapolation-session in MATLAB is presented, then values from the initial signal of the decay curves, displayed in Figure 9-14, is presented. None of the two methods gave the exact initial signal intensity, but they showed little difference, and indicated the same development. Figure 9-15 displays the initial signal intensity development through the high-pressure hydrate study.

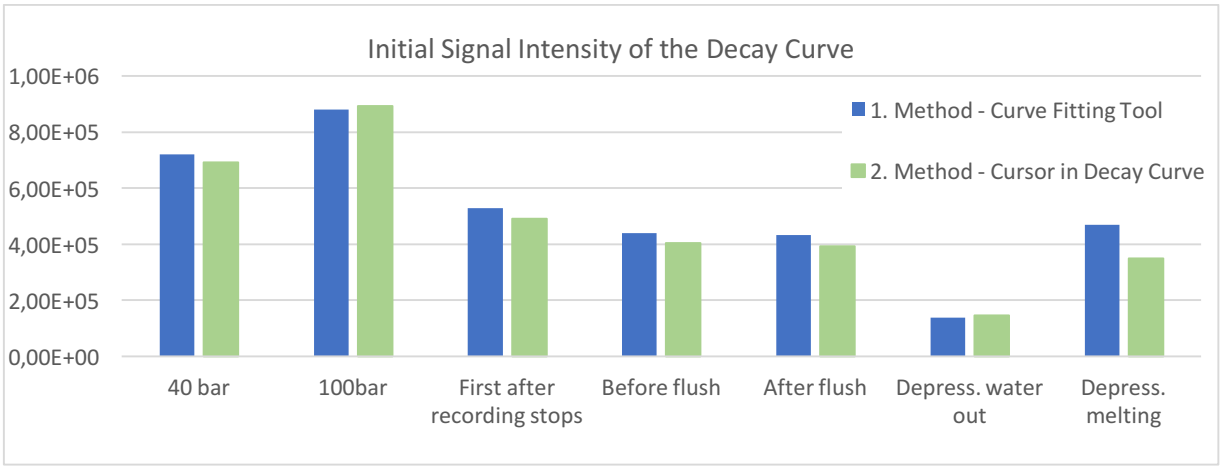

Figure 9-15: Initial signal intensity of the decay curve from: (1) First Method, blue, using the curve fitting tool in MatLab, plotting the "C-value" of the exponential decay equation. (2) Second method, green, plotting the decay curve, and using the built-in cursor function to find the first and highest intensity value. The initial signal values are found for the main steps/regions described for RARE and T2 distribution maps.

9.4.1 Saturation Estimation

Assuming the linear relationship of initial signal intensity of the decay curve, and saturation. A linear relationship illustrated by the saturation studies. The new water saturation in the presence of hydrate was estimated. Estimations were done using the initial known water saturation, $S_{w,initial}$, corresponding initial signal intensity, $I_{p,initial}$, and the new measured initial signal intensity, I_p:

$$S_w = \frac{I_p}{I_{p,initial}} \cdot S_{w,initial} \quad (9.1)$$

Estimations of the hydrate saturation, S_h, were done using the water saturation loss, which will contribute in gas hydrate formation, and the expansion factor:

$$S_h = \left(S_{w,initiall} - S_w\right) \cdot 1{,}25 \quad (9.2)$$

The saturation estimates of water and gas hydrate are displayed in Table 9.2. The results are divided by the methods gathering the initial signal intensity of the decay curve, and at which point (40 or 100 bar) used as 65% water saturation.

Table 9.2: Estimated reached hydrate saturation and corresponding water saturation, using the initial signal intensity of the decay curve.

Method	Water saturation, S_w	Gas hydrate saturation, S_h
CPMG 1. Method, $I_{p,initial}$ at 40bar	*40 %*	*32 %*
CPMG 1. Method, $I_{p,initial}$ at 100bar	32 %	41 %
CPMG 2. Method, $I_{p,initial}$ at 40bar	*38 %*	*34 %*
CPMG 2. Method, $I_{p,initial}$ at 100bar	29 %	45 %

The uncertainties of the CPMG intensity values are not given, also the methods presented here only give an approximated $I_{p,initial}$. However, the values using the initial intensity at 100 bar and the initial known water saturation of 65 %, are very close to the value estimated by the RARE method.

9.5 SUMMARY OF SATURATION ESTIMATIONS

Three different methods have been used to estimate the maximum hydrate saturation reached in the core, from the correlating water saturation at this point. A summary of the results is found in the table and figure below:

Table 9.3: Summary of the estimated hydrate saturations and correlating water saturations at this point.

Method	Water saturation, S_w	Gas hydrate saturation, S_h
RARE From figure of average saturation	31 %	42 %
CPMG – T2 Distribution Map The first, at 40bar	45%	25%
CPMG – T2 Distribution Map At 100bar	34%	39%
CPMG –Decay Curve *1. Method, $I_{p,initial}$ at 40bar*	*40 %*	*32 %*
CPMG –Decay Curve 1. Method, $I_{p,initial}$ at 100bar	32 %	41 %
CPMG –Decay Curve *2. Method, $I_{p,initial}$ at 40bar*	*38 %*	*34 %*
CPMG –Decay Curve 2. Method, $I_{p,initial}$ at 100bar	29 %	45 %

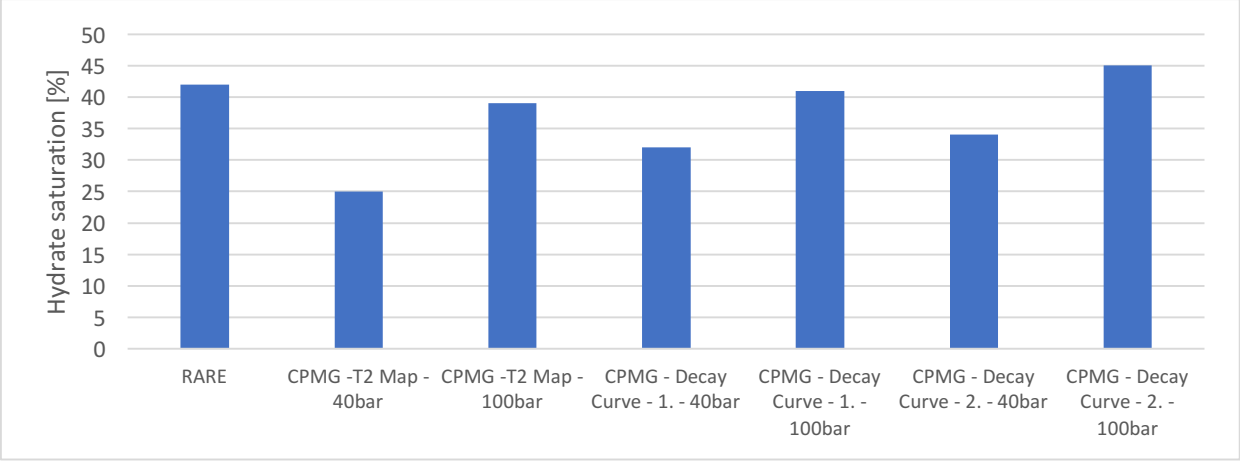

Figure 9-6: Bar plot of hydrate saturation estimations from the different methods.

In the figures, the RARE value was not given at which time the estimations were based on. The RARE measurements were less affected by the pressure build-up than the CPMG measurements. Estimations were done by using the average pixel intensity of the core at the 4 first scans from 40 bar. However, the average pixel value at 100 bar do not differ significantly from the value at 40 bar, (see Figure 9-3).

The estimations gave hydrate saturations in a region of 25-45%, depending on which intensity stage considered corresponding to the initial water saturation of 65%. If considering the results of CPMG using the 100 bar as reference point the most reliable, then hydrate saturation estimations were found to be in the region of 42±3 %.

All the estimations were calibrated to the initial water saturation of 65%. The MR images from the RARE study indicated that water had escaped to the line. If the initial water saturation was lower than 65%, all the result will be overestimated, as less water than assumed was available for hydrate formation. However, at this stage, the measurement and estimation methods are in focus. Since the results of the different methods are in good agreement, saturation estimations based on measurements attained from a high field strength magnet are found to be promising.

Part IV. CONCLUSION AND FURTHER WORK

10 CONCLUSION

The saturation study:

- The MR signal intensity was found to be strongly dependent on the water saturation of the core. This relationship was seen by both RARE and MSME measurements.
- The MR images showed high spatial resolution of the core. One pixel equals 1x1 mm^2, with thickness of 3 mm in the length of the core. Even though the resolution was not high enough to show single pores, it could tell if, and where, the porous media was even or uneven saturated.
- This thesis presents different methods to analyze the pixel intensities of the MR images. The methods were able to illustrate the spatial development of signal intensity through the core, as saturation was increased/decreased.
- The saturation methods where the core was submerged in water were found to give the most homogenous saturations in the core. When the core was vacuumed before submerged in water, even higher saturations were reached.

The high-pressure hydrate study:

- First of all, the new experimental design, using a high field strength magnet of 4.7 Tesla, was successfully applied in imaging and visualizing phase transitions of gas hydrate in the porous media of a sandstone core. This was done by RARE and CPMG measurements.
- In the MR images obtained from the RARE measurements, the hydrate formation was observed as signal loss, and dark regions were appearing in the images. One pixel in the image equals 1x1mm^2, with thickness of 2mm in the length of the core. For pixel analysis, larger pixels can be recommended reducing the number of data-files to be processed.
- T2 distribution maps and the initial signal intensity of the decay curve were obtained from the CPMG measurements.
- The two methods, RARE and CPMG, were found to correlate strongly in signal development. They presented the same trends in signal loss/growth at the same times of the study.
- Three different methods to estimate hydrate saturation were presented. The estimations were based on the differential in water saturation before and after hydrate formation, estimated from:
    - RARE – the pixel analysis
    - CPMG – the T2 distribution maps
    - CPMG – the initial signal of the signal decay curve

  The estimations gave hydrate saturations in a region of 25-45%, depending on which intensity stage considered corresponding to 65% water saturation. Considering RARE results, together with CPMG measurements when assuming that intensity found at 100bar corresponds to 65% water saturation, estimations of hydrate saturation were found to be in the region of 42±3 %. Since the results of the different methods are in good agreement, saturation estimations based on measurements attained from a high field strength magnet were found to be promising.

11 FUTURE WORK

First, since the high-pressure hydrate study was missing a crucial part when the hydrate was formed, a replica of this study should be done to improve the understanding of hydrate growth. Also, more details of the gas hydrate dissociation process should be targeted through further MRI experiments. Replica would also be important for the study's reliability, as these results are based on only one hydrate experiment.

The methods in estimating water saturation and hydrate saturation should be tested against other measurements. For example, gas consumption can be used to estimate hydrate saturation. Future work should also include permeability and porosity estimations when hydrate is present in the pore media. A method based on the T2 distribution maps is introduced in the literature survey (Chapter 3).

The experimental design of the MRI instrument should be improved with temperature control. This would make gas hydrate stable conditions easier to reach, and additional gases could be studied. For example, interesting MRI studies have been done on $CH_4 – CO_2$ exchange in gas hydrates in sandstone cores. Gas hydrates are suggested in CO_2 sequestration. Studies should be done to improve the understanding of the characteristics of such a scenario.

The software accompanying the MR instrument primarily intended for biomedical analysis, were found to be a bit challenging in core analysis. A software adapted to the use for core analysis could simplify and optimize the process. There is much room for improving the efficiency in both the data gathering and analysis.

This thesis pointed out the possibility of increased irreducible water saturation after the presence of gas hydrate in the pores. It is unknown if the water was pushed to existing pores or cavities previously not introduced to water, or if the hydrate cracked the core on a smaller level. As ice can fracture rock, so could possible gas hydrates. T2 distribution mapping can be used to further investigate this assumption.

Inspired by the saturation study, spontaneous imbibition of water can be studied by T2 distributions. Literature gives different theories about pore filling sequences: large versus small pores first, and whether it is the resistivity or capillary forces dominating the process.

PART V. APPENDICES AND BIBLIOGRAPHY

APPENDIX A– NOMENCLATURE AND ABBREVIATIONS

Nomenclature	Description
A	Contact area for hydrate towards the surroundings
A_i	Initial signal amplitude of decay curve for pore size *i*
B	Offset of decay curve
B_0	Magnetic field strength [T] (Applied magnetic field)
B_i	Local magnetic field strength (at location r_i) [T]
c	Constant from porosity calibration
C	Initial intensity of the decay curve
E	Energy
ΔG	Gibbs free energy
$\Delta g^{ph.tran.}$	The intensive change in Gibbs free energy related to the phase transition [J/mol]
G_T	Total gradient amplitude
G	Gradient
I	Intensity
I_0	Initial intensity
I_p	Initial intensity of the decay curve for water in pores
I_b	Initial intensity of the decay curve for bulk water
k	Permeability
M_0	Net magnetization
$M(t)$	MR signal as function of time t
$p(T_2)$	T_2 distribution
R_v	Expansion factor for water to hydrate
r	Radius
r_i	Location at magnetic field strength B_i
T_1	Longitudinal relaxation
T_2	Transverse relaxation time
$T_{2,LM}$	Mean transverse relaxation time
t	Time
S_{gas}	Gas saturation
S_h	Hydrate saturation
S_w	Water saturation
S_{w0}	Initial water saturation
I_0	Mean initial intensity
R_v	Volume ratio between water and water in gas hydrate
S_{gas}	Gas saturation
S_h	Hydrate saturation
$\frac{S}{V}$	Surface/volume ratio
γ	the interfacial tension [J/m^2] *Section 1.4*
γ	Gyromagnetic ratio [s^{-1}T^{-1}] *Section 2.2*
μ	Magnetic moment of a spinning nucleus
ρ	Surface relaxivity
ρ_N^H	molecular density [mole/m^3]
ϕ	Porosity
τ	Time (echo time intervals)

Acronyms	Description
BSR	Bottom Simulating Reflector
CPMG	Carr – Purcell – Meiboom – Gill pulse sequence
DICOM	digital imaging and communications in medicine
ds	Different settings
dTE	Different echo time
FID	Free induction decay (The MR signal)
GHSZ	Gas hydrate stability zone
H	Hydrogen
HPH2	“High Pressure Hydrate (2)” study
MR	Magnet Resonance
MRI	Magnetic Resonance Imaging
MSME	Multi Slice Multi Echo scan sequence
RARE	Rapid Acquisition with Relaxation Enhancement scan sequence
RF	Resonance Frequency
ROI	Region of interest
SE-SPI	Spin Echo Single Point Imaging - scan sequence
S/N	Signal to noise ratio
SPRITE	Single Point Ramped Imaging with T1 Enhancement - scan sequence
SS2	Sample in the saturation Study 2
SS3	Sample in the saturation Study 3
S/V	Surface to volume ratio
T1	Spin – lattice, or longitudinal relaxation time
T2	Spin –spin, or transverse relaxation time
TE	Echo Time
USGS	US Geological Survey

CH_4	Methane
C_2H_6	Ethane
CO_2	Carbon Dioxide
H_2S	Hydrogen Sulfide
NaCl	Sodium Chloride

APPENDIX B – CORE PROPERTIES AND SATURATION CALCULATIONS

SS2

The core	
Mass dry [g]	226,75
Length [cm]	10,25
Diameter [cm]	3,75
Porosity	0,244
Vb [cm3]	113,21
Vp [cm3]	27,64

Water	
NaCl [wt%]	0,1
Density [g/cm3]	1,001

Grain	
Density [g/cm3]	2,65
Volume [cm3]	85,566

Experiment	1	2	3	4	5
Saturated core weight [g]	236,67	242,81	245,410	249,01	253,27
Mass water [g]	9,92	16,06	18,66	22,26	26,52
Volume water [cm3]	9,91	16,04	18,64	22,24	26,49
SATURATION [%]	35,85	58,04	67,44	80,45	95,85

SS3

The core	
Mass dry [g]	220,47
Length [cm]	9,95
Diameter [cm]	3,75
Porosity	0,243
Vb [cm3]	109,89
Vp [cm3]	26,70

Water	
NaCl [wt%]	0,1
Density [g/cm3]	1,001

Grain	
Density [g/cm3]	2,65
Volume [cm3]	83,196

Experiment	1	2	3	4	5	6
Saturated core weight [g]	246,08	243,39	239,980	238,13	235,77	232,25
Mass water [g]	25,61	22,92	19,51	17,66	15,30	11,78
Volume water [cm3]	25,58	22,90	19,49	17,64	15,28	11,77
SATURATION [%]	95,83	85,76	73,00	66,08	57,25	44,08

APPENDIX C – LESSON LEARNED FORM AN UNSUCCESSFUL EXPERIMENT

The core mounted with end-pieces and the lines, is easy to move. Should be kept in center and handled carefully, because the end-piece can easily slip out of sleeve. An example is a study done (HPH3), where one of the end pieces slipped a little out, leaving a weak spot in the sleeve, which fractured as pressure was increased. Shown in image below.

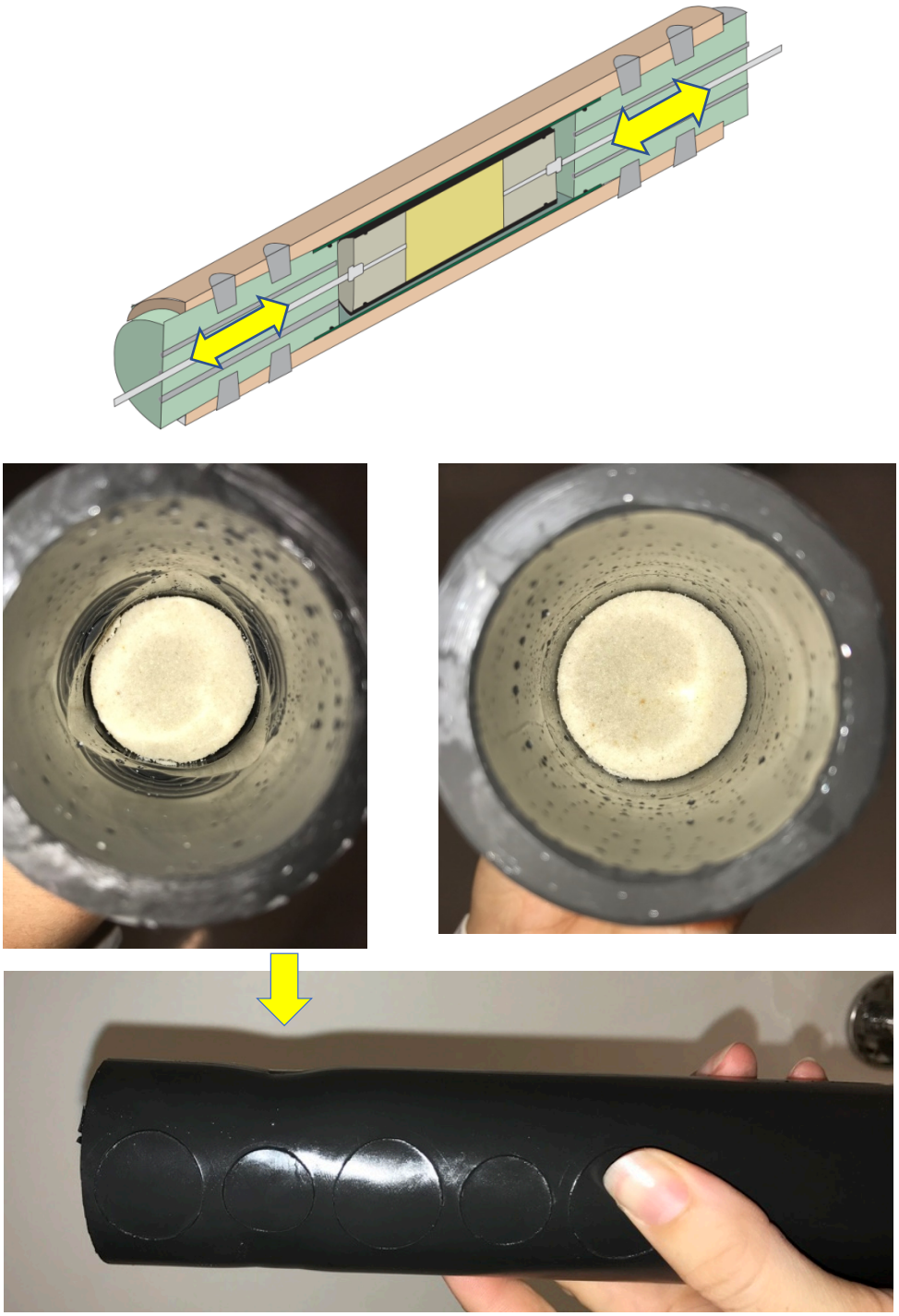

Figure C-1: Top: Illustration of the core holder, and the possible movement of the core in the sleeve mounted with the end-pieces. Below: images of the core in the sleeve. Left image show a fractured sleeve, and right a whole sleeve. Bottom image show where the end-piece had been moved out some, leading to the fracture in the sleeve.

APPENDIX D – MATLAB SCRIPTS

D.1: A_Dicom2IntensityMatrix.m
RARE. Used to read the dicom-files, and make a matrix of intensities in the right dimensions of length and time.

D.2: Image_v3.m
RARE. Makes tiff files of montages of all slices for one scan, and then making a movie of the tiff files.

D.3: B_Cropping_Intensity_Matrix_FIGURES.m
RARE. Cropping and making figures as function of intensity.

D.4: C_Cropping_Saturation_Matrix_FIGURES.m
RARE. Cropping and making figures as function of water saturation

D.5: T2_statoil.m
CPMG data: getting the signal decay curve, converting unix files to text files

D.6: 2D Laplace Inversion Program
CPMG/MSME. Signal decay curve: → T2 distribution map files

D.7: T2_plot
(CPMG/MSME. Plotting the T2 distribution map files

D.1 A_Dicom2IntensityMatrix.m

```
% Reads and manipulates dicom-files
%%
clear all;clc;

%%
% NB! Stay in "MATLAB" (over "Command Window") (St? i
mappen du har lagret
% scriptet i)

% Put in name of folder:
cd('./HighPressure2')

%%
% Checking folders:
folders=dir;
nfolderstot=size(folders);

% Check how many "fake" folders, and subtract the number
"b". (Here 3).
nfolders=nfolderstot(:,1)-3;

%%
% Start with the same number here: (b+1)
cd(folders(3+1).name);

%%
files=dir;
% Checking files
nfilestot=size(files);

% Number of dicomfiles, subtract number of "fake" files
ndcmfiles=nfilestot(:,1)-2;

% Generating length vector and matrix containing all slice
saturations
% (Zero - matrix ready)
length=linspace(1,ndcmfiles,ndcmfiles);
I1RescaleSum=zeros(ndcmfiles,nfolders);

% Going back to startfolder:
cd('../')
j=0; i=0;

%%

% For all folders j
for j=1:nfolders
   cd(folders(3+j).name);
   % Read all files (slices) i:
   for a=1:ndcmfiles
      i=i+1;

      filename = ['MRIm' num2str(a,'%02d') '.dcm'];
% Reading image matrix (All(:) x and y for slice(file) i in
time(folder) j)
      IMall(:,:,i,j)=dicomread(filename);
      % I1 intensity matrix pr slice
      I1=dicomread(filename);
      % Reading experiment and image information
      infoI1=dicominfo(filename);

      % Number of pixels in height and width
      npixelW=infoI1.Width;
      npixelH=infoI1.Height;
      % Pixelspacing (physical length/pixel number)
      pixelspacing=infoI1.PixelSpacing;
      pixelspacingHI1=pixelspacing(1);
      pixelspacingWI1=pixelspacing(2);
      % Physical height and width
      HI1=double(npixelH)*pixelspacingHI1;
      WI1=double(npixelW)*pixelspacingWI1;

      % Rescale (tilbake til r?-data)
      I1Rescale=double(infoI1.RescaleSlope*I1+infoI1.RescaleIn
tercept);
      % Sum of intensities pr slice
      I1RescaleSum(i,j)=double(sum(I1Rescale(:)));

      % Rescaled Matrix
      IMRall(:,:,i,j)=I1Rescale;
      xsat(i,j)=I1RescaleSum(i,j);
   end

   % Endrer p? tidsskalaen
   timeformat=[infoI1.AcquisitionDate infoI1.AcquisitionTime];
   datetime(timeformat,'InputFormat','yyyyMMddHHmmss');
   coretime(j)=datenum(datetime(timeformat,'InputFormat','y
yyyMMddHHmmss'));
   coresat(j)=sum(I1RescaleSum(:,j));

   cd('../');
   i=0;
   %j=j+1; ?
end

%%

% Sorting coretime, in increasing order,
[B,ind]=sort(coretime);

% Trekker fra alle tidspunkter det f?rste punktet for ? f?
differansen
% mellom tidene - "Tidsvektor":
timediff=double((B-B(1)));

% BB matrix of intensities (right order)
BB=I1RescaleSum(:,ind);
```

(Saving workspace)

D.2 Image_v3.m

```
%making tiff files and montage
%%
clear all;clc;
nh=7;nv=7;background=5;
%%
load SS2_sat.mat;

%%
%renumbering sorted files
%for i=1:ndcmfiles
for i=1:43
    Im(:,:,i,:)=IMRall(:,:,i,ind);
end
%%
% making tiff files in numbered folders
for k=1:nfolders
    foldername=['Tiff' num2str(k,'%02d')];
    mkdir(foldername);
    %for i=1:ndcmfiles
    for i=1:43
        I1=Im(:,:,i,k);
        Ip=imsubtract(I1,background);
        filename2 = ['MRIm' num2str(i,'%02d')
'.Tiff'];
        I2 =
uint8(255*double(Ip)/double(max(Ip(:))));
        set(gca,'DataAspectRatio',[pixelspacin
gHI1,pixelspacingWI1,1]);
        cd(foldername);
        I3=imresize(I2,2);
        %I4=imgaussfilt(I3,1);
        %II=imsharpen(I4,'Amount',4);
        imwrite(I3,filename2);
        cd('../');
    end
end
%%
% making filenames to use in montage
fileFolder = fullfile('Tiff01');
dirOutput =
dir(fullfile(fileFolder,'MRIm*.Tiff'));
file Names = {xxxxx';
cd('Tiff02')
montage(fileNames,'Size',[nh,nv]);
%set(gca,'DataAspectRatio',[pixelspacingHI1,pi
xelspacingWI1,1]);
cd('../');
%%
% making all montages
for m=1:nfolders
    foldername1 = ['Tiff' num2str(m,'%02d')];
    cd(foldername1)
    figure(i);
    montage(fileNames,'Size',[nh,nv]);
    set(gca,'DataAspectRatio',[pixelspacingHI1
,pixelspacingWI1,1]);
    mymontage=getframe(gca);
    imwrite(mymontage.cdata,['Montage'
num2str(m,'%02d') '.Tiff'],'Tiff');
    cd('../');96
    %hold on
end
%%
% making all montages in video
v=VideoWriter('testnew.avi');
v.FrameRate=1;
v.Quality=100;
open(v)
%myvideo1=zeros(1,nfolders);
for m=1:nfolders
     foldername1 = ['Tiff' num2str(m,'%02d')];
     cd(foldername1)
     filename_m=['Montage' num2str(m,'%02d')
'.Tiff'];
     imnew=imread(filename_m);

imshow(imnew,[]);
     set(gca,'DataAspectRatio',[pixelspacingHI
1,pixelspacingWI1,1]);
     hold on;
     myvideo1=getframe;
     writeVideo(v,myvideo1)
     cd('../');
end
 close(v)
%%
```

D.3 B_Cropping_Intensity_Matrix_FIGURES.m

```
clc; clear all;

% Loading workspace
load('HPH2all.mat')

%% Cutting the matrix

% "BB" is the matrix of intensities (56 x 129)
% Ends of sample is cutted to get rid off end effects
%
% EX here: 56 --> 47 (1:3 and 51:56 are removed) from BB
% Length and timediff have to be cut to fit dimentions

%%
% New BB cutted
Int_matrix=BB(4:50, :);

% Length cutted
length=length(:, 1:47);

% Timediff cutted
timediff=timediff(:,:);


%% INTENSITY FIGURES

%% 2D plot

% Intensity over length
figure(10)
plot(length,Int_matrix)
xlabel('Length')
ylabel('Intensity')


% Intensitet over time
figure (11)
Int_matrixI = Int_matrix';
plot (timediff,Int_matrixI)
xlabel('Time')
ylabel('Intensity')

%% Average Intensity of the slices (Average Intensity through the
core)

% Devide by number of slices used
avI=(sum(Int_matrix)/47);

% Plot average intensity over time
figure(12)
plot(timediff,avI,'*')
title('Saturation development per slice over time')
xlabel('Time')
ylabel('Intensity')

%% Intensity map for time and length

figure(13)
imagesc(timediff,length,Int_matrix)
title('Intensity map for time and length')
xlabel('Time')
ylabel('Length')

%% Making 3D figures INTENSITY
figure(14)
surf(timediff,length,Int_matrix)
title('Intensity over time and length')
xlabel('Time')
ylabel('Length')
zlabel('Intensity')


figure(15)
waterfall(timediff,length,Int_matrix)
title('Intensity over time and length')
xlabel('Time')
ylabel('Length')
zlabel('Intensity')
```

D.4 C_Cropping_Saturation_Matrix_FIGURES.m

```
clear all; clc;

%% From intensity ttoo saturation

% Henter workspace
load('HPH2all.mat');

%% Cutting the intensity matrix

% Skip first section under if you are not sure which parts to cut yet.


% "BB" is matrix of intensities (Here: 56 x 129)
% Ends of sample is left out to get rid off end effects
%
%
% EX here: 56 --> 47 (1:3 and 51:56 are removed) from BB
% Length and timediff have to be cut to fit dimentions

%% New matrix and vectors

% New BB cutted "intensity-matrix"
Int_matrix=BB(4:50, :);

% Length cutted
length=length(:, 1:47);

% Timediff cutted
timediff=timediff(:,:);


%% SATURATION MATRIX

% Initial water saturation (Fraction)
Sw_start=0.65;

% Matrix, intensities at initial water saturation
Sw1_matrix=Int_matrix(:,1:4);

% Average intensity at initial water saturation
I_start=(sum(Sw1_matrix(:)))/(47*4);

% Making a matrix of saturations, using initial water saturation and
corresponding intensity.
Sw_matrix=Int_matrix*(Sw_start/I_start);



%% Average Saturation of the slices (Average saturation through the
core)

% Devide by number of slices used

avSw=(sum(Sw_matrix)/47);

% Plot average intensity over time
% NB! Sw(0) should match "Sw_start" used above.
figure(1)
plot(timediff,avSw,'*-')
title('Average saturation through the core over time')
xlabel('Time')
ylabel('Saturation')

%% 2D plot

% Saturation over length
figure(2)
plot(length, Sw_matrix)
title('Saturation profiles through the core at different times')
xlabel('Core Length')
ylabel('Saturation')

% Intensitet over time (% Turning the matrix)
Sw_matrixI = Sw_matrix';
figure (3)
plot (timediff, Sw_matrixI)
title('Saturation development per slices over time')
xlabel('Time')
ylabel('Saturation')

%%
% Saturation map over time and length
figure(4)
imagesc(timediff,length,Sw_matrix)
title('Saturation map over time and length')
xlabel('Time')
ylabel('Core Length')
colorbar


%% Making 3D figures

figure(5)
surf(timediff,length,Sw_matrix)
title('Saturation over time and length')
xlabel('Time')
ylabel('Core Length')
zlabel('Saturation')

figure(6)
waterfall(timediff,length,Sw_matrix)
title('Saturation over time and length')
xlabel('Time')
ylabel('Core Length')
zlabel('Saturation'
```

D.5 T2_Statoil.m

```
%Program (or function) for procssing data obtained using the cpmg pulse
%sequence on the 4.7T scanner at Statoil.
%Final result is a T2-decay (magnitude)
close all
clear all

fid=fopen('fid','r','l');
data=fread(fid,'int32');
save -ascii -tabs t_data.txt data

td1=size(data);
% Setter inn "-" for ? snu kurven
ser_rs_fid=-data(7:256:td1);


save -ascii -tabs I_ser.txt ser_rs_fid



td2=size(ser_rs_fid);

t = [1:1:td2];
tau=input('What is echo time (ms) in the CPMG train? ');
t=t.*tau*1e-3;
t=t';


figure(2)
plot(ser_rs_fid,'*')

It=[t,ser_rs_fid];


save -ascii -tabs T2_data.txt It
save -ascii -tabs I_T2.txt ser_rs_fid
save -ascii -tabs t_T2.txt t

```

Provided by John Georg Seland, Department of Chemistry, University of Bergen

D.6 2D_Laplace_Inversion-program

From attached instruction manual:

"2D LAPLACE INVERSION INSTRUCTION MANUAL

Sophie Godefroy, Brett Ryland and P. T. Callaghan
Victoria University of Wellington, Wellington, New Zealand

This 2 dimensional so-called Laplace inversion is a program written at Victoria University of Wellington (Wellington, New Zealand) to process 2 dimensional ASCII data measuring in the two directions either diffusion or relaxation characteristics of heterogeneous proton systems. The program interface is written in Matlab whereas the code section that performs the bulk of the computation is written in C, making use of the Matlab "mex" external interface."

Redistributed by John Georg Seland, Department of Chemistry, University of Bergen

D.7 T2_statoil.m

```
load I_T2.txt.out
load t_T2.txt.out

figure
plot(t_T2_txt,I_T2_txt,'k')

set(gca,'xscale','log')
set(gca,'fontsize',16)
xlhand=get(gca,'xlabel');
set(xlhand,'String','T_2*(s)','fontsize',16)
ylhand=get(gca,'ylabel');
set(ylhand,'String','p(T_2*)','fontsize',16)
```

APPENDIX E – SS3 & SS2: T2 VALUES FROM MSME

The estimated T2 values from the signal decays of the slices, (the same decays the T2 distribution maps are generated from), are found in following tables. First is SS3 presented, thereafter SS2. T2 values are presented separate and in average. The average T2 values are plotted with water saturation.

Deviation of T2 means the largest deviation between T2 of the slices and the average. Uncertainty of water saturation in each slice must be larger than given in the table, because the core is not completely homogeneous saturated, and the saturation given here is average of the whole core.

T2 relaxation times were found to have a linear relationship with water saturation of the cores.

E.1 SS3 - T2 RELAXATION TIMES

Table E.1: SS3 - Water saturation and T2 relaxation times

Sw	**0,34**	**0,44**	**0,57**	**0,66**	**0,73**	**0,86**	**0,96**
±	0,01	0,01	0,01	0,01	0,01	0,01	0,01
T2 Slice 1 [ms]	9,7	12,7	19,2	30,9	37,2	35,4	31,8
T2 Slice 2 [ms]	15,4	24,1	43,1	43,2	46,7	45,1	42,3
T2 Slice 3 [ms]	9,7	15,5	26,3	33,4	39,5	40,3	37,9
Average T2 [ms]	**11,6**	**17,4**	**29,5**	**35,9**	**41,1**	**40,3**	**37,3**
Dev. [ms]	3,8	6,7	13,6	7,3	5,5	4,8	5,6

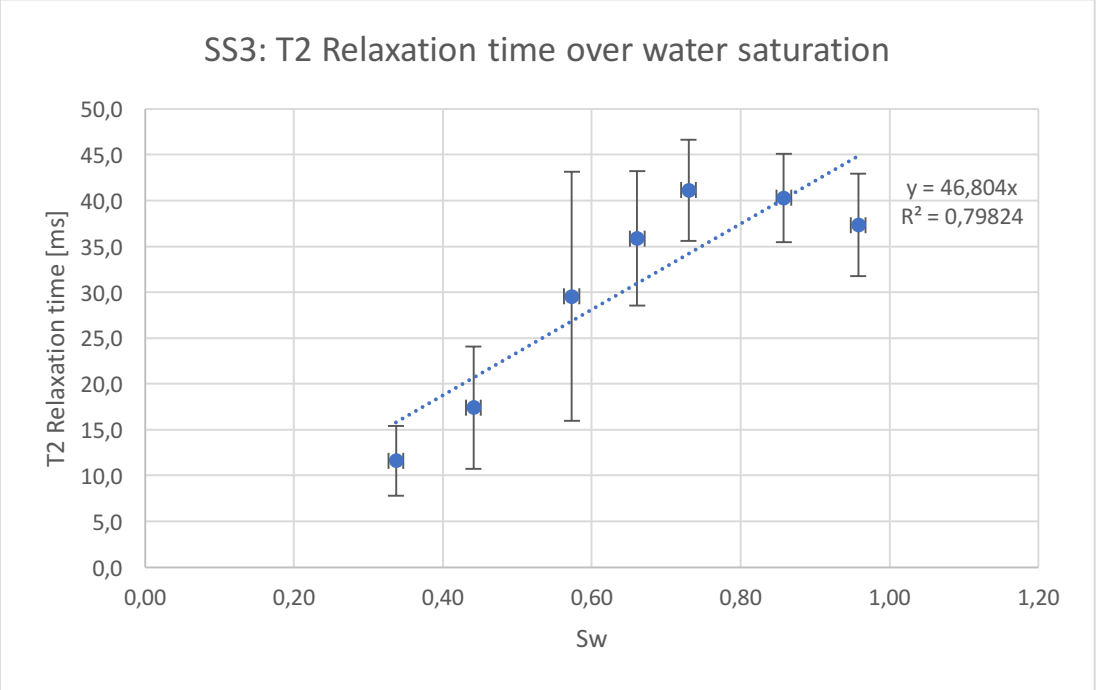

Figure E-0-1: Plott of average T2 relaxation time over saturation [frac].

E.2 SS2 - T2 RELAXATION TIMES

Table E.2: SS2 – Water saturation and T2 relaxation times

Sw	**0,35**	**0,58**	**0,68**	**0,81**	**0,96**
±	0,01	0,01	0,01	0,01	0,01
T2 (1) [ms]	7,3	12,9	15,4	30,1	32,8
T2 (2) [ms]	10,7	18,0	20,3	25,2	42,4
T2 (3) [ms]	9,5	14,4	15,7	30,7	37,9
Average T2 [ms]	**9,1**	**15,1**	**17,2**	**28,7**	**37,7**
Deviation	1,8	2,9	3,1	3,5	4,9

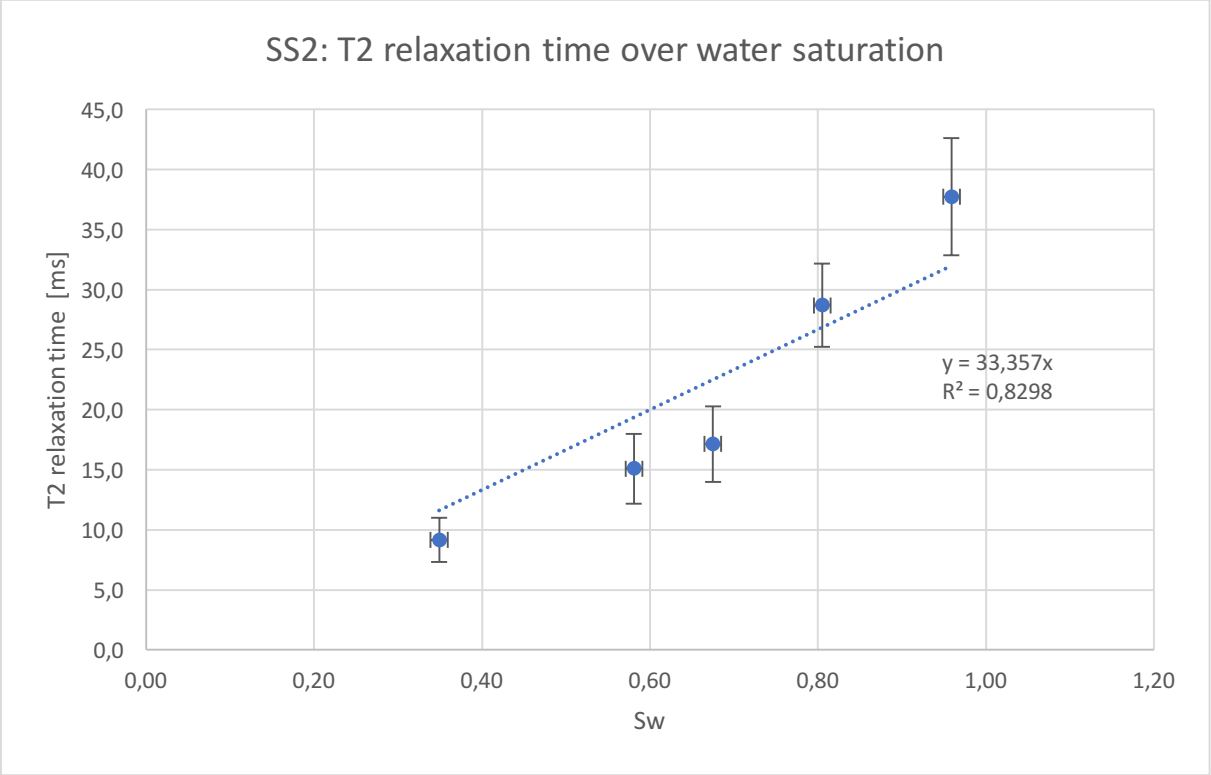

Figure E-0-2: Plott of average T2 relaxation time over saturation [frac].

APPENDIX F – SS3: T2 MAPS FOR ALL SATURATIONS

Following figures shows T2 distribution maps for the three slices, left (x) are from a square ROI, and right (o) from circular. The images below are the correlating slices, marked as 1-3.

Sw = 34 %

Square (X)

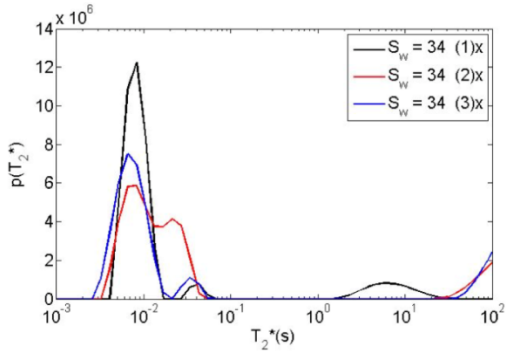

Circular (O)

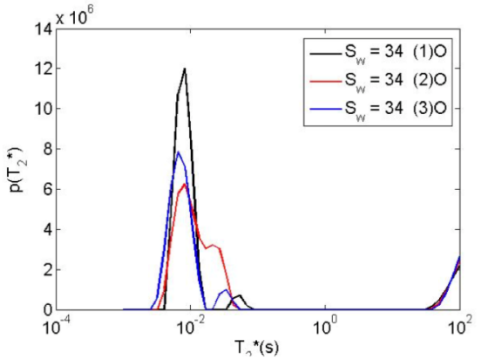

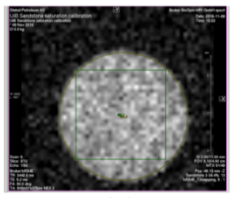

(1)

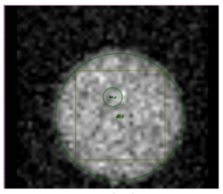

(2)

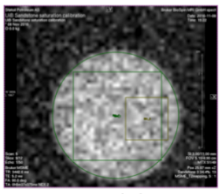

(3)

Sw = 44 %

Square (X)

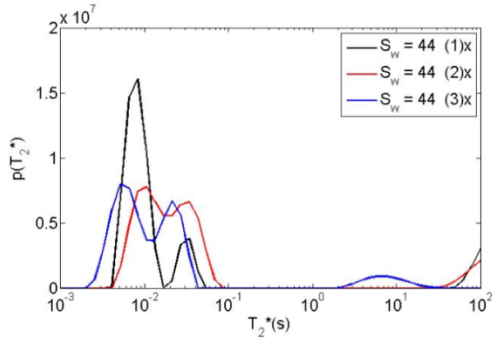

Circular (O)

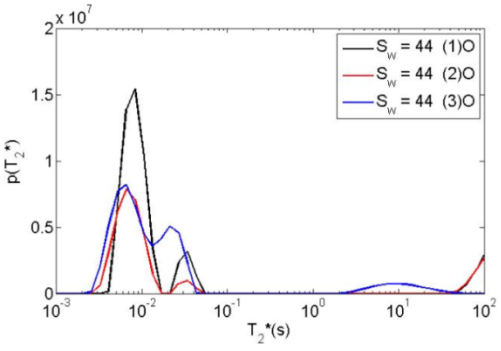

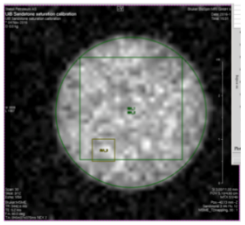

(1)

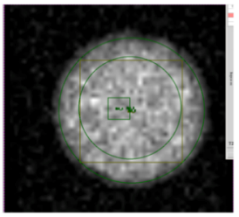

(2)

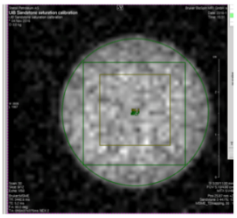

(3)

Sw = 57 %

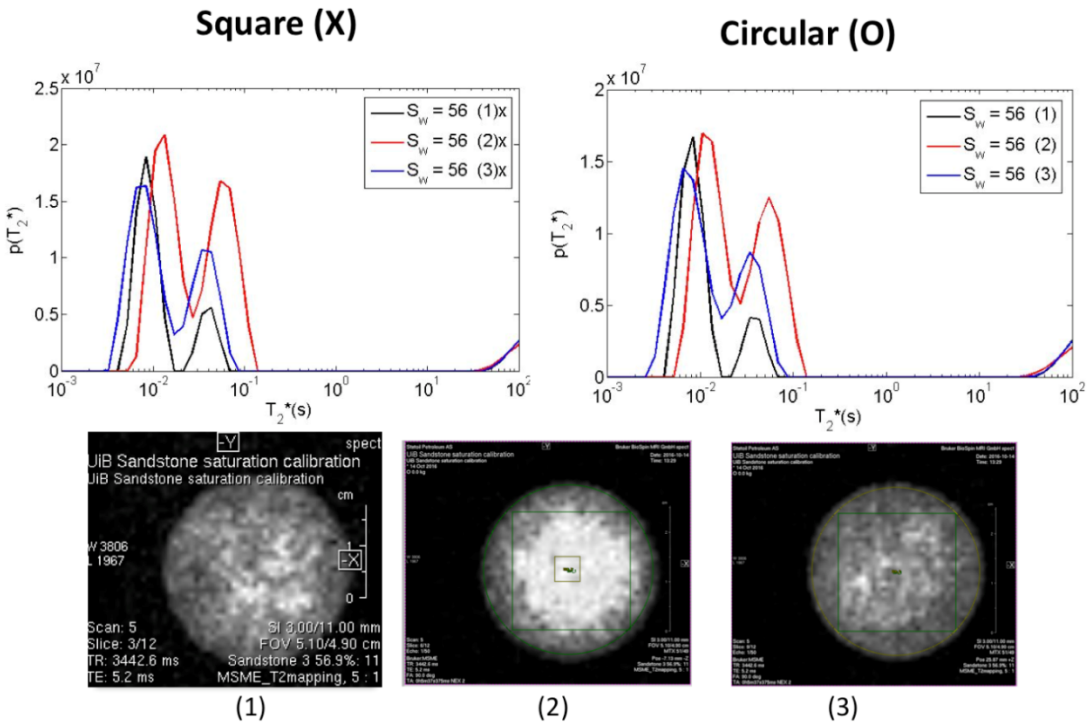
Square (X)
Circular (O)
x 10^7
p(T2*)
T2*(s)
Sw = 56 (1)x
Sw = 56 (2)x
Sw = 56 (3)x
Sw = 56 (1)
Sw = 56 (2)
Sw = 56 (3)
JiB Sandstone saturation calibration
JiB Sandstone saturation calibration
Scan: 5
Slice: 3/12
TR: 3442.6 ms
TE: 5.2 ms
Sandstone 3 56.9%: 11
MSME_T2mapping, 5 : 1
(1)
(2)
(3)

Sw = 66 %

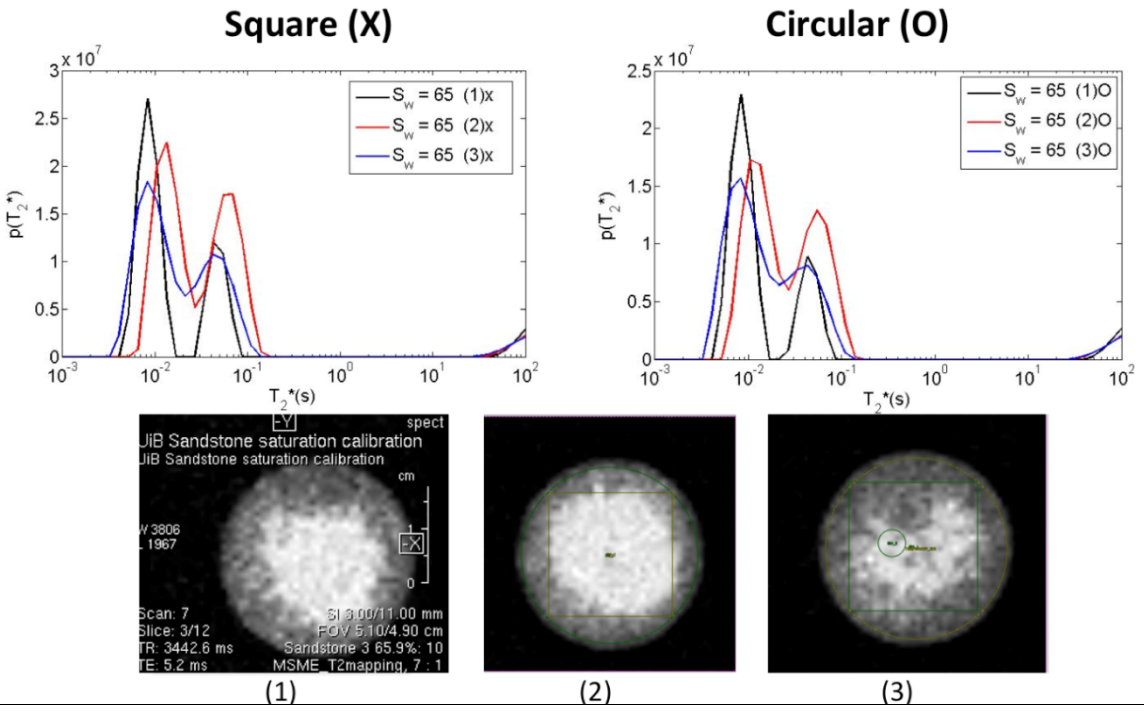
Square (X)
Circular (O)
x 10^7
p(T2*)
T2*(s)
Sw = 65 (1)x
Sw = 65 (2)x
Sw = 65 (3)x
Sw = 65 (1)O
Sw = 65 (2)O
Sw = 65 (3)O
JiB Sandstone saturation calibration
JiB Sandstone saturation calibration
Scan: 7
Slice: 3/12
TR: 3442.6 ms
TE: 5.2 ms
Sandstone 3 65.9%: 10
MSME_T2mapping, 7 : 1
(1)
(2)
(3)

Sw = 73 %

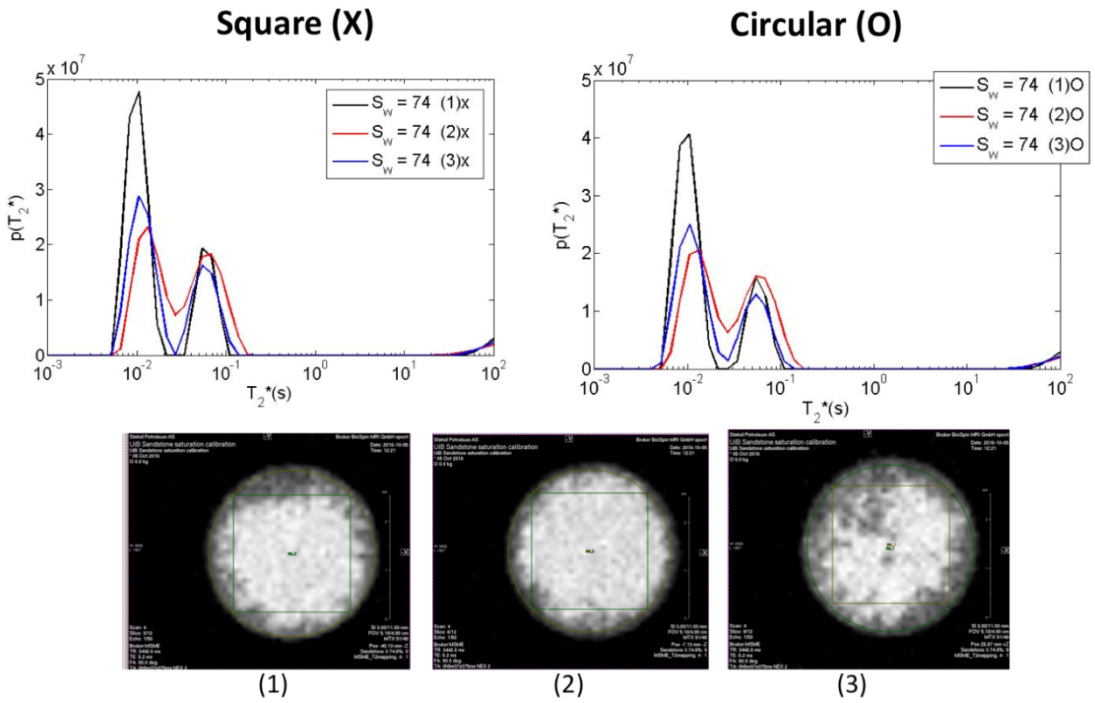
Square (X)
Circular (O)
x 10^7
p(T2*)
T2*(s)
Sw = 74 (1)x
Sw = 74 (2)x
Sw = 74 (3)x
Sw = 74 (1)O
Sw = 74 (2)O
Sw = 74 (3)O
(1)
(2)
(3)

Sw = 86 %

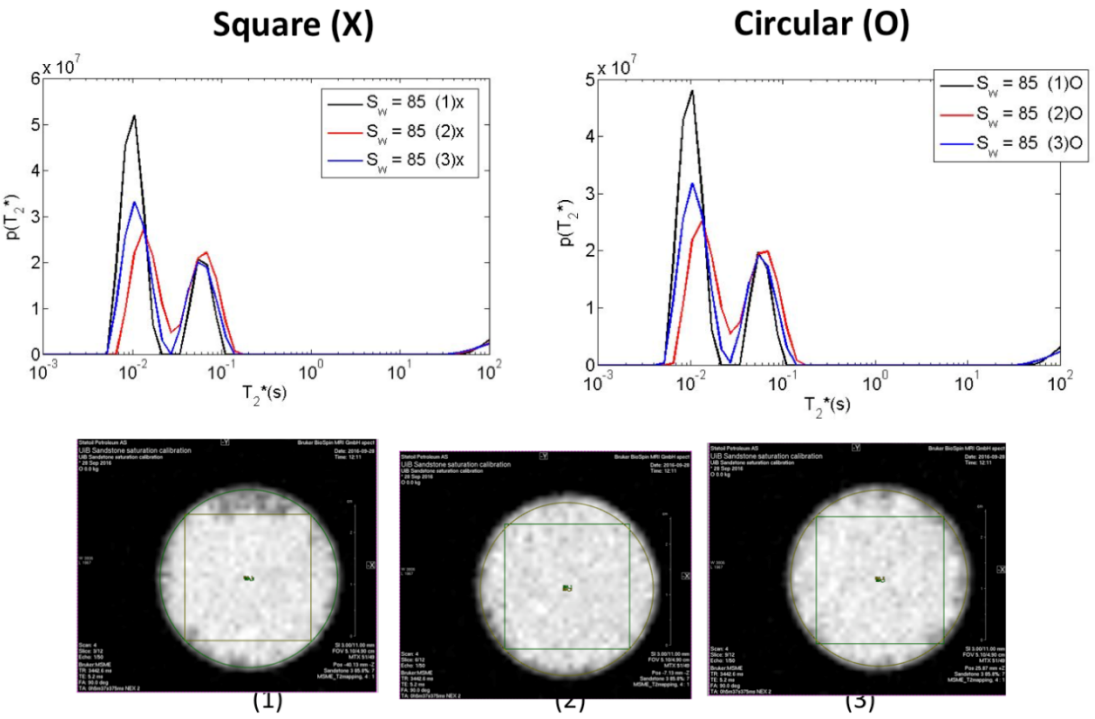
Square (X)
Circular (O)
x 10^7
p(T2*)
T2*(s)
Sw = 85 (1)x
Sw = 85 (2)x
Sw = 85 (3)x
Sw = 85 (1)O
Sw = 85 (2)O
Sw = 85 (3)O
(1)
(2)
(3)

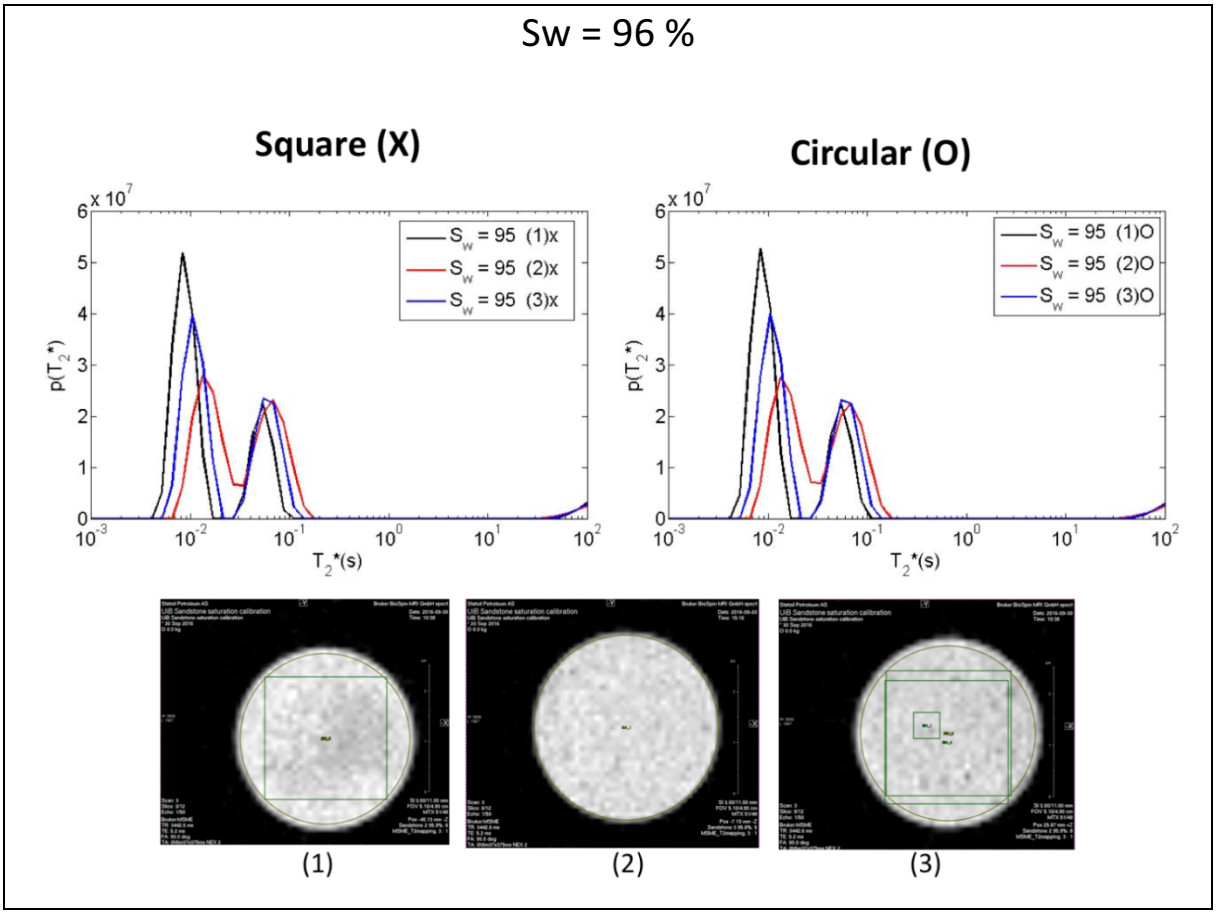

Figure F-1: T2 distribution maps for the three selected slices of SS3, at all the water saturation stages. Left, marked with (x) are based on decay curves from a square ROI, whereas to the right, marked with (o) are based on decay curves from a circular ROI. The three images at the bottom represent the three slices selected. Saturations given in the T2 distribution figures may vary 1 % from the one given on the top of the figures. The saturation on top is the more correct one.

APPENDIX G – MSME – Different Settings - Saturation Study

G.1 Short vs. Long Echo Time

A test of short versus long echo time was done to SS3 at 44% water saturation. By increasing the echo time, less information got picked up. Longer echo time resulted in smaller T2 distribution, only one top, and less variation through the core. See figure below for details.

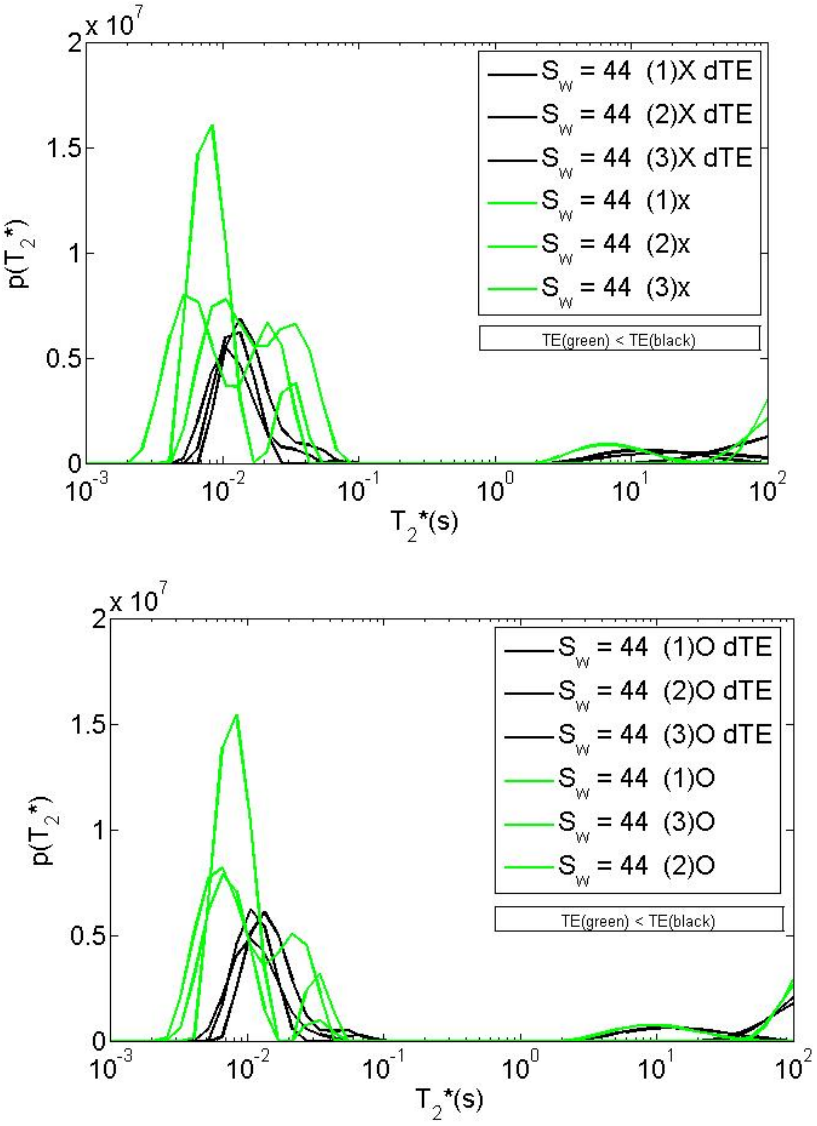

Figure G-1: Green represents short echo time (TE) (same as the ones used in the saturation study), black represents long echo time (dTE). Top, (X) square ROI, bottom, (O) circular ROI.

G.2 Different Settings (DS)

Another test of settings was done on SS2, at 58% water saturation. Summary of relevant settings used for the MSME measurements are found in Table G.1. Figure G-*2* displays the resulting T2 distributions for the different settings separate, then Figure G-3 displays the T2 distribution of the different settings per slice.

Table G.1: Different settings

	Saturation Study	DS1	DS2
Echo Time [ms]	5.16029	5.16029	6.19501
Repetition Time [ms]	3442.61	3442.61	3773.32
Number of Averages	2	22	10
Scan Time	0h5m37s375ms	1h1m51s129ms	1h20m29s846ms
Number of Slices	12	12	6
Slice Thickness [mm]	3.00	3.00	4.00
FOV [mm x mm]	51 x 49	51 x 49	51 x 49
Matrix	51 x 49	51 x 49	128 x 128

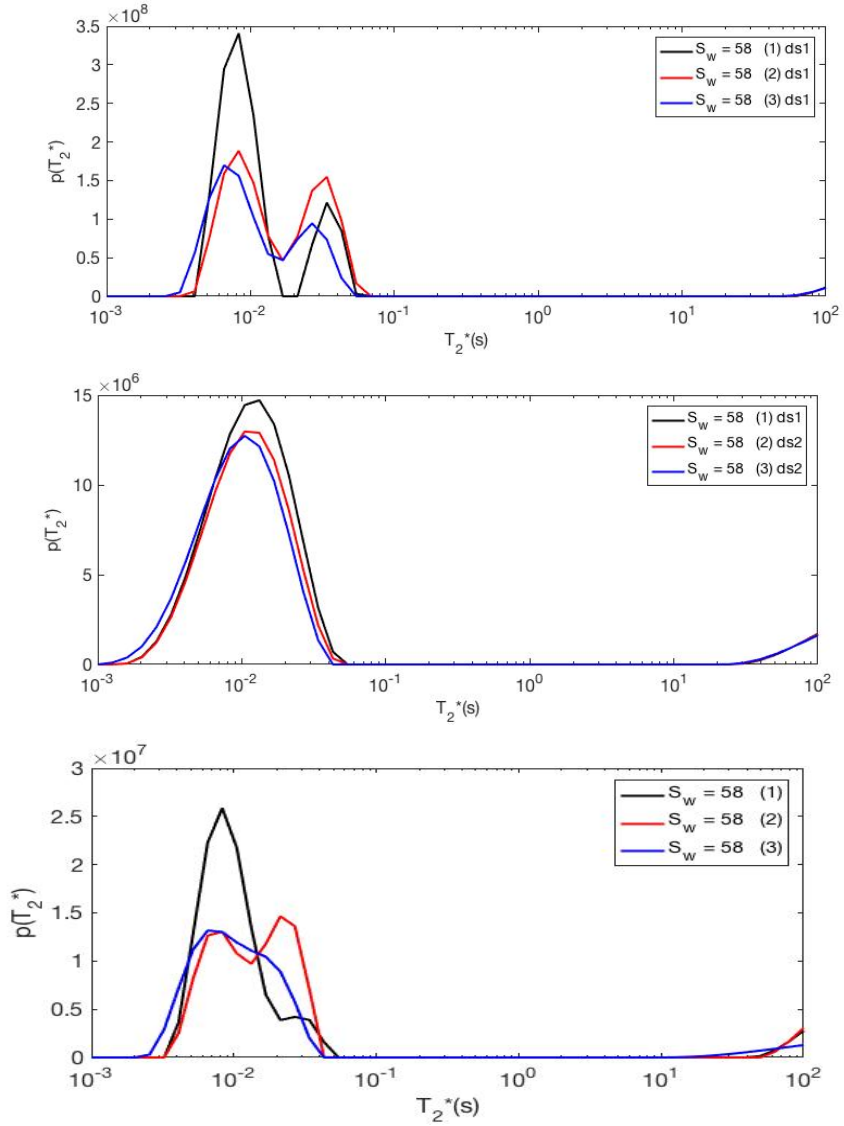

Figure G-2: Different settings, from top to bottom: Different settings 1 (ds1), different settings 2 (ds2), and last standard settings used for the saturation study.

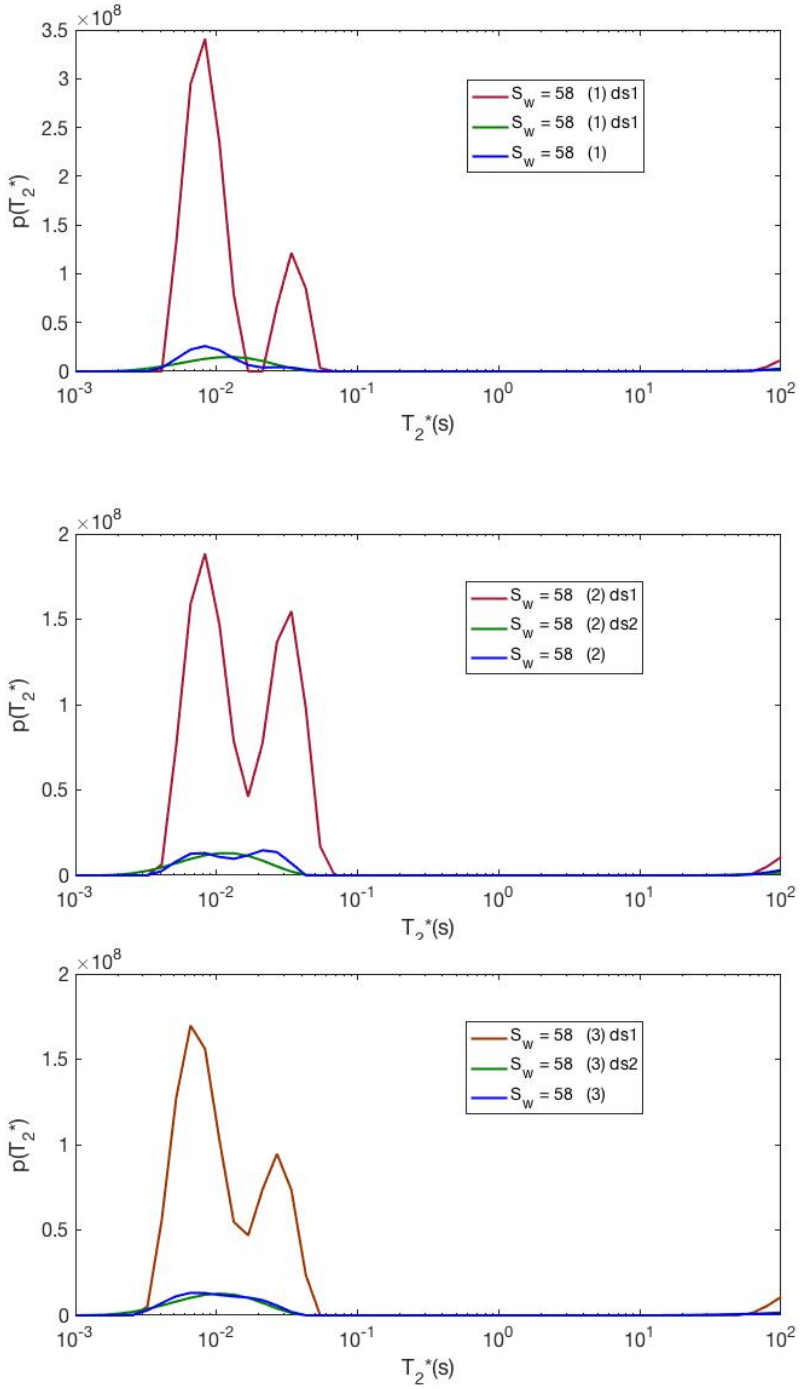

Figure G-3: Comparing the different T2 distributions from the different settings. The figures show the difference for each slice.

APPENDIX H – HPH2 – RARE figures–uncropped – f(intensity)

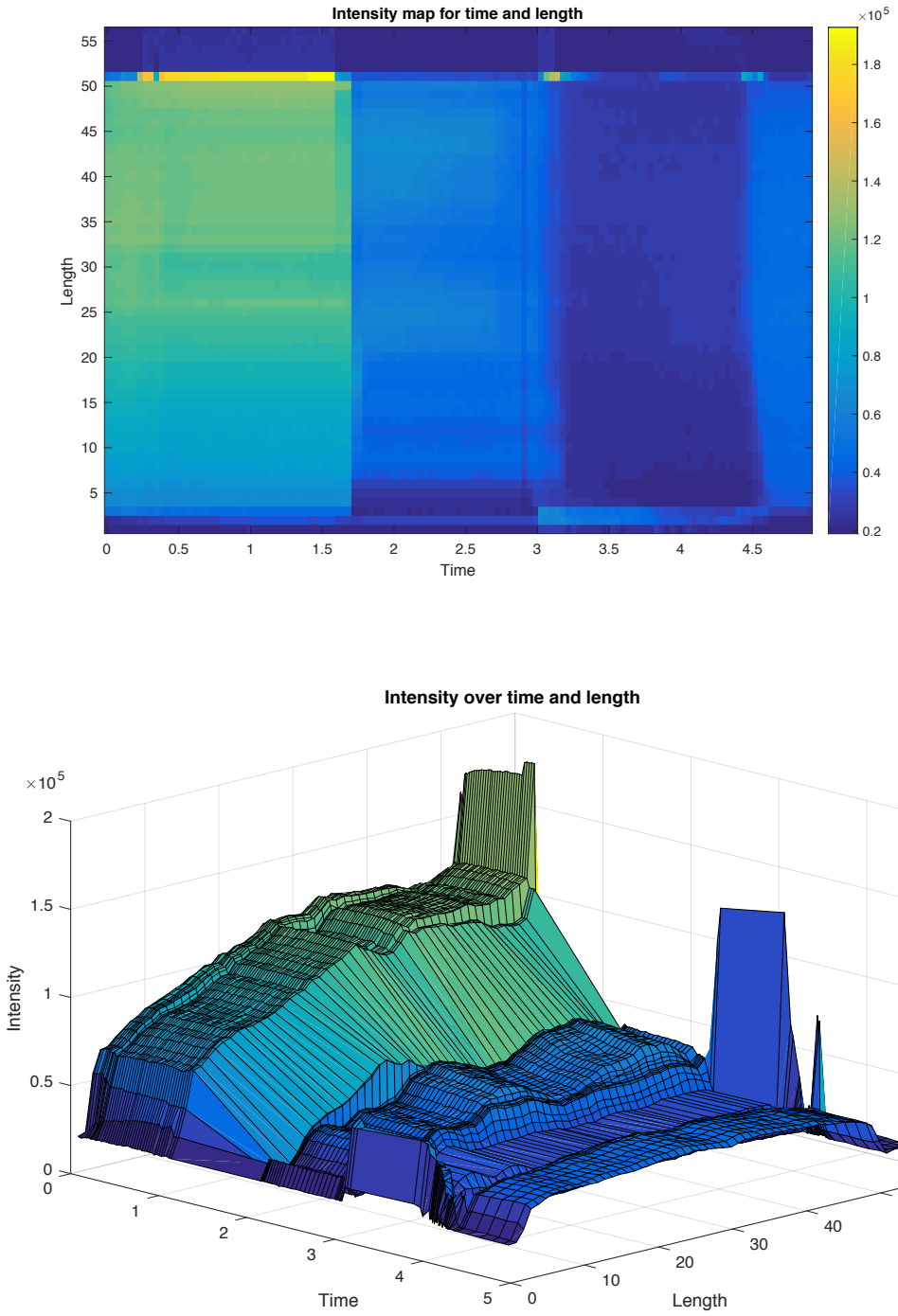

Figure H-0-1: Top, intensity map over time and length of the whole examination volume. Bottom, 3D intensity illustration over time and length of whole examination volume. The slices on the ends of the length do not contain the core, which is why they has been cropped in the main analysis.

BIBLIOGRAPHY

1. Hester, K.C. and P.G. Brewer, *Clathrate hydrates in nature.* Ann Rev Mar Sci, 2009. **1**: p. 303-27.
2. Kvamme, B., et al., *Effect of H2S Content on Thermodynamic Stability of Hydrate Formed from CO2/N2 Mixtures.* Journal of Chemical & Engineering Data, 2017. **62**(5): p. 1645-1658.
3. Peter Gatt, J.B., Bjørn Kvamme, *Gas hydrate technology - state of the art and future possibilities for Europe*, C. MIGRATE, Editor. 2017.
4. Magritek, *Routine Core Analysis*, in *Pore size distribution*.
5. Kvamme, B., *RE: Course PTEK232: Fundamentals of Natural Gas Hydrates and Practical Implications.* University of Bergen, 2016.
6. E. Dendy Sloan, C.A.K., *Clathrate Hydrates of Natural Gases*. 3rd ed. 2007: CRC Press.
7. Survey, U.S.G. *Database of Worldwide Gas Hydrates*. 2014 August 27, 2014; Available from: https://woodshole.er.usgs.gov/project-pages/hydrates/database.html.
8. Mitchell, J., et al., *Magnetic resonance imaging in laboratory petrophysical core analysis.* Physics Reports, 2013. **526**(3): p. 165-225.
9. Kleinberg, R.L. and D.D. Griffin, *NMR measurements of permafrost: unfrozen water assay, pore-scale distribution of ice, and hydraulic permeability of sediments.* Cold Regions Science and Technology, 2005. **42**(1): p. 63-77.
10. Almenningen, S., *An Experimental Study of Methane Hydrates in Sandstone Cores*, in *Department of Physics and Technology*. 2015, University of Bergen.
11. Bjørn Kvamme, O.K.F., *Polar guest-molecules in natural gas hydrates. Effects of polarity and guest-guest-interactions on the Langimuri-constants.* 1993.
12. Baldwin, B.A., et al., *Using magnetic resonance imaging to monitor CH4 hydrate formation and spontaneous conversion of CH4 hydrate to CO2 hydrate in porous media.* Magn Reson Imaging, 2009. **27**(5): p. 720-6.
13. E.G. Hammerschmidt, T.N.G.C., Fritch, Texas, *Formation of Gas Hydrates in Natural Gas Transmission Lines.* Industrial and Engineering Chemistry, 1934.
14. Makogon, Y.F., S.A. Holditch, and T.Y. Makogon, *Natural gas-hydrates — A potential energy source for the 21st Century.* Journal of Petroleum Science and Engineering, 2007. **56**(1-3): p. 14-31.
15. Collett, T., et al., *Methane Hydrates in Nature—Current Knowledge and Challenges.* Journal of Chemical & Engineering Data, 2015. **60**(2): p. 319-329.
16. T. S. Collett, A.H.J., C.C. Knapp, R. Boswell, *Natural Gas Hydrates: A Review.* 2009.
17. Rodger, P.M., *Stability of Gas Hydrates.* The Journal of Physical Chemistry, 1990: p. 6080-6089.
18. Sloan, E.D., *Fundamental principles and applications of natural gas hydrates.* NATURE, 2003.
19. Birkedal, K.A., *Empirical and Numerical Evaluation of Mechanisms in Gas Production from CH4-hydrates: Emphasis on Kinetics, Empirical Resistivity, Depressurization and CO2-CH4 Exchange*, in *Department of Physics and Technology*. 2013, University of Bergen: bora.uib.no.
20. NOVA, P. 2017; Available from: https://www.pvtsimnova.com/.
21. Englezos, P., *Nucleation and Growth of Gas Hydrate Crystals in Relation to Kinetic Inhibition.* Revue de l'Institut Français du Pétrole, 1996. **51**(6): p. 789-795.

22. D. Katsuki, R.O., T. Ebinuma, H. Narita, *Methane hydrate crystal growth in a porous medium filled with methane-saturated liquid water.* Philosophical Magazine, 2007. **87**(7).
23. Volmer, M., *Kinetik der Phasenbildung.* Steinkopff, Dresden, 1939.
24. Kashchiev, D. and A. Firoozabadi, *Induction time in crystallization of gas hydrates.* Journal of Crystal Growth, 2003. **250**(3-4): p. 499-515.
25. George J. Moridis, M.B.K., Karsten Pruess, *Depressurization-Induced Gas Production From Class 1 Hydrate Deposits.* SPE Reservoir Evaluation & Engineering, 2007.
26. Ersland, G., *Studies of flow mechanisms and hydrate phase transitions in fractured rocks*, in *Department of Phydics and Technology*. 2008, University of Bergen.
27. Christian Berndt, J.M., Maarten Vaaneste, Stefan Bunz, *Gas hydrate dissociation and sea-floor collapse in the wake of the Storegga Slide, Norway.* Norwegian Petroleum Society Special Publications, 2005. **12**.
28. A. Graue, B.K., B. A. Baldwin, J. Stevens, J. howard, G. Ersland, J. Husebø, D.R. Zornes, *MRI Visualization of Spontaneous Methane Production From Hydrates in Sandstone Core Plugs When Exposed to CO2.* SPE Reservoir Evaluation & Engineering, 2008.
29. Ota, M., et al., *Replacement of CH4 in the hydrate by use of liquid CO2.* Energy Conversion and Management, 2005. **46**(11-12): p. 1680-1691.
30. Ruppel, C.D., *Methane Hydrates and Contemporary Climate Change.* Nature Education Knowledge, 2011.
31. Oljedirektoratet, *CO2 samleatlas for Norsk kontinentalsokkel*, in *2. Petroleum activity on the NCS*. 2014.
32. G. D, F., A. G Judd, *The orgins of shallow gas.* 1992.
33. Torres, M.E., et al., *Methane hydrate formation in turbidite sediments of northern Cascadia, IODP Expedition 311.* Earth and Planetary Science Letters, 2008. **271**(1-4): p. 170-180.
34. A. M. Tréhu, C.R., M. Holland, G. R. Dickens, M. E. Torres, T. S. Collett, D. S. Goldberg, M. Riedel, P. Schultheiss,, *Oceanography.* 2006.
35. G. J. Moridis, T.S.C., *Gas Production from Class 1 Hydrate Accumulations* Recent Advances in the Study of Gas Hydrates, 2004.
36. Ray Boswell, T.C., *The Gas Hydrates Resource Pyramid.* NETL, Fire in the Ice, Methane Hydrate Newsletter, 2006.
37. Reuters, *China produces gas from "flammable ice" under South China Sea*, in *REUTERS*. 2017: reuters.com.
38. Mark A. Brown, R.C.S., *MRI Basic Principles and Applications*. Third Edition ed. 2003: Wiley - Liss.
39. Chavhan, G.B., et al., *Principles, techniques, and applications of T2*-based MR imaging and its special applications.* Radiographics, 2009. **29**(5): p. 1433-49.
40. Brown, R.W., et al., *Magnetic Resonance Imaging : Physical Principles and Sequence Design*. 2014, Somerset, UNITED STATES: Wiley.
41. AD Elster, E.L. *T2 vs. T2**. 2009; Available from: http://mriquestions.com/t2-vs-t2.html.
42. Oleg V. Petrov, G.E., Bruce J. Balcom, *T2 distribution mapping profiles with phase-encode MRI.* Journal of Magnetic Resonance 2011.
43. G. C. Borgia, V.B., R. J. S. Brown, P. Fantazzini, *A robust method for calculating geometric mean times from multiexponential relaxation data, using only a few data*

points and only a few elementary operations. Magn Reson Imaging, 1996. **14**: p. 895-897.
44. Lien, J.R., *PTEK211 - Grunneleggende reservoarfysikk (Kjerneanalyse og logging)*. 2004, Institutt for fysikk og teknologi, Universitetet i Bergen.
45. Vinciguerra, S., *Rock Physics and Natural Hazards*. 2009: Birkhauser.
46. Ersland, G., et al., *Measuring gas hydrate formation and exchange with CO2 in Bentheim sandstone using MRI tomography.* Chemical Engineering Journal, 2010. **158**(1): p. 25-31.
47. Yang, M.S., Y. Zhao, Z. , *MRI Measurements of CO2 Hydrate Formation and Dissociation in Porous Medium.* ISOPE, 2010.
48. B.A. Baldwin, A.M.-A., J.C. Stevens, *Monitoring hydrate formation and dissociation in sandstone and bulk with magnetic resonance imaging.* Magn Reson Imaging, 2003: p. 1061-1069.
49. Ersland, G., et al., *Transport and storage of CO2 in natural gas hydrate reservoirs.* Energy Procedia, 2009. **1**(1): p. 3477-3484.
50. Husebø, J., et al., *Effects of salinity on hydrate stability and implications for storage of CO2 in natural gas hydrate reservoirs.* Energy Procedia, 2009. **1**(1): p. 3731-3738.
51. Sarah Vashaee1, M.L., Bryce MacMillan1, Razieh Enjilela1, Derrick P. Green2, F. Marica1, Bruce J. Balcom1, 1 UNB MRI Research Centre, Department of Physics, University of New Brunswick, E3B 5A3, Canada. 2 Green Imaging Technologies, Inc., 520 Brookside Drive, Suite B Fredericton, NB, E3A 8V2, Canada, *Magnetic Resonance Imaging with a Variable Field Superconducting Magnet that can be rotated for Vertical or Horizontal Operation*. 2017.
52. Coyne, K. *MRI: A Guided Tour*. 2017 22. March 2017; Available from: https://nationalmaglab.org/education/magnet-academy/learn-the-basics/stories/mri-a-guided-tour.
53. Moyer, B. *An Overview of Medical Imaging*. 2013; Available from: https://www.electronicproducts.com/RF_and_Microwave_Components/RF_and_Microwave/An_Overview_of_Medical_Imaging.aspx?id=2546.
54. Bruker. *BioSpec*. 2017; Available from: https://www.bruker.com/products/mr/preclinical-mri/biospec/overview.html.
55. Heidenreich, M., . *System Manual for AVANCE III HS/MRI Instruments.* 2014, Bruker.
56. Graham, R.N., R.W. Perriss, and A.F. Scarsbrook, *DICOM demystified: a review of digital file formats and their use in radiological practice.* Clin Radiol, 2005. **60**(11): p. 1133-40.